

Contents lists available at ScienceDirect

Journal of the Mechanics and Physics of Solids

journal homepage: www.elsevier.com/locate/jmps





A thermodynamically consistent gradient theory for diffusion–reaction–deformation in solids: Application to conversion-type electrodes

Arman Afshar, Claudio V. Di Leo *

School of Aerospace Engineering, Georgia Institute of Technology, United States of America

ARTICLE INFO

Keywords: Continuum chemo-mechanics Reaction-induced Deformation Diffusion-reaction Phase field formulation Energy storage

ABSTRACT

We develop a thermodynamically consistent phase-field finite strain theory for problems in solids mechanics that couple transport of species into a host material, sharp interface reactions of the species with the host, mechanical deformation and stress. The theory distinguishes between diffusion-limited and reaction-limited kinetics, resolving the manner in which a sharp reaction front can be developed in either case. The phase field formulation has the added benefit of enabling the application of wetting (surface energy) boundary conditions which are critical in reproducing experimentally relevant reaction front morphologies. The theory is fully coupled with diffusion and reaction phenomena impacting mechanical deformation and subsequent stress generation, and conversely these phenomena are coupled to mechanical stress. We derive thermodynamically consistent driving forces for diffusion and reaction through a continuum treatment of these phenomena. Importantly, the resulting formulation makes precise the nature of the material properties driving these thermodynamic forces and in turn makes it amenable to being specialized and calibrated for application.

While the framework is quite general, we apply it to modeling conversion electrodes for energy storage using a three-dimensional finite element implementation. We demonstrate the manner in which the theory can be specialized and calibrated in straightforward fashion. Simulations are performed of chemical reactions of FeS_2 crystals with lithium and sodium ions, both of which proceed through the formation and propagation of a sharp interface, and are compared to experimental observations of the same system. Our simulations show good qualitative agreement with experimental observations, and elucidate the critical role mechanics plays in determining the morphology of the sharp reaction interface and subsequent stress generation which can lead to mechanical deterioration of these materials. Beyond this application, the theoretical framework should serve useful in a number of engineering problems of relevance in which diffusion and sharp interface reactions occur.

1. Introduction

The development of theoretical frameworks in continuum mechanics which couple chemical stimuli and mechanical deformation – in particular those involving coupling of species diffusion with deformation of the host material – have received significant attention in the recent literature. This drive is largely attributed to the need for understanding the interplay of chemistry and mechanics in a number of engineering problems of relevance where mechanics plays a non-negligible role in the performance of

E-mail address: cvdileo@gatech.edu (C.V. Di Leo).

^{*} Corresponding author.

the material. These include energy storage devices (Christensen and Newman, 2006; Zhang et al., 2007; Cheng and Verbrugge, 2008; Cui et al., 2012), chemically active polymers (Bosnjak et al., 2020; Okumura et al., 2020; Mao and Anand, 2018), oxides and corrosion phenomena (Loeffel and Anand, 2011; Konica and Sain, 2020; Cui et al., 2020), as it has become clear that mechanics plays an important role on the chemo-mechanical performance of these systems. Specifically, the design and analysis of energy storage devices required new models that addressed the coupling between transport phenomena and mechanics, and from this need came a group of theories specifically devoted to modeling these problems. The review papers by Zhao et al. (2019b) and Bistri et al. (2020) provide a recent summary of modeling efforts in this area. Among these, the thermodynamics based finite strain models of Bower et al. (2011), Zhao et al. (2011a), Anand and co-workers (Anand, 2012; Di Leo et al., 2014), Levitas and Attariani (2014), Brassart and Suo (2013), and Ganser et al. (2019) are notable for their rigorous treatment of the coupling between diffusion and mechanics. These frameworks have been successfully applied to capturing experimentally observed electrochemical phenomena in energy storage devices (cf. Bucci et al., 2014; Di Leo et al., 2015). While rigorous, current theoretical frameworks are largely limited to the class of problems in which the concentration of diffusing species is conserved, i.e. there is no chemical reaction within the solid to convert mass from one compound to another.

There are a number of technologically important applications requiring an understanding of the coupling between chemistry and mechanics including the manner in which reactions occur within the solid. These applications range from oxidation and polymerization (cf. Tolpygo et al., 1998; Minervino et al., 2014; El Kadiri et al., 2008; Gigliotti et al., 2011) to reaction based electrodes for energy storage (cf. Lin et al., 2014; Li et al., 2012). Notable works in thermodynamics based models for modeling reaction–diffusion phenomena including mechanical deformation are the works of Loeffel et al. (2013) for modeling thermal barrier coating oxidation, Zhao et al. (2019a) for SiC fiber oxidation, Xu et al. (2019) for thermal coating corrosion, the general formulation of Svendsen et al. (2018) for phase-field based modeling, and Salvadori et al. (2018) for trapping reactions. The aforementioned theoretical frameworks have made significant progress towards modeling diffusion–reaction problems in solids; however, they lack in a few key areas which we seek to address in this work.

The purpose of this work is to report on a novel, thermodynamically consistent, gradient, theoretical framework for modeling concurrent diffusion, reactions, and deformations in solids with a particular emphasis on problems in which sharp reaction interfaces occur. The framework is general and should be applicable to a number of engineering problems. In particular, our framework includes the following unique features distinguishing it from previous work in this area:

- The theoretical framework allows for both kinetically and thermodynamically driven sharp interface formation. Kinetically driven interfaces occur in systems in which the reaction kinetics are significantly faster than the diffusion kinetics. Thermodynamically driven sharp interfaces can occur in any system including those in which the reaction kinetics are sluggish and are driven by the existence of a thermodynamic energy barrier between reacting phases.
- The theoretical framework develops a thermodynamically consistent, physically motivated, driving force for chemical reactions that distinguishes the role of various chemical and mechanical driving forces. Particularly useful then is the fact that material properties driving the reaction kinetics can be easily identified from the literature or experiments.
- The gradient based phase-field formulation allows us to capture surface energy phenomena which significantly affect the morphology of the reaction front. In particular, surfaces with lower energy for being fully reacted will become fully "wetted" (i.e. fully reacted) and this is consistently captured using our gradient formulation (cf. the work of Bazant and co-workers Bazant, 2013; Cogswell and Bazant, 2013; Nadkarni et al., 2018).

To demonstrate the relevance and use of this theoretical framework we specialize it to model the particular engineering problem of reaction electrodes (i.e. conversion electrodes) for energy storage. An accompanying three-dimensional finite element implementation is used to compare numerical simulations using our novel theoretical framework with experimental results. Current state of the art lithium-ion batteries make use of active particles, such as graphite, whose primary mechanism of lithium storage is intercalation. Alternatively, next generation electrode materials made of transition metal oxides which store charge carrying ions via chemical conversion mechanism have recently been given attention as their theoretical capacity dwarfs that of intercalation based electrodes. This superior capacity has been linked to the high number of ions per structural unit that can be stored via conversion vs the lower number that can be intercalated into layered structure of intercalation based electrodes (Poizot et al., 2000; Yu et al., 2016; Li et al., 2012). The conversion reaction, however, is accompanied by structural and chemical phase transformation of the host material (cf. Wang et al., 2012), resulting in a rich chemo-mechanics problem. The exact energy density and the crystalline or amorphous structural phase transformation incurred by the electrode during electrochemical cycling depend on the specific transition metal oxide used (cf. Yu et al., 2016 for a detailed comparison between different compounds). However, nearly all compounds and their nano-structured variations incur very large volumetric expansion and structural changes on the order of $\approx 100\%$ strain during cycling (cf. Zhang et al., 2008; Larcher et al., 2002; Ren et al., 2014; Hu et al., 2006). These large reaction-induced deformations can lead to mechanical and electrochemical battery degradation, necessitating the development of a theory that accounts for diffusion of species, chemical reaction and subsequent phase transformation, mechanical deformation and stress, and how these fields are coupled.

We specialize our theoretical framework to modeling the reaction of FeS₂ crystals with different ions as experimentally investigated by Boebinger et al. (2018). In doing so, we demonstrate the manner in which mechanics affects the chemical reaction kinetics and morphology of the sharp interface. We further elucidate the role of wetting (surface energy) chemical boundary condition in reproducing reaction morphologies which are consistent with experimental observations. Finally, using our theoretical framework and numerical implementation we provide insight as to how mechanical coupling can explain the counterintuitive

experimental observation made by Boebinger et al. (2018), where reactions with larger sodium ions resulted in a more mechanically reliable structure when compared to reactions with lithium ions.

We begin with the conceptual depiction of a generic diffusion–reaction–deformation process as shown in Fig. 1. The figure depicts the reaction

$$A + C \to B \tag{1.1}$$

which describes the physical phenomena of diffusing species C reacting with the host lattice A to form the new compound B. The reaction itself is treated in a phase-field sense and taken to occur over a diffuse boundary (light gray region) and is tracked through the normalized phase-field parameter $\bar{\xi}$ which is formally introduced in Section 2. A value of $\bar{\xi} = 0$ represents the original material A, and a value of $\bar{\xi} = 1$ represents the fully reacted and newly formed compound B, while naturally intermediate values of $0 < \bar{\xi} < 1$ represent the reaction zone. The inset in Fig. 1 shows a conceptual illustration of the reaction zone where the phase α is associated with the unreacted material A, while the phase β is associated with the reacted compound B. We note that the reacted phase β may also act as a host for the diffusing species as shown schematically.

The paper is organized as follows. In Section 2 we introduce mass conservation and formally define our physically motivated phase-field parameter ξ governing the extent of reaction. In Section 3 we describe the kinematics of the problem. We introduce a novel decomposition of the velocity gradient to account for chemically induced deformations. Governing balance laws are developed in Section 4 through the use of the principle of virtual power, and the first and second laws of thermodynamics. The constitutive theory is presented in Section 5 and summarized in its general form in Section 6. In Sections 7 and 8 we present a specialization of our theoretical framework to modeling conversion electrodes for energy storage.

Numerical simulations are presented in Section 9. First, in Section 9.1 we present diffusion–deformation (without mechanics) simulations to elucidate the kinetically driven and thermodynamically driven regimes of sharp interface formation. In Section 9.2 we simulate the reaction of FeS_2 crystals with either lithium or sodium ions and compare to experimental results form the literature. Finally, in Section 9.3 we present a series of simulations aimed at elucidating the important role of surface wetting (surface energy) boundary conditions in capturing experimentally relevant reaction front morphologies. We close with concluding remarks in Section 10.

2. Mass conservation

Considering the diffusion-reaction problem shown schematically in Fig. 1, we wish to write mass conservation for the generic reaction

$$A + C \to B. \tag{2.1}$$

Let $c(\mathbf{X},t)$ denote the number of moles of diffusing species per unit *reference volume*. In addition, let ξ denote the number of moles of reacted species per unit *reference volume* with $\dot{\xi}$ the reaction rate. We may then define the quantity $\bar{\xi} = \xi/c_{\max}^R \in [0,1]$ as the extent of reaction such that at $\bar{\xi} = 1$ the reaction has led to consumption of c_{\max}^R moles of species. The physical property c_{\max}^R is the maximum amount of diffusing species that can be reacted and is determined by the stoichiometry of the specific reaction under consideration. Conservation of mass may then be written as a diffusion–reaction equation of the form

$$\dot{c} = -\text{Div } \mathbf{j}_{R} - \dot{\xi} \tag{2.2}$$

where $\mathbf{j}_{R}(\mathbf{X},t)$ is the referential flux of the diffusing species which must be constitutively prescribed. In (2.2), the reaction rate $\dot{\xi}$ must also be constitutively defined and will be discussed in detail in the development of this framework.

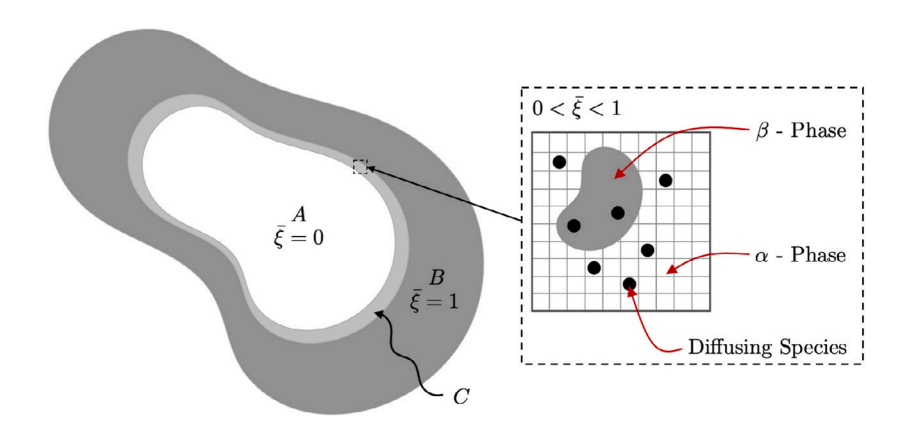


Fig. 1. Schematic representation of the diffusion–reaction problem of a diffusing species C reacting with host A to form the new compound B. $\bar{\xi}=0$ and $\bar{\xi}=1$ denote unreacted and fully reacted material points respectively. $0<\bar{\xi}<1$ denotes the reaction zone.

Note that the reaction quantity ξ is independent from the concentration of the diffusing species in either the original or reacted material. This distinction is critical since the newly formed phase may still host the diffusing species. In other words, the reacted phase is still a host, but with a new compound. This field treatment is different from the traditional formulation applied to modeling intercalation based active materials where only one parameter, the concentration of diffusing species, is sufficient to describe the state of the system. Further, we note that the quantity $c_{\text{max}}^{\text{R}}$, denoting the maximum amount of a diffusing species which may react to form the new compound, is different and independent from the maximum amount of diffusing species $c_{\text{max}}^{\text{D}}$, which can be hosted in either the pristine or reacted material.

3. Kinematics

We introduce here the kinematic formulation for the description of a deformation resulting from coupled chemical diffusion, reactions and mechanics. Starting from a traditional finite deformation framework, consider a body B with an arbitrary material point in B denoted by **X**. The motion of B is then a smooth one-to-one mapping $\mathbf{x} = \chi(\mathbf{X}, t)$ with deformation gradient, velocity, and velocity gradient given by¹

$$\mathbf{F} = \nabla \chi, \qquad \mathbf{v} = \dot{\chi}, \qquad \mathbf{L} = \operatorname{grad} \mathbf{v} = \dot{\mathbf{F}} \mathbf{F}^{-1}.$$
 (3.1)

The theory is built on two kinematic decompositions: (i) a multiplicative decomposition of the deformation gradient, and (ii) an additive decomposition of the velocity gradient for the chemical distortion. First, we decompose the deformation gradient as

$$\mathbf{F} = \mathbf{F}^{\text{mechanical}} \mathbf{F}^{\text{chemical}} = \mathbf{F}^{\mathbf{m}} \mathbf{F}^{\mathbf{c}}. \tag{3.2}$$

Here

- (i) **F**^c(**X**) represents the combined local distortion of the material neighborhood of **X** due to chemical phenomena including: (a) diffusion of species, and (b) structural phase transformations resulting from the chemical reaction;
- (ii) **F**^m(**X**) represents the distortion due to *macroscopic stresses*. These may include distortions due to classical plasticity mechanisms such as dislocation motion, and the subsequent elastic stretching and rotation of this inelastically deformed material neighborhood.

We refer to \mathbf{F}^m and \mathbf{F}^c as the *mechanical* and *chemical* distortions, respectively. Importantly, we note here that \mathbf{F}^c is assumed to account for inelastic mechanisms associated with diffusion–reaction, and hence does not include classical plasticity that is due to applied external forces which may be included in the mechanical distortion \mathbf{F}^m .

The volume ratio is given by

$$J \stackrel{\text{def}}{=} \det \mathbf{F} > 0, \tag{3.3}$$

and using (3.2),

$$J = J^{\mathrm{m}} J^{\mathrm{c}}$$
, with $J^{\mathrm{m}} \stackrel{\mathrm{def}}{=} \det \mathbf{F}^{\mathrm{m}} > 0$, and $J^{\mathrm{c}} \stackrel{\mathrm{def}}{=} \det \mathbf{F}^{\mathrm{c}} > 0$, (3.4)

such that \mathbf{F}^{m} and \mathbf{F}^{c} are invertible. The right and left polar decomposition of \mathbf{F}^{m} is given by

$$\mathbf{F}^{\mathbf{m}} = \mathbf{R}^{\mathbf{m}} \mathbf{U}^{\mathbf{m}} = \mathbf{V}^{\mathbf{m}} \mathbf{R}^{\mathbf{m}},\tag{3.5}$$

where \mathbf{R}^m is a rotation, while \mathbf{U}^m and \mathbf{V}^m are symmetric, positive-definite right and left stretch tensors. The right Cauchy–Green deformation tensor is given by

$$\mathbf{C}^{\mathbf{m}} = (\mathbf{U}^{\mathbf{m}^2}) = \mathbf{F}^{\mathbf{m}\mathsf{T}} \mathbf{F}^{\mathbf{m}}. \tag{3.6}$$

Using (3.1) and (3.2), the velocity gradient may be written as

$$L = L^{m} + F^{m}L^{c}F^{m-1}$$
(3.7)

with

$$L^{m} = \dot{\mathbf{F}}^{m} \mathbf{F}^{m-1}, \qquad L^{c} = \dot{\mathbf{F}}^{c} \mathbf{F}^{c-1}.$$
 (3.8)

As is standard, we define mechanical and chemical stretching and spin tensors through

$$\mathbf{D}^{m} = \operatorname{sym} \mathbf{L}^{m}, \qquad \mathbf{W}^{\text{mech}} = \operatorname{skw} \mathbf{L}^{m},$$

$$\mathbf{D}^{c} = \operatorname{sym} \mathbf{L}^{c}, \qquad \mathbf{W}^{\text{chem}} = \operatorname{skw} \mathbf{L}^{c},$$
(3.9)

such that $\mathbf{L}^m = \mathbf{D}^m + \mathbf{W}^m$ and $\mathbf{L}^c = \mathbf{D}^c + \mathbf{W}^c$.

Notation: We use standard notation of modern continuum mechanics used by Gurtin et al. (2010). Particularly: ∇ and Div denote the gradient and divergence operators with respect to the material point **X** in reference configuration; while grad and div operate with respect to the point $\mathbf{x} = \chi(\mathbf{X}, t)$ in the deformed body; a superposed dot denotes the material time-derivative. Throughout, we write $\mathbf{F}^{e-1} = (\mathbf{F}^e)^{-1}$, $\mathbf{F}^{e-7} = (\mathbf{F}^e)^{-7}$, etc. We also write tr**A**, sym **A**, skw **A**, **A**₀, and sym₀**A** respectively, for the trace, symmetric, skew, deviatoric, and symmetric-deviatoric parts of a tensor **A**. Finally, the inner product of tensors **A** and **B** is denoted by **A**: **B**, and the magnitude of **A** by $|\mathbf{A}| = \sqrt{\mathbf{A} : \mathbf{A}}$.

Our second kinematic assumption is made with regards to the chemical velocity gradient. Motivated by the conceptual image of the reaction zone shown in Fig. 1, we take the chemical velocity gradient as the additive decomposition of diffusion and reaction induced deformations weighted by the phase-field parameter $\bar{\xi}$. The chemical velocity gradient is taken to be given as

$$\mathbf{L}^{c} = (1 - \bar{\xi})\mathbf{L}^{\alpha,D} + \bar{\xi}(\mathbf{L}^{\beta,D} + \mathbf{L}^{\beta,R}). \tag{3.10}$$

Here:

- (i) $\mathbf{L}^{\alpha,D}$ captures the deformation of the material point due to the diffusion of species in the *unreacted* phase;
- (ii) $\mathbf{L}^{\beta,D}$ captures the deformation of the material point due to the diffusion of species in the *reacted* phase; and
- (iii) $\mathbf{L}^{\beta,R}$ captures the deformation associated with phase transformation due to the chemical reaction.

The three terms in (3.10) are physically understood as the deformations induced by diffusion in either the unreacted or reacted materials and by the phase-transformation due to the ongoing chemical reaction. The scaling by the phase-field parameter $\bar{\xi}$ ensures that in the pristine state ($\bar{\xi} = 0$) chemical distortion is due to only diffusion, while in the fully-reacted state ($\bar{\xi} = 1$) material points are distorted both by the reaction induced phase-transformation and any concurrent and ongoing diffusion.

We further make the pragmatic assumption that chemical deformation is irrotational, ignoring inelastic spins and yielding

$$\mathbf{D}^{c} = (1 - \bar{\xi})\mathbf{D}^{\alpha,D} + \bar{\xi}(\mathbf{D}^{\beta,D} + \mathbf{D}^{\beta,R}). \tag{3.11}$$

We now specify the diffusion induced stretching to be of the form

$$\mathbf{D}^{\alpha,D} = \dot{c}\mathbf{N}^{\alpha,D} \quad \text{and} \quad \mathbf{D}^{\beta,D} = \dot{c}\mathbf{N}^{\beta,D} \tag{3.12}$$

where \dot{c} is the rate of change of the diffusing species and $N^{\alpha,D}$ and $N^{\beta,D}$ are the directions of diffusion induced stretching in the pristine and reacted material, respectively. Similarly, we assume the reaction induced stretching to be based on the extent of the reaction and given by

$$\mathbf{D}^{\beta,R} = \dot{\xi} \mathbf{N}^{\beta,R} \tag{3.13}$$

with $\dot{\xi}$ the reaction rate and $\mathbf{N}^{\beta,R}$ the direction of reaction induced deformations.

Finally, the formulation presented so far makes no assumption regarding the nature of **F**^m; we are free to pick any decomposition regarding the mechanical part of the deformation. We present here for completeness a mechanical distortion which consists of both elastic and plastic components. Hence, we employ a decomposition of the form

$$\mathbf{F}^{\mathbf{m}} = \mathbf{F}^{\mathbf{e}} \mathbf{F}^{\mathbf{p}} \tag{3.14}$$

with F^e the elastic mechanical distortion and F^p the plastic mechanical distortion. We further assume plasticity to be irrotational and volume conserving, that is

$$\mathbf{L}^{p} = \dot{\mathbf{F}}^{p} \mathbf{F}^{p-1} = \mathbf{D}^{p} + \mathbf{W}^{p}, \quad \text{with} \quad \mathbf{W}^{p} = \mathbf{0}, \quad \text{and}$$

$$J^{p} = \det \mathbf{F}^{p} = 1.$$
(3.15)

where $\mathbf{D}^p = \operatorname{sym} \mathbf{L}^p$ and $\mathbf{W}^p = \operatorname{skw} \mathbf{L}^p$. We introduce an equivalent plastic shear strain rate

$$v^{\mathbf{p}} = \sqrt{2}|\mathbf{D}^{\mathbf{p}}| \ge 0,\tag{3.16}$$

and whenever $|\mathbf{N}^p| \neq 0$, introduce the plastic flow direction

$$N^p = \frac{D^p}{|D^p|}. ag{3.17}$$

Use of (3.14) through (3.17) along with (3.12) and (3.13) in (3.11) leads to

$$(\nabla \dot{\chi})\mathbf{F}^{-1} = \dot{\mathbf{F}}^{\mathbf{e}}\mathbf{F}^{\mathbf{e}-1} + \frac{1}{\sqrt{2}}\nu^{\mathbf{p}}\mathbf{F}^{\mathbf{e}}\mathbf{N}^{\mathbf{p}}\mathbf{F}^{\mathbf{e}-1} + (1 - \bar{\xi})\mathbf{F}^{\mathbf{e}}\mathbf{F}^{\mathbf{p}}\left(\dot{c}\mathbf{N}^{\alpha,D}\right)\mathbf{F}^{\mathbf{p}-1}\mathbf{F}^{\mathbf{e}-1} + \bar{\xi}\mathbf{F}^{\mathbf{e}}\mathbf{F}^{\mathbf{p}}\left(\dot{c}\mathbf{N}^{\beta,D} + \dot{\xi}\mathbf{N}^{\beta,R}\right)\mathbf{F}^{\mathbf{p}-1}\mathbf{F}^{\mathbf{e}-1},$$

$$(3.18)$$

which will be of use subsequently.

Before continuing the kinematical description, it is useful to visualize the proposed kinematics as shown schematically in Fig. 2, where (a) shows the kinematic decomposition of F following (3.2), and (b) shows the decomposition of L^c following (3.10). Note that for visual simplification, in Fig. 2 we ignore the diffusion induced deformation $L^{\beta,D}$ in the reacted phase.

3.1. Frame-indifference

We define a change in frame at a fixed time t as the following transformation of spatial points x to new spatial points

$$\mathbf{x}^* = \mathbf{y}(t) + \mathbf{Q}(t)(\mathbf{x} - \mathbf{o}),\tag{3.19}$$

with \mathbf{Q} defined as a rotation, \mathbf{y} as a translation, and \mathbf{o} a fixed spatial origin. Based on Eq. (3.19), the deformation gradient transforms according to

$$\mathbf{F}^* = \mathbf{OF}.\tag{3.20}$$

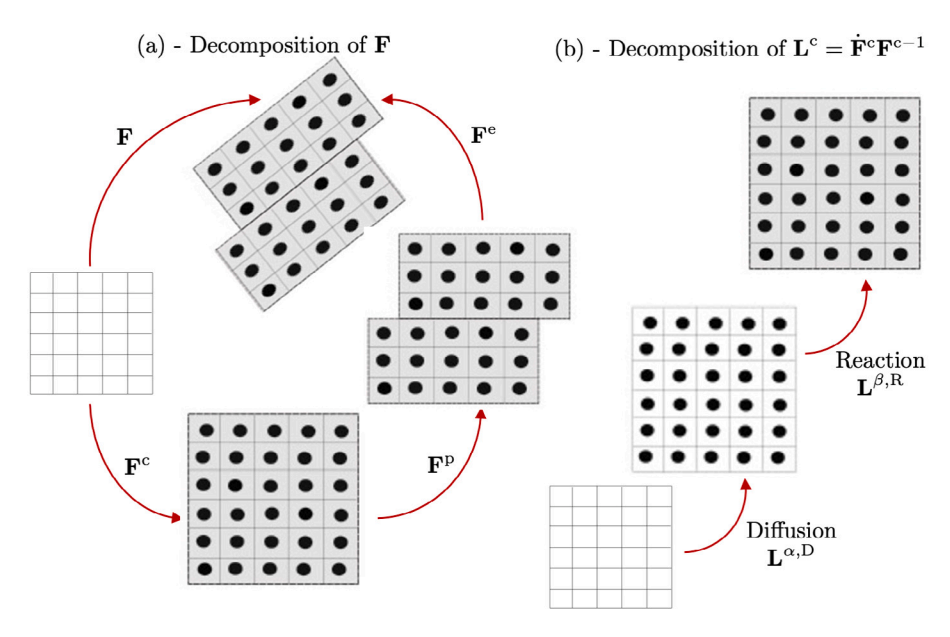


Fig. 2. Schematic representation of the kinematic decompositions assumed. (a) Decomposition $\mathbf{F} = \mathbf{F}^c \mathbf{F}^m = \mathbf{F}^c \mathbf{F}^c \mathbf{F}^p$ of the deformation gradient into chemical and mechanical distortions. (b) Decomposition of the chemical velocity gradient $\mathbf{L}^c = \dot{\mathbf{F}}^c \mathbf{F}^{c-1}$ into diffusion and reaction induced components.

Since the reference configuration and the intermediate structural space do not depend on this change in frame, we have that \mathbf{F}^c and \mathbf{F}^p are invariant under such a change. This leads to

$$(\mathbf{F}^{\mathbf{e}})^* = \mathbf{O}\mathbf{F}^{\mathbf{e}}.\tag{3.21}$$

In a similar fashion, Lc is invariant and

$$(\mathbf{L}^{\mathbf{e}})^* = \mathbf{O}\mathbf{L}^{\mathbf{e}}\mathbf{O}^{\mathsf{T}} + \mathbf{O}\dot{\mathbf{O}},\tag{3.22}$$

which yields

$$(\mathbf{D}^{e})^{*} = \mathbf{Q}\mathbf{D}^{e}\mathbf{Q}^{\mathsf{T}}, \quad (\mathbf{W}^{e})^{*} = \mathbf{Q}\mathbf{W}^{e}\mathbf{Q}^{\mathsf{T}} + \mathbf{Q}\dot{\mathbf{Q}}.$$
 (3.23)

Further, using the polar decomposition we have

$$(\mathbf{F}^{\mathbf{e}})^* = \mathbf{Q}\mathbf{R}^{\mathbf{e}}\mathbf{U}^{\mathbf{e}},\tag{3.24}$$

which based on the uniqueness of polar decomposition yields

$$(\mathbf{R}^{\mathbf{e}})^* = \mathbf{O}\mathbf{R}^{\mathbf{e}},\tag{3.25}$$

and the tensor U^e is invariant. Hence, C^e is also invariant. In addition and for completeness, scalar fields c and ξ , and the referential vector field \mathbf{j}_R are also invariant.

4. Governing balance laws

In this section, we develop the governing equations for our theoretical framework including macroscopic and microscopic force balance and thermodynamic laws.

4.1. Principle of virtual power. Macro and micro force balances

To develop the remaining balance laws in our theoretical framework, we follow the virtual-power approach (cf. Germain, 1973; Gurtin, 2002). This will result in a "macroforce" balance and "microforce" balances for the rate-like kinematical descriptors in our theory. We consider a list of generalized *virtual* velocity fields to be given by

$$\mathcal{V} = (\delta \chi, \delta \mathbf{F}^{\mathbf{e}}, \delta \mathbf{v}^{\mathbf{p}}, \delta c, \delta \xi, \nabla \delta \xi). \tag{4.1}$$

Further, through (3.18), these virtual velocities are constrained by

$$(\nabla \delta \chi)\mathbf{F}^{-1} = \delta \mathbf{F}^{\mathbf{e}}\mathbf{F}^{\mathbf{e}-1} + \frac{1}{\sqrt{2}} \delta \nu^{\mathbf{p}}\mathbf{F}^{\mathbf{e}}\mathbf{N}^{\mathbf{p}}\mathbf{F}^{\mathbf{e}-1} + (1 - \bar{\xi})\mathbf{F}^{\mathbf{e}}\mathbf{F}^{\mathbf{p}} \left(\delta c \mathbf{N}^{\alpha, D}\right) \mathbf{F}^{\mathbf{p}-1}\mathbf{F}^{\mathbf{e}-1} + \bar{\xi}\mathbf{F}^{\mathbf{e}}\mathbf{F}^{\mathbf{p}} \left(\delta c \mathbf{N}^{\beta, D} + \delta \xi \mathbf{N}^{\beta, R}\right) \mathbf{F}^{\mathbf{p}-1}\mathbf{F}^{\mathbf{e}-1}.$$

$$(4.2)$$

For any part P of the body B the internal and external powers are given by

$$\delta W_{\text{ext}}(P, \mathcal{V}) = \int_{\partial P} \mathbf{t}(\mathbf{n}_{R}) \cdot \delta \chi da_{R} + \int_{P} \mathbf{b}_{R} \cdot \delta \chi dv_{R} + \int_{\partial P} \eta \delta \xi da_{R},
\delta W_{\text{int}}(P, \mathcal{V}) = \int_{P} (\mathbf{S}^{e} : \delta \mathbf{F}^{e} + \pi \delta v^{p} + E \delta c + F \delta \xi + \mathbf{G} \cdot \nabla \delta \xi) dv_{R},$$
(4.3)

where we have defined the following macroscopic and microscopic force systems conjugate to the kinematical variables:

- (a) A stress S^e that expends power over the elastic distortion rate \dot{F}^e ;
- (b) A scalar microstress π that expends power over the plastic shearing rate v^p ;
- (c) A traction $\mathbf{t}_{R}(\mathbf{n}_{R})$ (for each unit vector \mathbf{n}_{R}) that expends power over the velocity $\dot{\chi}$;
- (d) A scalar microscopic stress E that expends power over the rate \dot{c} ;
- (e) A scalar microscopic stress F that expends power over the rate $\dot{\xi}$;
- (f) A vector microscopic stress **G** that expends power over the gradient $\nabla \dot{\xi}$; and
- (g) A scalar microscopic traction η that expends power over $\dot{\xi}$ on the boundary of the part.

The principle of virtual power then consistent of: (1) Power balance which requires that $\delta W_{\rm ext}(P,\mathcal{V}) = \delta W_{\rm int}(P,\mathcal{V})$ for all generalized virtual velocities \mathcal{V} and; (2) Frame-indifference which requires that $\delta W_{\rm int}(P,\mathcal{V})$ is invariant under all changes in frame.

Remark 1. In this work we aim to address problems involving sharp interface reactions occurring in solids. Our strategy here is to do this through a phase-field model with the physically motivated extent of reaction ξ as our phase-field variable. In order to implement a diffuse-interface model, we introduce the gradient $\nabla \xi$ of the phase-field parameter as part of the theoretical formulation. First, it allows one to implement wetting (surface energy) boundary conditions through the presence of the traction η expending power over $\dot{\xi}$ on the boundary. Second, the gradient theory will set a finite length scale for our interface and make this theoretical framework amenable to numerical implementation by finite elements.

We begin by using the power balance requirement. First, let $\delta v^p = 0$, $\delta c = 0$, $\delta \xi = 0$, $\nabla \delta \xi = 0$ such that (4.2) yields the relation $\delta \mathbf{F^e} = \nabla \delta \chi \mathbf{F^{-1}F^e}$. For this choice, the principle of virtual power yields

$$\int_{\partial \mathbf{P}} \mathbf{t}(\mathbf{n}_{\mathbf{R}}) \cdot \delta \chi da_{\mathbf{R}} + \int_{\mathbf{P}} \mathbf{b}_{\mathbf{R}} \cdot \delta \chi dv_{\mathbf{R}} = \int_{\mathbf{P}} \mathbf{S}^{\mathbf{e}} : \delta \mathbf{F}^{\mathbf{e}} dv_{\mathbf{R}} = \int_{\mathbf{P}} \mathbf{S}^{\mathbf{e}} \mathbf{F}^{\mathbf{p} - \top} \mathbf{F}^{\mathbf{c} - \top} : \nabla \delta \chi dv_{\mathbf{R}},$$

$$(4.4)$$

which by defining

$$\mathbf{T}_{\mathbf{R}} \stackrel{\text{def}}{=} \mathbf{S}^{\mathbf{e}} \mathbf{F}^{\mathbf{p}-\mathsf{T}} \mathbf{F}^{\mathbf{c}-\mathsf{T}},\tag{4.5}$$

and using the divergence theorem on (4.4) leads to the macroscopic force balance

Div
$$\mathbf{T}_{R} + \mathbf{b}_{R} = 0$$
, and the traction condition $\mathbf{t}_{R}(\mathbf{n}_{R}) = \mathbf{T}_{R}\mathbf{n}_{R}$. (4.6)

As is standard, the Piola stress T_R is related to the symmetric Cauchy stress T through

$$\mathbf{T}_{\mathsf{P}} = J\mathbf{T}\mathbf{F}^{-\mathsf{T}}.\tag{4.7}$$

and for future use we may write $S^e = JTF^{e-T}$.

Now, we let $\nabla \delta \chi = 0$, $\delta c = 0$, $\delta \xi = 0$ such that (4.2) yields the relation $\delta \mathbf{F}^{\mathbf{e}} = -(1/\sqrt{2})\delta v^{\mathbf{p}}\mathbf{F}^{\mathbf{e}}\mathbf{N}^{\mathbf{p}}$. Using this relation, along with $J^{\mathbf{p}} = 1$ from (3.15)₂, we may write the stress power $\mathbf{S}^{\mathbf{e}} : \delta \mathbf{F}^{\mathbf{e}}$ as

$$\mathbf{S}^{\mathbf{e}} : \delta \mathbf{F}^{\mathbf{e}} = -(1/\sqrt{2})\delta \nu^{\mathbf{p}} (\mathbf{F}^{\mathbf{e}^{\mathsf{T}}} \mathbf{S}^{\mathbf{e}}) : \mathbf{N}^{\mathbf{p}} = -(1/\sqrt{2})\delta \nu^{\mathbf{p}} J^{\mathbf{c}} (J^{\mathbf{e}} \mathbf{F}^{\mathbf{e}^{\mathsf{T}}} \mathbf{T} \mathbf{F}^{\mathbf{e}^{\mathsf{T}}}) : \mathbf{N}^{\mathbf{p}}$$

$$= -(1/\sqrt{2})\delta \nu^{\mathbf{p}} J^{\mathbf{c}} \mathbf{M}_{\mathbf{o}}^{\mathbf{e}} : \mathbf{N}^{\mathbf{p}},$$
(4.8)

where we have used the fact that N^p is deviatoric, and have defined the elastic Mandel stress as

$$\mathbf{M}^{\mathbf{e}} \stackrel{\text{def}}{=} J^{\mathbf{e}} \mathbf{F}^{\mathbf{e} \mathsf{T}} \mathbf{T} \mathbf{F}^{\mathbf{e} \mathsf{T}}, \tag{4.9}$$

where \mathbf{M}_{n}^{e} denotes the deviatoric part of \mathbf{M}^{e} . Use of (4.8) and (4.3) yields

$$\int_{\mathbf{R}} (-(1/\sqrt{2})\delta J^{\mathbf{c}} \mathbf{M}_{0}^{\mathbf{e}} : \mathbf{N}^{\mathbf{p}} v^{\mathbf{p}} + \pi \delta v^{\mathbf{p}}) dv_{\mathbf{R}} = 0, \tag{4.10}$$

which must hold for all values of δv^p , yielding the plastic microforce balance

$$\pi = \frac{1}{\sqrt{2}} J^{c} \mathbf{M}_{0}^{e} : \mathbf{N}^{p}. \tag{4.11}$$

The first chemical micro force balance, associated with diffusion, is obtained by letting $\nabla \delta \chi = \mathbf{0}, \delta v^p = 0, \delta \xi = 0$ and $\nabla \delta \xi = 0$ such that (4.2) yields

$$\mathbf{S}^{\mathbf{e}} : \delta \mathbf{F}^{\mathbf{e}} = \mathbf{S}^{\mathbf{e}} : \left(\mathbf{F}^{\mathbf{e}} \mathbf{F}^{\mathbf{p}} \left((1 - \bar{\xi}) \mathbf{N}^{\alpha, D} + \bar{\xi} \mathbf{N}^{\beta, D} \right) \right) \mathbf{F}^{\mathbf{p} - 1} \delta c$$

$$= -(\mathbf{F}^{\mathbf{e}} \mathbf{F}^{\mathbf{p}})^{\mathsf{T}} \mathbf{S}^{\mathbf{e}} \mathbf{F}^{\mathbf{p} - \mathsf{T}} : \left((1 - \bar{\xi}) \mathbf{N}^{\alpha, D} + \bar{\xi} \mathbf{N}^{\beta, D} \right) \delta c$$

$$= -(J^{\mathbf{c}} \mathbf{F}^{\mathbf{p} \mathsf{T}} \mathbf{M}^{\mathbf{e}} \mathbf{F}^{\mathbf{p} - \mathsf{T}}) : \left((1 - \bar{\xi}) \mathbf{N}^{\alpha, D} + \bar{\xi} \mathbf{N}^{\beta, D} \right) \delta c$$

$$(4.12)$$

use of which, along with the power balance statement and (4.3) yields

$$E = J^{c}\mathbf{M}^{m}: \left((1 - \bar{\xi})\mathbf{N}^{\alpha,D} + \bar{\xi}\mathbf{N}^{\beta,D}\right), \tag{4.13}$$

where we have defined the mechanical Mandel stress as

$$\mathbf{M}^{\mathbf{m}} \stackrel{\text{def}}{=} \mathbf{F}^{\mathbf{p}\mathsf{T}} \mathbf{M}^{\mathbf{e}} \mathbf{F}^{\mathbf{p}-\mathsf{T}} = J^{\mathbf{m}} \mathbf{F}^{\mathbf{m}\mathsf{T}} \mathbf{T} \mathbf{F}^{\mathbf{m}-\mathsf{T}}. \tag{4.14}$$

Remark 2. The definition of elastic Mandel stress M^e in (4.9) is identical to that of Anand (2012), written as a pullback operation from the deformed body to the intermediate plastically distorted space. Now, due to the decomposition $F = F^eF^pF^c$, we define an additional mechanical Mandel stress M^m given in (4.14) which is defined through an additional pullback operation from the plastically distorted intermediate space to the chemically distorted intermediate space. This stress is absent in the work of Anand (2012) as it is assumed, from the onset, that chemical expansion is isotropic, making M^e and M^m equal. In our theory, however, chemical expansion is kept general at this point, distinguishing the two stresses. This subtle distinction is important since in Eqs. (4.13) and (4.17) it is the mechanical Mandel stress that is coupled to the chemical driving forces.

The second micro force balance, associated with the reaction, is obtained by letting $\delta \chi = \mathbf{0}, \delta v^p = 0, \delta c = 0$. The virtual power balance statement and (4.3) yields

$$\int_{\partial \mathbf{P}} \eta \delta \xi da_{\mathbf{R}} = \int_{\mathbf{P}} \left(\mathbf{S}^{\mathbf{e}} : \delta \mathbf{F}^{\mathbf{e}} + F \delta \xi + \mathbf{G} \cdot \nabla \delta \xi \right) dv_{\mathbf{R}},
\int_{\partial \mathbf{P}} \eta \delta \xi da_{\mathbf{R}} = \int_{\mathbf{P}} \left(-J^{\mathbf{c}} \bar{\xi} \mathbf{M}^{\mathbf{m}} : \mathbf{N}^{\beta, R} \delta \xi + F \delta \xi + \mathbf{G} \cdot \nabla \delta \xi \right) dv_{\mathbf{R}}.$$
(4.15)

Applying the divergence theorem

$$\int_{\mathbf{P}} \left(-J^{\mathbf{c}} \bar{\xi} \mathbf{M}^{\mathbf{m}} : \mathbf{N}^{\beta, R} \delta \xi + F \delta \xi - \text{Div} \mathbf{G} \delta \xi \right) dv_{\mathbf{R}} = \int_{\partial \mathbf{P}} (\eta - \mathbf{G} \cdot \mathbf{n}_{\mathbf{R}}) \delta \xi da_{\mathbf{R}}, \tag{4.16}$$

which must hold for all values of $\delta \xi$ and yields the second micro force balance

$$F - J^{c}\bar{\epsilon}\mathbf{M}^{\mathbf{m}} : \mathbf{N}^{\beta,R} - \text{Div}\mathbf{G} = 0, \tag{4.17}$$

along with the corresponding boundary condition

$$\eta = \mathbf{G} \cdot \mathbf{n}_{\mathbf{R}}.\tag{4.18}$$

To summarize, using the principle of virtual work we have derived one macroscopic force balance for the Piola stress T_R as well as three microscopic force balances for the stresses π , E, F, and G. The balances are summarized as follows

$$\begin{aligned} &\operatorname{Div} \mathbf{T}_{\mathrm{R}} + \mathbf{b}_{\mathrm{R}} = 0, & \text{with boundary condition} \quad \mathbf{t}_{\mathrm{R}}(\mathbf{n}_{\mathrm{R}}) = \mathbf{T}_{\mathrm{R}}\mathbf{n}_{\mathrm{R}}, \\ &\pi = \frac{1}{\sqrt{2}}J^{\mathrm{c}}\mathbf{M}_{0}^{\mathrm{e}} : \mathbf{N}^{\mathrm{p}}, \\ &E = J^{c}\mathbf{M}^{\mathrm{m}} : \left((1 - \bar{\xi})\mathbf{N}^{\alpha,D} + \bar{\xi}\mathbf{N}^{\beta,D}\right), \\ &F - J^{c}\bar{\xi}\mathbf{M}^{\mathrm{m}} : \mathbf{N}^{\beta,R} - \operatorname{Div}\mathbf{G} = 0, & \text{with boundary condition} \quad \eta = \mathbf{G} \cdot \mathbf{n}_{\mathrm{R}}. \end{aligned}$$

Finally, we discuss the requirement that the internal virtual work $\delta W_{\rm int}(P,\mathcal{V})$ be frame indifferent for all virtual velocities. Given a change of frame, we should have:

$$\delta W_{\text{int}}(P, \mathcal{V}) = \delta W_{\text{int}}^*(P, \mathcal{V}^*) \tag{4.20}$$

where * denote quantities in the new frame. Scalar quantities in (4.3) remain invariant, while δF^e transforms according to

$$(\delta \mathbf{F}^{\mathbf{e}})^* = \mathbf{Q} \delta \mathbf{F}^{\mathbf{e}} + \dot{\mathbf{Q}} \mathbf{F}^{\mathbf{e}} \tag{4.21}$$

under a rotation Q. Following Anand (2012), we also have

$$(\nabla \delta \xi)^* = (\nabla \delta \xi) \tag{4.22}$$

as the gradient operator is in the reference body. We can then write $\delta W_{\rm int}^*(P,\mathcal{V}^*)$ as

$$\delta W_{\text{int}}^*(P, \mathcal{V}^*) = \int_{\mathbf{p}} (\mathbf{S}^{e*} : (\mathbf{Q}\delta \mathbf{F}^e + \dot{\mathbf{Q}}\mathbf{F}^e) + \pi \delta v^p + E\delta c + F\delta \xi + \mathbf{G}^* \cdot (\nabla \delta \xi)) dv_{\mathbf{R}}
= \int_{\mathbf{p}} (\mathbf{Q}^{\mathsf{T}}\mathbf{S}^{e*} : (\delta \mathbf{F}^e + \mathbf{Q}^{\mathsf{T}}\dot{\mathbf{Q}}\mathbf{F}^e) + E\delta c + F\delta \xi + \mathbf{G}^* \cdot (\nabla \delta \xi)) dv_{\mathbf{R}}.$$
(4.23)

Since this should be equal to $\delta W_{\rm int}(P,\mathcal{V})$ by virtue of (4.20), and P is arbitrary, we have

$$\mathbf{Q}^{\mathsf{T}}\mathbf{S}^{\mathsf{e}*}:(\delta\mathbf{F}^{\mathsf{e}}+\mathbf{Q}^{\mathsf{T}}\dot{\mathbf{Q}}\mathbf{F}^{\mathsf{e}})+\mathbf{G}^{*}\cdot(\nabla\delta\xi)=\mathbf{S}^{\mathsf{e}}:\delta\mathbf{F}^{\mathsf{e}}+\mathbf{G}\cdot(\nabla\delta\xi)$$
(4.24)

and since Q is arbitrary, we pick a time independent rotation which yields

$$(\mathbf{S}^{\mathbf{e}} - (\mathbf{O}^{\mathsf{T}} \mathbf{S}^{\mathbf{e}*})) : \delta \mathbf{F}^{\mathbf{e}} + (\mathbf{G} - \mathbf{G}^{*}) \cdot (\nabla \delta \xi) = 0. \tag{4.25}$$

On account of $\delta \mathbf{F}^{e}$ and $\nabla \delta \xi$ being arbitrary we arrive at

$$S^{e*} = QS^{e},$$

$$G^{*} = G.$$
(4.26)

Alternatively, we may assume another rotation of the from Q = 1 with arbitrary skew \dot{Q} , which by virtue of (4.24) leads to

$$\mathbf{S}^{\mathbf{e}}\mathbf{F}^{\mathbf{e}\top}):\dot{\mathbf{Q}}=0\tag{4.27}$$

or equivalently that the stress $S^eF^{e^{\top}}$ must be symmetric. Finally, on account of the discussion above, the Piola stress T_R and Cauchy stress T obey the following transformation rules under a change in frame

$$\mathbf{T}_{p}^{\mathsf{L}} = \mathbf{Q}\mathbf{T}_{\mathsf{R}}, \text{ and } \mathbf{T}^{*} = \mathbf{Q}\mathbf{T}\mathbf{Q}^{\mathsf{T}}.$$
 (4.28)

The elastic Mandel stress Me, and mechanical Mandel stress Mm are invariant under a change in frame.

4.2. Balance of energy. Entropy imbalance. Free energy imbalance

Our discussion of thermodynamics involves the following fields:

- ϵ_{R} the internal energy density per unit reference volume,
- $\eta_{\rm R}$ the entropy density per unit reference volume,
- q_R the heat flux per unit reference area,
- $q_{\rm R}$ the external heat supply per unit reference volume,
- θ the absolute temperature ($\theta > 0$),
- μ the macroscopic chemical potential.

Considering a material region P, we take the balance law for energy as

$$\frac{1}{\int_{\mathbf{P}} \varepsilon_{\mathbf{R}} dv_{\mathbf{R}}} = -\int_{\partial \mathbf{P}} \mathbf{q}_{\mathbf{R}} \cdot \mathbf{n}_{\mathbf{R}} da_{\mathbf{R}} + \int_{\mathbf{P}} q_{\mathbf{R}} dv_{\mathbf{R}} + \mathcal{W}_{\text{ext}}(\mathbf{P}) - \int_{\partial \mathbf{P}} \mu \mathbf{j}_{\mathbf{R}} \cdot \mathbf{n}_{\mathbf{R}} da_{\mathbf{R}}, \tag{4.29}$$

where the last term in (4.29) represents the flux of energy carried into P by the flux of diffusing species. We define the elastic second Piola stress as

$$\mathbf{T}^{e} \stackrel{\text{def}}{=} J^{e} \mathbf{F}^{e-1} \mathbf{T} \mathbf{F}^{e-\top} = \mathbf{C}^{e-1} \mathbf{M}^{e}. \tag{4.30}$$

with $\mathbf{C}^e = \mathbf{F}^{e\top}\mathbf{F}^e$ the elastic right Cauchy–Green tensor. We note that the stress power \mathbf{S}^e : $\dot{\mathbf{F}}^e$ may be written as \mathbf{S}^e : $\dot{\mathbf{F}}^e = (1/2)J^c\mathbf{T}^e$: $\dot{\mathbf{C}}^e$. Next, equating the external power with the internal power, we may write the energy balance as

$$\overline{\int_{\mathbf{P}} \boldsymbol{\varepsilon}_{\mathbf{R}} \, d\boldsymbol{v}_{\mathbf{R}}} = -\int_{\partial \mathbf{P}} \mathbf{q}_{\mathbf{R}} \cdot \mathbf{n}_{\mathbf{R}} \, d\boldsymbol{a}_{\mathbf{R}} + \int_{\mathbf{P}} q_{\mathbf{R}} \, d\boldsymbol{v}_{\mathbf{R}} \\
+ \int_{\mathbf{R}} \left(\frac{1}{2} J^{\mathbf{C}} \mathbf{T}^{\mathbf{e}} : \dot{\mathbf{C}}^{\mathbf{e}} + \pi \boldsymbol{v}^{\mathbf{p}} + E \dot{\boldsymbol{c}} + F \dot{\boldsymbol{\xi}} + \mathbf{G} \cdot \nabla \dot{\boldsymbol{\xi}} \right) d\boldsymbol{v}_{\mathbf{R}} - \int_{\mathbf{n}^{\mathbf{R}}} \mu \mathbf{j}_{\mathbf{R}} \cdot \mathbf{n}_{\mathbf{R}} d\boldsymbol{a}_{\mathbf{R}}, \tag{4.31}$$

which applying the divergence theorem to the boundary integral terms may be written as

$$\int_{\mathbf{p}} \left(\dot{\varepsilon}_{\mathbf{R}} - q_{\mathbf{R}} + \text{Div}\mathbf{q}_{\mathbf{R}} - \frac{1}{2} J^{\mathbf{c}} \mathbf{T}^{\mathbf{e}} : \dot{\mathbf{C}}^{\mathbf{e}} - \pi v^{\mathbf{p}} - E\dot{c} - F\dot{\xi} - \mathbf{G} \cdot \nabla \dot{\xi} + \mu \text{Div}(\mathbf{j}_{\mathbf{R}}) + \mathbf{j}_{\mathbf{R}} \cdot \nabla \mu \right) dv_{\mathbf{R}} = 0. \tag{4.32}$$

Finally, using the balance law (2.2) and the fact that (4.32) must hold for all parts P, we obtain the local form of energy balance as

$$\dot{\varepsilon}_{R} = q_{R} - \text{Div}\mathbf{q}_{R} + \frac{1}{2}J^{c}\mathbf{T}^{e} : \dot{\mathbf{C}}^{e} + \pi\nu^{p} + E\dot{c} + F\dot{\xi} + \mathbf{G} \cdot \nabla\dot{\xi} + \mu(\dot{c} + \dot{\xi}) - \mathbf{j}_{R} \cdot \nabla\mu. \tag{4.33}$$

The local form of the second law takes the form of an entropy imbalance

$$-\theta \dot{\eta}_{\rm R} \le 0 \tag{4.34}$$

which by introducing the Helmholtz free energy, $\psi_R = \epsilon_R - \vartheta \eta_R$, may be written as

$$\dot{\psi}_{R} - \dot{\varepsilon}_{R} + \eta_{R} \dot{\vartheta} \le 0. \tag{4.35}$$

Henceforth in this development we restrict ourselves to isothermal conditions, such that

$$\vartheta \equiv {\rm constant}, \quad q_{\rm R}=0, \quad {\rm and} \quad {\bf q}_{\rm R}=0.$$

Finally, combining the local energy balance (4.33) with the entropy imbalance (4.35) under isothermal conditions yields the local form of the free energy imbalance as

$$\dot{\psi}_{\mathbf{R}} - \frac{1}{2} J^{\mathbf{c}} \mathbf{T}^{\mathbf{e}} : \dot{\mathbf{C}}^{\mathbf{e}} - \pi v^{\mathbf{p}} - E \dot{c} - F \dot{\xi} - \mathbf{G} \cdot \nabla \dot{\xi} - \mu (\dot{c} + \dot{\xi}) + \mathbf{j}_{\mathbf{R}} \cdot \nabla \mu \le 0. \tag{4.37}$$

For later use we define the dissipation density per unit time as

$$\mathcal{D} = \frac{1}{2} J^{c} \mathbf{T}^{e} : \dot{\mathbf{C}}^{e} + \pi v^{p} + E \dot{c} + F \dot{\xi} + \mathbf{G} \cdot \nabla \dot{\xi} + \mu (\dot{c} + \dot{\xi}) - \mathbf{j}_{R} \cdot \nabla \mu \le 0.$$

$$(4.38)$$

Note that all quantities in (4.37) and (4.38) are invariant under a change in frame based on the invariance properties discussed previously.

5. Constitutive theory

We divide the section into energetic and dissipative constitutive equations, along with a discussion on isotropy.

5.1. Energetic constitutive equations

We first consider the following set of constitutive equations for the free energy ψ_R , the stress \mathbf{T}^e , and the chemical potential μ :

$$\psi_{\mathbf{R}} = \hat{\psi}_{\mathbf{R}}(\Lambda)
\mathbf{T}^{\mathbf{e}} = \hat{\mathbf{T}}^{\mathbf{e}}(\Lambda)
\mu = \hat{\mu}(\Lambda)$$
(5.1)

where Λ denotes the list

$$\Lambda = (\mathbf{C}^{\mathbf{e}}, c, \xi, \nabla \xi). \tag{5.2}$$

Using the constitutive Eqs. (5.1), the free-energy imbalance (4.37) may be written as

$$\left(\frac{\partial \hat{\psi}_{R}}{\partial \mathbf{C}^{e}} - \frac{1}{2}J^{c}\mathbf{T}^{e}\right) : \dot{\mathbf{C}}^{e} + \left(\frac{\partial \hat{\psi}_{R}}{\partial c} - E - \mu\right)\dot{c} + \left(\frac{\partial \hat{\psi}_{R}}{\partial \xi} - F - \mu\right)\dot{\xi} + \left(\frac{\partial \hat{\psi}_{R}}{\partial \nabla \xi} - \mathbf{G}\right) \cdot \nabla \dot{\xi} - \pi v^{p} + \mathbf{j}_{R} \cdot \nabla \mu \le 0.$$
(5.3)

In writing (5.3), we make assumptions regarding the dissipative and energetic terms. We make the distinction that processes associated with diffusion (governed by \dot{c}) are energetic, while the ones associated with reaction induced phase change (governed by \dot{c}) are dissipative. An exception to this is the power conjugate to $\nabla \dot{c}$, which is taken to be entirely energetic, i.e all reaction dissipative processes are already accounted for in the \dot{c} term.

As the inequality shown in (5.3) is to hold for all values of \dot{C}^e , \dot{c} , and $\nabla \dot{\xi}$ their "coefficients" must vanish, for otherwise they may be chosen to violate (5.3). We are therefore led to the thermodynamic restriction that the free energy determines the stress T^e , chemical potential μ , and the vector microstress G through the "state relations"

$$T^{e} = 2J^{c-1} \frac{\partial \hat{\psi}_{R}(\Lambda)}{\partial C^{e}},$$

$$\mu = \frac{\partial \hat{\psi}_{R}(\Lambda)}{\partial c} - E,$$

$$G = \frac{\partial \hat{\psi}_{R}(\Lambda)}{\partial \nabla \xi}.$$
(5.4)

5.2. Dissipative constitutive equations

We are now left with the following reduced dissipation inequality

$$\mathcal{D} = -\left(\frac{\partial \hat{\psi}_{\mathbf{R}}(\Lambda)}{\partial \xi} - F - \mu\right)\dot{\xi} + \pi v^{\mathbf{p}} - \mathbf{j}_{\mathbf{R}} \cdot \nabla \mu \ge 0. \tag{5.5}$$

We define the chemical potential of the species of interest in the reacted compound as

$$\mu^{\xi} \stackrel{\text{def}}{=} \frac{\partial \hat{\psi}_{R}(\Lambda)}{\partial \xi} - F, \tag{5.6}$$

which leads to the definition of the thermodynamic driving force for the reaction as

$$\mathcal{F} \stackrel{\text{def}}{=} \mu^{\xi} - \mu, \tag{5.7}$$

and the dissipation inequality (5.5) may now be written as

$$\mathcal{D} = -\mathcal{F}\dot{\xi} + \pi \nu^{p} - \mathbf{j}_{R} \cdot \nabla \mu \ge 0. \tag{5.8}$$

The thermodynamic driving force \mathcal{F} drives the chemical reaction and its specific form and properties will be discussed in detail in subsequent sections. It is worth noting that on one hand, μ controls the diffusion part of the problem from one point to another. On the other hand, \mathcal{F} , which is the difference of μ^{ξ} and μ , controls the reaction part of the problem in a single point. This formulation

encompasses the intuitive understanding that diffusion and reaction processes depend on differences in chemical potentials of the participating species.

Guided by the dissipation inequality (5.8), we first append to the equations in (5.1) a constitutive equation for the flux of diffusion species of the form

$$\mathbf{j}_{R} = -\mathbf{M}_{\text{mob}} \nabla \mu \tag{5.9}$$

where the flux \mathbf{j}_R is linearly proportional to $\nabla \mu$ through the mobility tensor \mathbf{M}_{mob} . Using (5.9) the dissipation inequality may be written as

$$D = -\mathcal{F}\dot{\xi} + \pi v^{p} + \nabla \mu \cdot \mathbf{M}_{\text{mob}} \nabla \mu \ge 0. \tag{5.10}$$

Important to note in Eq. (5.10) is the presence of the first term, denoting reaction induced dissipation. This is consistent with the expectation that even in the absence of plasticity and chemical potential gradients, there can be dissipation due to chemical reactions. Moreover, as a simple constitutive equation for the microforce π we assume

$$\pi = \hat{\pi}(\bar{\gamma}^p) \tag{5.11}$$

with $\bar{\gamma}^p$ the equivalent plastic shear strain.

We further assume that all terms in (5.10) individually satisfy

$$-\mathcal{F}\dot{\xi} \ge 0,$$

$$\pi v^{p} \ge 0,$$

$$\nabla \mu \cdot \mathbf{M}_{\text{moh}} \nabla \mu \ge 0,$$
(5.12)

which leads to the restriction that the mobility tensor \mathbf{M}_{mob} is positive semi-definite. With respect to the chemical reaction dissipation, we assume that $\dot{\xi} > 0$ if and only if $\mathcal{F} < 0$, and vice versa $\dot{\xi} < 0$ if and only if $\mathcal{F} > 0$. Finally, we assume that plastic flow is strongly dissipative and hence that $\hat{\pi}(\bar{\gamma}^p) > 0$. These restrictions ensure that the dissipation inequality (5.10) is not violated.

5.3. Material isotropy

We restrict our theory to isotropic mechanical deformations.² The free energy function $\hat{\psi}_{R}(\Lambda)$ is hence an isotropic function of its arguments:

$$\hat{\psi}_{R}(\mathbf{C}^{e}, c, \xi, \nabla \xi) = \tilde{\psi}_{R}(\mathbf{I}_{\mathbf{C}^{e}}, c, \xi, |\nabla \xi|), \tag{5.13}$$

with the list of principal invariants of Ce given by

$$I_{C^e} = (I_1(C^e), I_2(C^e), I_3(C^e)).$$
 (5.14)

Therefore, T^e is an isotropic function of C^e by virtue of $(5.4)_1$, which in turn leads to symmetry of the elastic Mandel stress due to (4.30).

Now we represent Ce in principal coordinates

$$\mathbf{C}^{\mathbf{e}} = \sum_{i=1}^{3} (\lambda_i^{\mathbf{e}})^2 \mathbf{r}_i \otimes \mathbf{r}_i, \tag{5.15}$$

where λ_i^e and \mathbf{r}_i are eigenvalues and eigenvectors of \mathbf{U}^e , respectively. We may define the elastic logarithmic strain \mathbf{E}^e as

$$\mathbf{E}^{\mathbf{e}} = \ln \mathbf{U}^{\mathbf{e}} = \sum_{i=1}^{3} E_{i}^{\mathbf{e}} \mathbf{r}_{i} \otimes \mathbf{r}_{i} = \sum_{i=1}^{3} \ln \lambda_{i}^{\mathbf{e}} \mathbf{r}_{i} \otimes \mathbf{r}_{i}, \tag{5.16}$$

with E_i^e the principal values of the logarithmic strain. The elastic Mandel stress may then be equivalently calculated as (cf. Anand, 2012)

$$\mathbf{M}^{\mathbf{e}} = J^{\mathbf{c}-1} \sum_{i=1}^{3} \frac{\partial \check{\psi}_{\mathbf{R}}(E_{1}^{\mathbf{e}}, E_{2}^{\mathbf{e}}, E_{3}^{\mathbf{e}}, c, \xi, |\nabla \xi|)}{\partial E_{i}^{\mathbf{e}}} \mathbf{r}_{i} \otimes \mathbf{r}_{i}. \tag{5.17}$$

Finally, with \mathcal{I}_{E^e} the list of principal invariants of E^e , we consider the free-energy a function of $\psi_R(\mathcal{I}_{E^e}, c, \xi, |\nabla \xi|)$ and the elastic Mandel stress is given by

$$\mathbf{M}^{e} = J^{c-1} \frac{\partial \psi_{R}(\mathcal{I}_{E^{e}}, c, \xi, |\nabla \xi|)}{\partial \mathbf{E}^{e}}.$$
(5.18)

The Cauchy and mechanical Mandel stresses are now related to Me through

$$T = J^{e-1}R^{e}M^{e}R^{eT},$$

$$M^{m} = F^{pT}M^{e}F^{p-1}.$$
(5.19)

² Note that other components of the theory, such as diffusion and reaction rate need not be isotropic.

For later use, we also define E_{H}^{e} as the spatial push of the elastic logarithmic strain

$$\mathbf{E}_{H}^{e} = \mathbf{R}^{e} \mathbf{E}^{e} \mathbf{R}^{eT}. \tag{5.20}$$

6. Summary of the general constitutive theory

In this section we summarize our general diffusion-reaction chemo-mechanical theory. The theory relates the following fields:

$\mathbf{x} = \boldsymbol{\chi}(\mathbf{X}, t),$	motion;	
$\mathbf{F} = \nabla \chi, J = \det \mathbf{F} > 0,$	deformation gradient;	
$\mathbf{F} = \mathbf{F}^{\mathbf{m}} \mathbf{F}^{\mathbf{c}},$	multiplicative decomposition of F ;	
$\mathbf{F}^{\mathbf{c}}$, $J^{\mathbf{c}} = \det \mathbf{F}^{\mathbf{c}} > 0$,	chemical distortion;	
$\mathbf{F}^{\mathrm{m}}, J^{\mathrm{m}} = \det \mathbf{F}^{\mathrm{m}} > 0,$	mechanical distortion;	
$\mathbf{F}^{\mathbf{m}} = \mathbf{F}^{\mathbf{e}} \mathbf{F}^{\mathbf{p}},$	elastic-plastic multiplicative	
,	decomposition of F ^m ;	
$\mathbf{F}^{\mathbf{e}}, J^{e} = \det \mathbf{F}^{\mathbf{e}} > 0,$	elastic distortion;	
$\mathbf{F}^{\mathbf{p}}, J^{p} = \det \mathbf{F}^{\mathbf{p}} = 1,$	elastic distortion;	
$\mathbf{L} = \dot{\mathbf{F}}\mathbf{F}^{-1} = \mathbf{L}^{m} + \mathbf{F}^{m}\mathbf{L}^{c}\mathbf{F}^{m-1}$	velocity gradient;	
$\mathbf{L}^{c} = \dot{\mathbf{F}}^{c} \mathbf{F}^{c-1} = \mathbf{D}^{c} + \mathbf{W}^{c} \text{with}$	chemical velocity gradient;	
$\mathbf{W}^{c} = 0$,	
$\mathbf{D}^{c} = (1 - \bar{\xi})\mathbf{D}^{\alpha,D} + \bar{\xi}(\mathbf{D}^{\beta,D} + \mathbf{D}^{\beta,R})$	additive decomposition of the chemical stretching;	
$\mathbf{D}^{\alpha,D} = \dot{c}\mathbf{N}^{\alpha,D},$	diffusion induced chemical stretching of	
	the unreacted phase;	
$\mathbf{D}^{\beta,D} = \dot{c}\mathbf{N}^{\beta,D},$	diffusion induced chemical stretching of	
	the reacted phase;	
$\mathbf{D}^{\beta,R} = \dot{\xi} \mathbf{N}^{\beta,R},$	reaction induced chemical stretching;	
$\mathbf{F}^{\mathbf{e}} = \mathbf{R}^{\mathbf{e}} \mathbf{U}^{\mathbf{e}} = \mathbf{V}^{\mathbf{e}} \mathbf{R}^{\mathbf{e}},$	polar decompositions of F ^e ;	
$\mathbf{C}^{\mathbf{e}} = (\mathbf{F}^{\mathbf{e}})^{T} \mathbf{F}^{\mathbf{e}} = (\mathbf{U}^{\mathbf{e}})^{2},$	right Cauchy–Green tensor;	
$\mathbf{E}^{e} = \ln \mathbf{U}^{e} = \sum_{i=1}^{3} \ln \lambda_{i}^{e} \mathbf{r}_{i} \otimes \mathbf{r}_{i},$	logarithmic elastic strain;	
$\mathbf{E}_{\mathrm{H}}^{\mathrm{e}} = \mathbf{R}^{\mathrm{e}} \mathbf{E}^{\mathrm{e}} (\mathbf{R}^{\mathrm{e}})^{T}.,$	spatial logarithmic elastic strain;	
$\mathbf{T} = \mathbf{T}^{T},$	Cauchy stress;	
$\mathbf{M}^{\mathbf{e}} = J^{\mathbf{e}} \mathbf{F}^{\mathbf{e} \top} \mathbf{T} \mathbf{F}^{\mathbf{e} - \top},$	elastic Mandel stress;	
$\mathbf{M}^{\mathbf{m}} = J^{\mathbf{m}} \mathbf{F}^{\mathbf{m}\top} \mathbf{T} \mathbf{F}^{\mathbf{m}-\top},$	mechanical Mandel stress;	
$\mathbf{T}_{R} = J\mathbf{T}\mathbf{F}^{-T},$	Piola stress;	
$\mathbf{T}_{\mathrm{R}} = J\mathbf{T}\mathbf{F}^{-T},$ $\mathbf{T}^{\mathrm{e}} = J^{\mathrm{e}}\mathbf{F}^{\mathrm{e}-1}\mathbf{T}\mathbf{F}^{\mathrm{e}-T},$	elastic second Piola stress;	
$\psi_{ m R}$,	free energy density per unit reference	
	volume;	
с,	number of moles of diffusing species per	
	unit reference volume;	
ζ,	number of moles of reacted species per	
	unit reference volume;	
$\bar{\xi} = \xi/c_{\text{max}}^{\text{R}} \in [0, 1],$	extent of the reaction;	
$\nabla \xi$,	gradient of reacted species concentration;	
μ ,	chemical potential of the diffusing	
	species;	
$\mathbf{j}_{\mathrm{R}},$	referential species flux vector.	
	-	

6.1. Kinematics

The deformation gradient is decomposed as

$$\mathbf{F} = \mathbf{F}^{\mathbf{m}} \mathbf{F}^{\mathbf{c}} = \mathbf{F}^{\mathbf{e}} \mathbf{F}^{\mathbf{p}} \mathbf{F}^{\mathbf{c}}, \tag{6.1}$$

with $F^m = F^e F^p$ the mechanical distortion, which is further decomposed into elastic and plastic parts. F^c is the chemical distortion. Further, the chemical velocity gradient is $L^c = \dot{F}^c F^{c-1} = D^c$, with the chemical stretching D^c additively decomposed as

$$\mathbf{D}^{c} = (1 - \bar{\xi})\mathbf{D}^{\alpha,D} + \bar{\xi}(\mathbf{D}^{\beta,D} + \mathbf{D}^{\beta,R}), \tag{6.2}$$

where

$$\mathbf{D}^{\alpha,D} = \dot{c}\mathbf{N}^{\alpha,D}, \quad \mathbf{D}^{\beta,D} = \dot{c}\mathbf{N}^{\beta,D}, \quad \text{and} \quad \mathbf{D}^{\beta,R} = \dot{\xi}\mathbf{N}^{\beta,R}. \tag{6.3}$$

In (6.3) the terms $N^{\alpha,D}$ and $N^{\beta,D}$ respectively are the directions of diffusion induced deformations in the unreacted and reacted material. The terms $N^{\beta,R}$ is the direction of reaction induced deformation.

The evolution for $\dot{\mathbf{F}}^p$ is given by $\dot{\mathbf{F}}^p = \mathbf{D}^p \mathbf{F}^p$ with the plastic stretching given by

$$\mathbf{D}^{\mathbf{p}} = \frac{1}{\sqrt{2}} \nu^{\mathbf{p}} \mathbf{N}^{\mathbf{p}}. \tag{6.4}$$

Further, using $(4.19)_2$, the equivalent plastic strain rate v^p is constrained by $(5.12)_3$ to obey

$$(1/\sqrt{2})M_0^a: N^p v^p > 0 \text{ for } v^p > 0, \text{ and } M_0^a: N^p > 0.$$
 (6.5)

with N^p the direction of plastic flow to be constitutively prescribed.

6.2. Constitutive equations

6.2.1. Free energy

The free energy is given by

$$\psi_{\mathbf{R}} = \hat{\psi}_{\mathbf{R}}(I_{\mathbf{F}^{\mathbf{e}}}, c, \xi, |\nabla \xi|),\tag{6.6}$$

where \mathcal{I}_{E^e} is the list of principal invariants of E^e .

6.2.2. Stress

The elastic Mandel stress is given by

$$\mathbf{M}^{\mathbf{e}} = J^{c-1} \frac{\partial \check{\psi}_{\mathbf{R}}(I_{\mathbf{E}^{\mathbf{e}}}, c, \xi, |\nabla \xi|)}{\partial \mathbf{E}^{\mathbf{e}}}, \tag{6.7}$$

with the Cauchy stress given by $\mathbf{T} = J^{e-1}\mathbf{R}^e\mathbf{M}^e\mathbf{R}^{e\mathsf{T}}$, the mechanical Mandel stress by $\mathbf{M}^m = \mathbf{F}^{p\mathsf{T}}\mathbf{M}^e\mathbf{F}^{p\mathsf{-T}}$, and the first Piola stress by $\mathbf{T}_{\mathsf{R}} = J^c\mathbf{F}^{e-\mathsf{T}}\mathbf{M}^e\mathbf{F}^{p\mathsf{-T}}$.

6.2.3. Chemical potential. Flux

Using $(4.19)_3$ in $(5.4)_2$, the chemical potential is given by

$$\mu = \frac{\partial \psi_{\mathbf{R}}}{\partial c} - J^{c} \mathbf{M}^{\mathbf{m}} : \left((1 - \bar{\xi}) \mathbf{N}^{\alpha, D} + \bar{\xi} \mathbf{N}^{\beta, D} \right). \tag{6.8}$$

The referential flux of diffusing species is given by

$$\mathbf{j}_{R} = -\mathbf{M}_{\text{mob}}(c, \xi) \nabla \mu \tag{6.9}$$

with the mobility \mathbf{M}_{mob} a positive semi-definite tensor.

6.2.4. Reaction driving force and kinetics

The reaction kinetics are constrained to obey that $-\mathcal{F}\dot{\xi} \geq 0$. The driving force \mathcal{F} for the chemical reaction is

$$\mathcal{F} = \mu^{\xi} - \mu. \tag{6.10}$$

Combining $(4.19)_4$ and $(5.4)_3$ in (5.6), the chemical potential μ^{ξ} of the species of interest in the reacted compound is

$$\mu^{\xi} = \frac{\partial \psi_{R}}{\partial \xi} - J^{c} \bar{\xi} \mathbf{M}^{m} : \mathbf{N}^{\beta, R} - \text{Div}\left(\frac{\partial \psi_{R}}{\partial \nabla \xi}\right). \tag{6.11}$$

6.3. Governing partial differential equations

The governing equations consist of

1. The local force balance (4.6), viz

$$Div \mathbf{T}_{R} + \mathbf{b}_{R} = 0, \tag{6.12}$$

where $T_R = JTF^{-T}$ is the Piola stress and b_R the body force.

2. The local mass balance (2.2), viz

$$\dot{c} = -\text{Div } \mathbf{j}_{R} - \dot{\xi},\tag{6.13}$$

with the flux j_R described in Section 6.2.3 and the reaction rate $\dot{\xi}$ in Section 6.2.4

3. The reaction kinetics summarized in Section 6.2.4 introduce an additional PDE for the rate of reaction due to dependence of the free energy on the gradient $\nabla \xi$. Using (6.11) in (6.10), the final equation for the reaction kinetics may be given as

$$\dot{\xi} = \check{f}(\mathcal{F}), \quad \text{with} \quad \mathcal{F} = \frac{\partial \psi_{R}}{\partial \xi} - J^{c} \bar{\xi} \mathbf{M}^{m} : \mathbf{N}^{\beta,R} - \text{Div} \left(\frac{\partial \psi_{R}}{\partial \nabla \xi} \right) - \mu, \tag{6.14}$$

where the function $\check{f}(\mathcal{F})$ of \mathcal{F} must obey $-\mathcal{F}\dot{\xi} \geq 0$ in order to satisfy the dissipation inequality (5.12). A number of reaction kinetics may be considered for the function $\check{f}(\mathcal{F})$ which satisfy this constraint, the simplest of which, for example, is a linear relation of the form $\dot{\xi} = -R_0\mathcal{F}$, with R_0 a reaction constant.

Finally, using (5.4)₃ the boundary condition (4.18) for the PDE (6.14) becomes

$$\eta = \frac{\partial \psi_{R}}{\partial \nabla \mathcal{E}} \cdot \mathbf{n}_{R},\tag{6.15}$$

which as noted before will allow us to capture wetting (surface energy) chemical boundary conditions. This type of boundary condition is critical and common even in solid/solid interphases as the fully wetted interface often has the minimum energy (cf. Cogswell and Bazant, 2013 for more details).

7. Specialization of the constitutive equations

The theory presented thus far is quite general. We next present special constitutive equations which are: (i) useful for modeling FeS_2 conversion electrodes as will be done in Section 9, and (ii) provide a clearer understanding of the specific capabilities of the theoretical framework.

7.1. Diffusion and reaction induced deformations

We begin by specifying the manner in which diffusion and reaction of species induce mechanical deformation by specifying the tensors $\{N^{\alpha,D}, N^{\beta,D}, N^{\beta,R}\}$ in (6.3). We now restrict ourselves to problems in which the deformation induced by either diffusion or chemical reactions is *isotropic*.

Consider a generic isotropic volumetric expansion whose volumetric rate of deformation with respect to the variable of interest is constant, that is

$$\mathbf{F} = J^{1/3} \mathbf{1}$$
 with $\frac{dJ}{dc} = \Omega = \text{constant},$ (7.1)

which leads to a simple deformation gradient of the form $\mathbf{F} = (1 + \Omega c)^{1/3} \mathbf{1}$. The rate of stretching of such a deformation gradient is given by

$$\mathbf{D} = \dot{\mathbf{F}}\mathbf{F}^{-1} = \frac{\Omega \dot{c}}{3(1 + \Omega c)}\mathbf{1}.$$
 (7.2)

Motivated by the stretching shown in (7.2), we assume that the directions of diffusion induced stretching in the unreacted and reacted material $N^{\alpha,D}$ and $N^{\beta,D}$, are given by

$$\mathbf{N}^{\alpha,D} = \frac{\Omega_c^{\alpha}}{3(1 + \Omega_c^{\alpha}c)} \mathbf{1}, \quad \text{and} \quad \mathbf{N}^{\beta,D} = \frac{\Omega_c^{\beta}}{3(1 + \Omega_c^{\beta}c)} \mathbf{1}. \tag{7.3}$$

with Ω_c^{α} and Ω_c^{β} constant partial molar volumes associated with the unreacted and reacted phases, respectively. The values Ω_c^{α} and Ω_c^{β} thus quantify the amount of diffusion induced volumetric expansion and may be calculated from experimental observations or ab initio calculations.

Similarly, we restrict ourselves here to isotropic reaction induced deformations and define the direction $N^{\beta,R}$ as

$$\mathbf{N}^{\beta,R} = \frac{\Omega_{\xi}}{3(1 + \Omega_{\tau}\xi)}\mathbf{1},\tag{7.4}$$

with Ω_{ξ} a constant partial molar volume associated with reaction induced deformations. Combining (7.3) and (7.4) in (6.3), the diffusion and reaction induced stretching are given by

$$\mathbf{D}^{\alpha,D} = \frac{\Omega_c^{\alpha}}{3(1 + \Omega_c^{\alpha} c)} \dot{c} \mathbf{1}, \quad \mathbf{D}^{\beta,D} = \frac{\Omega_c^{\beta}}{3(1 + \Omega_c^{\beta} c)} \dot{c} \mathbf{1}, \quad \text{and} \quad \mathbf{D}^{\beta,R} = \frac{\Omega_{\xi}}{3(1 + \Omega_{\xi} \xi)} \dot{\xi} \mathbf{1}. \tag{7.5}$$

7.2. Free energy

The free energy per reference volume is assumed to be separable and of the form

$$\psi_{R}(I_{E^{c}}, c, \xi, |\nabla \xi|) = \psi_{R}^{c}(c, \xi) + \psi_{E}^{\delta}(\xi) + \psi_{R}^{m}(I_{E^{c}}, c, \xi) + \psi_{g}^{g}(|\nabla \xi|).$$
(7.6)

Here:

(i) ψ_R^c is the change in chemical free energy due to mixing of the diffusing species. We take it to be a weighted average of the free energies of the unreacted (denoted by α) and reacted (denoted by β) phases in the material point, with the contribution of each

phase assumed to be given by a regular solution model (cf. DeHoff, 2006). Specifically

$$\psi_{\mathbf{R}}^{c}(c,\xi) = (1 - \bar{\xi})\psi^{c,\alpha}(c) + \bar{\xi}\psi^{c,\beta}(c),$$

$$\psi_{\mathbf{R}}^{c}(c,\xi) = (1 - \bar{\xi})c_{\max}^{\mathbf{D}}\left(\mu_{0}^{\alpha}\bar{c} + R\vartheta\left(\bar{c}\ln\bar{c} + (1 - \bar{c})\ln(1 - \bar{c})\right)\right)$$

$$+ \bar{\xi}c_{\max}^{\mathbf{D}}\left(\mu_{0}^{\beta}\bar{c} + R\vartheta\left(\bar{c}\ln\bar{c} + (1 - \bar{c})\ln(1 - \bar{c})\right)\right).$$
(7.7)

Here, μ_0^{α} and μ_0^{β} are reference potentials of the diffusing species in the unreacted and reacted phases of the host. We define $\bar{c} \stackrel{\text{def}}{=} c/c_{\text{max}}^{\text{D}}$ as the normalized concentration of diffusing species with $c_{\text{max}}^{\text{D}}$ the maximum molar concentration of species which may be hosted in either the pristine or reacted material.³

This expression for the chemical free energy is similar to those used in purely diffusional treatments (cf. DeHoff, 2006), with the difference that the standard state μ_0 differs for the species hosted in either the reacted or unreacted material, and the free energy contributions are averaged through the terms $\bar{\xi}$ and $(1 - \bar{\xi})$. Similar treatment can be found in Guyer et al. (2004).

Remark 3. Note here that in writing (7.7), we assumed that the diffusing species is uniformly distributed over the two phases in the material point. In addition, we make the specific assumption that c_{\max}^D is a constant and hence the unreacted and reacted material may host the same amount of maximum diffusing species. A more general treatment is provided in Appendix A where we distinguish between the concentration of diffusing species in different phases. Appendix A makes clear the particular limiting condition of a uniform concentration of diffusing species within the material point, and how this specific condition yields the free energy (7.7). \square

(ii) ψ_R^{ξ} includes a potential energy function with two local minima associated with the chemical reaction barrier (i.e. chemical activation energy) as well as the reference chemical potential for the species of interest in the reacted compound. It is given by

$$\psi_{R}^{\xi}(\xi) = E^{a} \left(\bar{\xi}\right)^{2} \left(1 - \bar{\xi}\right)^{2} + \xi \mu_{0}^{\xi},\tag{7.8}$$

where the first term follows the work of Guyer et al. (2004) and introduces the reaction barrier E^a in our continuum kinetics formulation,⁴ while the second term sets the reference chemical potential to μ_R^{ξ} . The consequences of including this potential landscape in ψ_R^{ξ} will be shown in detail in the numerical examples to follow. In essence, this function may drive the reactions occurring in the bulk of the solid to occur over a sharp interface, even when a sharp interface is not kinetically preferred. We note that the term $\xi \mu_0^{\xi}$ must be included for it sets the reference potential for μ^{ξ} through (6.11). Note here that μ_0^{ξ} denotes the reference potential of the species when it is chemically reacted and part of the new compound, while μ_0^{β} denotes the reference potential of the species when it is merely diffusing through the new compound.

(ii) ψ_R^m is the contribution to changes in the free energy due to the elastic deformation of the host electrode material. It is taken to be given by

$$\psi_{\mathbf{R}}^{\mathbf{m}}(\mathbf{E}^{\mathbf{e}}, c, \xi) = J^{\mathbf{c}} \left[\frac{1}{2} \mathbf{E}^{\mathbf{e}} : \mathbb{C}(c, \xi)[\mathbf{E}^{\mathbf{e}}] \right], \tag{7.9}$$

where

$$\mathbb{C}(c,\xi) \stackrel{\text{def}}{=} 2G(c,\xi)\mathbb{I} + \left(K(c,\xi) - \frac{2}{3}G(c,\xi)\right)\mathbf{1} \otimes \mathbf{1},\tag{7.10}$$

is the elasticity tensor, with \mathbb{I} and 1 the fourth- and second-order identity tensors. The shear and bulk moduli are assumed to obey the following interpolation (cf. Loeffel et al., 2013)

$$G(c,\xi) = (1 - \bar{\xi})G_{\alpha}(c) + \bar{\xi}G_{\beta}(c),$$

$$K(c,\xi) = (1 - \bar{\xi})K_{\alpha}(c) + \bar{\xi}K_{\beta}(c),$$
(7.11)

where G(c) and K(c) are concentration-dependent shear and bulk moduli and the subscripts α and β denote that these belong to either the unreacted or reacted phases of the solid.

(iv) ψ_{R}^{g} is the interfacial free energy that penalizes sharp interfaces in the bulk and is simply taken as

$$\psi_{\mathbf{R}}^{g}(|\nabla \xi|) = \frac{1}{2}\lambda |\nabla \xi|^{2},\tag{7.12}$$

with λ a gradient energy coefficient.

As noted in Remark 1 in Section 4.1, one of the features of the gradient phase-field model developed here is that it will allow us to set a finite interface width, making the framework amenable to numerical solutions using finite elements. The parameter λ will thus control the minimum width of the interface.

³ One could replace concentrations here by activity coefficients to account for deviations from ideal behavior, as is done for example in the work of Bazant (2013).

⁴ Note that the polynomial function serves to introduce the energy barrier, and not to model phase separation through spinodal decomposition.

Finally, using (7.7) through (7.12) in (7.6), the total free energy which accounts for the combined effects of mixing (diffusion), reactions, and finite elastic deformations is given by

$$\psi_{R} = \left(1 - \bar{\xi}\right) c_{\max}^{D} \left(\mu_{0}^{\alpha} \bar{c} + R \,\theta \left(\bar{c} \ln \bar{c} + (1 - \bar{c}) \ln(1 - \bar{c})\right)\right)
+ \bar{\xi} c_{\max}^{D} \left(\mu_{0}^{\beta} \bar{c} + R \,\theta \left(\bar{c} \ln \bar{c} + (1 - \bar{c}) \ln(1 - \bar{c})\right)\right) + \xi \mu_{0}^{\xi}
+ J^{c} \left[\frac{1}{2} \mathbf{E}^{e} : \mathbb{C}(c, \xi) [\mathbf{E}^{e}]\right] + E^{a} \bar{\xi}^{2} (1 - \bar{\xi})^{2} + \frac{1}{2} \lambda |\nabla \xi|^{2}.$$
(7.13)

Remark 4. In the sections that follow we will take derivatives of the free energy ψ_R given by (7.13) with respect to the concentration of diffusing species c and the reaction coordinate ξ . In doing so, we will neglect the derivative of J^c which is present in the mechanical free energy ψ_R^m given by (7.9) with respect to those quantities. We note that derivatives of J^c will be multiplied by a term which is quadratic in the mechanical logarithmic strains, in large part this motivates our neglect of this derivative. Given the finite strain nature of this framework, it is possible for these quadratic terms to not be insignificant. Nonetheless, we chose to ignore this particular derivative so as not to obfuscate the more relevant physics discussed next.

7.3. Stress

The elastic Mandel stress is obtained using (7.13) in (6.7) as

$$\mathbf{M}^{e} = 2G(c,\xi)\mathbf{E}^{e} + \left(K(c,\xi) - (2/3)G(c,\xi)\right)(\text{tr}\mathbf{E}^{e})\mathbf{1},\tag{7.14}$$

and the Cauchy, Piola, and mechanical Mandel stresses are given by

$$\mathbf{T} = J^{e-1} \left[2G(c, \xi) \mathbf{E}_{H}^{e} + \left(K(c, \xi) - (2/3)G(c, \xi) \right) (\text{tr} \mathbf{E}_{H}^{e}) \mathbf{1} \right],$$

$$\mathbf{T}_{R} = J^{c} \mathbf{F}^{e-T} \mathbf{M}^{e} \mathbf{F}^{p-T},$$

$$\mathbf{M}^{m} = \mathbf{F}^{pT} \mathbf{M}^{e} \mathbf{F}^{p-T}.$$

$$(7.15)$$

with $E_{\mbox{\scriptsize H}}^{e}$ the spatial logarithmic elastic strain.

7.4. Chemical potential. Flux

Using (7.13) in (6.8), the chemical potential for the diffusing species is given by

$$\mu = (1 - \bar{\xi})\mu_0^{\alpha} + \bar{\xi}\mu_0^{\beta} + R\theta \ln\left(\frac{\bar{c}}{1 - \bar{c}}\right) - J^{c}\mathbf{M}^{m} : \left((1 - \bar{\xi})\mathbf{N}^{\alpha, D} + \bar{\xi}\mathbf{N}^{\beta, D}\right), \tag{7.16}$$

where in writing the above we neglect contributions arising from derivatives of the elasticity tensor \mathbb{C} with respect to c since these are quadratic in strain.

We specialize the flux of diffusing species to be *isotropic* and write (6.9) as

$$\mathbf{j}_{R} = -\hat{m}(c, \xi) \nabla \mu, \tag{7.17}$$

with the mobility m given by

$$\hat{m}(c,\xi) = \hat{m}_0(\xi)c(1-\bar{c}), \quad \text{with} \quad \hat{m}_0(\xi) = (1-\bar{\xi})m_0^\alpha + \bar{\xi}m_0^\beta > 0. \tag{7.18}$$

Here m_0^{α} and m_0^{β} are related to the diffusivities through the standard relations

$$m_0^{\alpha} = \frac{D_0^{\alpha}}{R_0}$$
, and $m_0^{\beta} = \frac{D_0^{\beta}}{R_0}$, (7.19)

with D_0^{α} and D_0^{β} the diffusivity of the diffusing species in the unreacted and reacted phases, respectively.

7.5. Reaction driving force and kinetics

As mentioned in the introduction, one of the objectives of this theoretical framework is to provide a thermodynamically consistent field treatment for chemical reactions, and the associated mechanical deformations, in solids. The general chemical reaction driving force \mathcal{F} is given by (6.10), with the chemical potential μ^{ξ} of the reacted species given by (6.11). The chemical potential landscape is conceptualized in Fig. 3. In this potential, we assume the generic reaction $A + C \rightarrow B$ occurs through a process of the form

$$A + C \to AC \to B \tag{7.20}$$

where we define a transition state $\psi^{\ddagger}/(R\theta)$ for the chemical reaction. As shown in the right of Fig. 3, the reaction evolves first through $A+C \to AC$ to reach the activated state, and subsequently through $AC \to B$ whereby the new β phase forms. This treatment

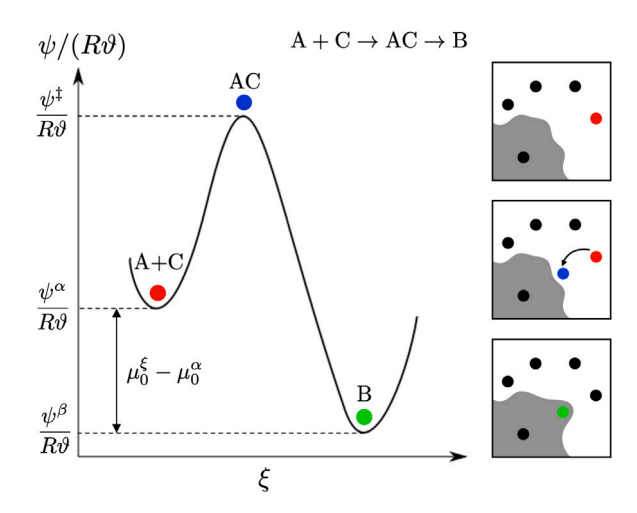


Fig. 3. Conceptual potential landscape for the chemical reaction. An atom leaves the unreacted α phase of the reaction zone and moves to the vicinity of the reacted phase in the activated state, A+C \rightarrow AC. Subsequently, the activated complex reacts forming the additional β phase, AC \rightarrow B. Additional diffusing atoms are present in both phases.

is motivated on the theory of chemical kinetics formulated by Bazant and co workers (Bazant, 2013), and is adopted here for a field treatment in continuum mechanics with mechanical coupling. A different formulation of stress modulating rate kinetics can also be found in the work of Ghasemi and Gao (2020).

Thus, the overarching idea is that there is a *global driving force* between the chemical potentials of the reacted and unreacted materials $(\mu_0^{\xi} - \mu_0^{\alpha})$ which drives the reaction forwards (or backwards) and a local driving force due to the transition state *energy barrier*, characterized by E^a in (7.13), which drives the reaction towards the local minima. These terms are further detailed with respect to the final specialized form of the driving force.

Using (7.13) in (6.11) yields μ^{ξ} as

$$\mu^{\xi} = \frac{c_{\max}^{\mathrm{D}}}{c_{\max}^{\mathrm{R}}} \left(-\mu_0^{\alpha} + \mu_0^{\beta} \right) \bar{c} + \mu_0^{\xi} + \frac{d}{d\xi} \left(E^{\mathrm{a}} \bar{\xi}^2 (1 - \bar{\xi})^2 \right) - J^c \bar{\xi} \mathbf{M}^{\mathrm{m}} : \mathbf{N}^{\beta, R} - \mathrm{Div}(\lambda \nabla \xi).$$
 (7.21)

Combining (7.21) along with μ from (7.16) in (6.10) yields

$$\mathcal{F} = \mu^{\xi} - \mu$$

$$= \frac{c_{\text{max}}^{D}}{c_{\text{max}}^{R}} \left(-\mu_{0}^{\alpha} + \mu_{0}^{\beta} \right) \bar{c} + \mu_{0}^{\xi} + \frac{d}{d\xi} \left(E^{a} \bar{\xi}^{2} (1 - \bar{\xi})^{2} \right) - J^{c} \bar{\xi} \mathbf{M}^{m} : \mathbf{N}^{\beta, R} - \text{Div}(\lambda \nabla \xi)$$

$$- (1 - \bar{\xi}) \mu_{0}^{\alpha} - \bar{\xi} \mu_{0}^{\beta} - R \theta \ln \left(\frac{\bar{c}}{1 - \bar{c}} \right) + J^{c} \mathbf{M}^{m} : \left((1 - \bar{\xi}) \mathbf{N}^{\alpha, D} + \bar{\xi} \mathbf{N}^{\beta, D} \right), \tag{7.22}$$

which after rearranging may be written in the following useful form

$$E = \mu^{\xi} - \mu$$

$$= \underbrace{\frac{1}{c_{\max}^{R}} \left(c - \xi \right) \left(\mu_{0}^{\beta} - \mu_{0}^{\alpha} \right) + \left(\mu_{0}^{\xi} - \mu_{0}^{\alpha} \right)}_{\text{energetic}} + \underbrace{\frac{d}{d\xi} \left(E^{a} \bar{\xi}^{2} (1 - \bar{\xi})^{2} \right)}_{\text{entropic}} - \underbrace{R\vartheta \ln \left(\frac{\bar{c}}{1 - \bar{c}} \right)}_{\text{entropic}}$$

$$+ \underbrace{J^{c} \mathbf{M}^{m} : \left((1 - \bar{\xi}) \mathbf{N}^{\alpha, D} + \bar{\xi} \mathbf{N}^{\beta, D} - \bar{\xi} \mathbf{N}^{\beta, R} \right)}_{\text{mechanical}} - \underbrace{Div(\lambda \nabla \xi)}_{\text{numerical regularization}}$$
(7.23)

In (7.23) we have identified the following therms. The first two terms represent the energetic difference between the species, comprising two distinct effects: (i) $(\mu_0^\alpha - \mu_0^\beta)$ denotes the difference between reference potentials of the species diffusing in the reacted and unreacted phase. Physically, this term captures the fact that the reaction driving force may be influenced by the diffusion reference potentials since it may be energetically preferable from a diffusion perspective to react to a phase which has lower reference potential for diffusion. Similarly, this term may retard the reaction if the converse is true. (ii) $(\mu_0^\xi - \mu_0^\alpha)$ denotes the difference between reference potentials of the species diffusing in the unreacted material and the species which is a part of the reacted compound, and naturally drives the reaction forward if the chemical potential of the reacted compound is lower. This whole energetic term acts as a global driving force. In order to gain more insight on the nature of this term, we consider two special cases:

• Case 1: $\mu_0^{\alpha} = \mu_0^{\beta}$ which implies that the reference potentials for diffusion in both phases are equal at a material point. Conceptually, this means there is no energetic preference for the species diffusing in either phase and hence there is no

energetic contribution towards enhancing or retarding the reaction. In this particular case, the energetic term in (7.23) reduces to $(\mu_0^{\xi} - \mu_0^{\alpha})$ and it is only the difference in reference potentials between the diffusing species and the species which is part of the reacted compound that governs the energetic term.

• Case 2: $\mu_0^0 = \mu_0^\xi$ which implies that the reference potential for the species is the same whether it is diffusing through the reacted phase or part of the reacted compounds. In this particular case, the energetic term in (7.23) reduces to $(c/c_{\text{max}}^R + (1 - \bar{\xi})) (\mu_0^\xi - \mu_0^\alpha)$, which has a form familiar in the literature. In the chemo-mechanics literature, one usually finds a term of the form $H(1 - \bar{\xi})$ introduced through a harmonic free energy of the form $(1/2)H(1 - \bar{\xi})^2$ as first proposed by Ulm et al. (2000) and subsequently adopted in a number of publications (cf. Loeffel and Anand, 2011; Konica and Sain, 2020; Cui et al., 2020; Zhao et al., 2019a). Here, this term arises naturally without the introduction of the "chemical modulus" H, as the energetic difference between unreacted and reacted states. A particular benefit, as used in Section 9, is that this modulus may be determined in straightforward fashion from experimentally measured energies for any given reaction. To be in line with the published literature, this is the special case we will use for our numerical simulations in Section 9.

The second term is an activation energy barrier associated with the energy of the transition state, and characterized by the energy E^a . This term has a significant impact on the sharp-interface nature of the reaction front. This term acts as a local driving force for the chemical reaction and drives the reaction towards the two energy minima. The energy E^a in this term may also be determined experimentally or from ab initio calculation for a given chemical reaction.

The third term captures the role of configurational entropy and drives the reaction towards maximum entropy. The fourth term captures the effect of mechanical stress on the reaction driving force. The final term in (7.23) arises from the gradient phase-field nature of the theory and regularizes the interface width, setting a minimum width controlled by λ .

Remark 5. The theoretical framework summarized in Section 6 above and specialized here, can also be considered as a special case, under specific constraints, of a more general framework in which one treats the diffusion of species through the α and β phases of unreacted and reacted material separately. Specifically, Appendix A demonstrates that the framework presented here is a *limiting case* of the more general formulation under two conditions that the chemical potentials of the diffusing species in the two phases are *in equilibrium*, and the concentration of diffusing species within the material point is *uniformly distributed*.

An additional feature of the reaction driving force \mathcal{F} in (7.23) is that in order for the dissipative constraint (5.12)₁ to hold, there is a critical concentration of the diffusing species below which the reaction will not initiate. The existence of such a threshold concentration is shown by first principles calculations in the work of Wan et al. (2010), and is reproduced here from a continuum thermodynamics approach. The critical concentration for reaction initiation, \bar{c}_{crt} , is found by solving (7.23) for the case of $\mathcal{F}=0$. As a demonstration, consider the *stress-free* case $\mathbf{M}^{\mathbf{m}}=\mathbf{0}$ where in addition we assume no gradients $\nabla \xi=0$. For such a case, the critical concentration \bar{c}_{crt} depends on the difference $(\mu_0^{\xi}-\mu_0^{\alpha})$ and the ratio c_{max}^D/c_{max}^R . The specific values are shown in Fig. 4. As expected, for the case of $(\mu_0^{\xi}-\mu_0^{\alpha})/(R\theta)=0$ the critical concentration depends only on the entropic part of (7.23) and is equal to $\bar{c}_{crt}=0.5$, which corresponds to the maximum entropy of an ideal mixture. As $(\mu_0^{\xi}-\mu_0^{\alpha})/(R\theta)$ increases, the critical concentration drops rapidly, which is the case for most experimentally relevant reactions.

Having discussed the reaction driving force \mathcal{F} , we now specify the reaction kinetics equation. We now restrict ourselves to modeling only *forward reactions* (i.e. $\dot{\xi} > 0$). The simplest form of the reaction kinetics which satisfies the dissipative constraint $(5.12)_1$ is a linear relationship of the form

$$\dot{\xi} = \begin{cases} -R_0 \mathcal{F}, & \text{if } \bar{\xi} < 0, \\ 0, & \text{if } \bar{\xi} = 1, \end{cases}$$
 (7.24)

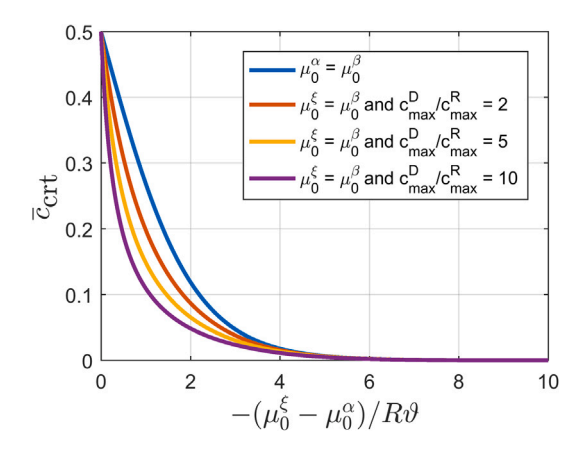


Fig. 4. Critical concentration for reaction initiation, $\bar{c}_{\rm crt}$, as a function of energetic difference $(\mu_0^{\ell} - \mu_0^a)$, plotted for both the case of $(\mu_0^a = \mu_0^{\ell})$ and the case of $(\mu_0^{\ell} = \mu_0^{\ell})$. For the case of $(\mu_0^{\ell} = \mu_0^{\ell})$, the critical concentration depends also on the maximum reaction to diffusion concentrations ratio, $c_{\rm max}^{\rm D}/c_{\rm max}^{\rm R}$. For most practical chemical reactions, the energetic difference $(\mu_0^{\ell} - \mu_0^a)$ is much larger than thermal energy $R\theta$.

with $R_0 > 0$ a positive reaction rate constant.

Remark 6. Although, for simplicity, a linear relationship as shown in (7.24) is used here, the theoretical framework is general and may accommodate any form of non-linear kinetics which satisfies the dissipative constraint (5.12)₁. For example one may define forwards and backwards non-linear reaction kinetics of the form

$$\dot{\xi} = \begin{cases} R_{0 \to} \left(\exp\left(\frac{-\alpha \mathcal{F}}{R \vartheta}\right) - 1 \right) & \text{if } \mathcal{F} < 0, \\ R_{0 \leftarrow} \left(1 - \exp\left(\frac{(1 - \alpha)\mathcal{F}}{R \vartheta}\right) \right), & \text{if } \mathcal{F} > 0, \end{cases}$$
 (7.25)

where $R_{0\rightarrow}$ and $R_{0\leftarrow}$ are forward and backward reaction rates, and $\alpha \in (0,1)$ is a symmetry factor. For the particular case of $R_0 = R_{0\rightarrow} = R_{0\leftarrow}$ this yields

$$\dot{\xi} = R_0 \left(\exp\left(\frac{-\alpha F}{R\theta}\right) - \exp\left(\frac{(1-\alpha)F}{R\theta}\right) \right). \tag{7.26}$$

which is the well-known Butler–Volmer kinetics. Further, we note that while in this work we only simulate forward reactions in the numerical examples provided in Section 9, both backward and forward reaction may be captured using the kinetics shown in (7.25) with the additional condition that $\dot{\xi} = 0$ if $\bar{\xi} = 0$ or $\bar{\xi} = 1$.

7.6. Plastic constitutive equations

Here we utilize the classical J_2 plasticity theory. We adopt the classical codirectionality hypothesis whereby the plastic flow direction N^p is codirectional with the deviatoric elastic Mandel stress M^e

$$Np = \frac{\mathbf{M}_0^e}{|\mathbf{M}_0^e|}, \text{ and hence } \mathbf{D}^p = \frac{1}{\sqrt{2}} v^p \frac{\mathbf{M}_0^e}{|\mathbf{M}_0^e|},$$
(7.27)

where we have used (6.4). We define an equivalent shear stress

$$\bar{\tau}_{\mathrm{p}} \stackrel{\mathrm{def}}{=} \frac{1}{\sqrt{2}} |\mathbf{M}_{0}^{\mathrm{e}}|,\tag{7.28}$$

such that the constitutive equation for the microforce balance (4.19)2 may be written as

$$\bar{\tau}_{\rm p} = Y(\bar{\gamma}^p) \quad \text{when} \quad v^p > 0, \tag{7.29}$$

where $Y(\bar{\gamma}^p) > 0$ is the yield stress of the material, taken here to depend only on the equivalent plastic shear strain $\bar{\gamma}^p$. In combination these satisfy the constraints (6.5) arising from the dissipation inequality. The loading–unloading condition naturally follows as

$$v^p \ge 0, \quad f \le 0, \quad v^p f = 0,$$
 (7.30)

where $f = \bar{\tau}_p - Y(\bar{\gamma}^p)$ is the yield function. Finally, the consistency condition of (7.30) can be written as

$$v^p \dot{f} = 0$$
 when $f = 0$. (7.31)

8. Governing partial differential equations for the specialized constitutive equations. Boundary conditions

The final set of governing partial differential equations consist of:

1. The local macroscopic force balance, Eq. (6.12), viz.

$$Div T_{p} + b_{p} = 0, \tag{8.1}$$

where T_R given by $(7.15)_2$, and b_R is the non-inertial body force.

2. The local mass balance for the diffusing species (6.13) which together with the flux (7.17) gives

$$\dot{c} = \operatorname{Div}(m\nabla \mu) - \dot{\xi} \tag{8.2}$$

with the mobility m given in (7.18), the chemical potential in (7.16) and the reaction kinetics governed by the PDE (8.3)

3. The reaction kinetics are governed by (7.24) which using the driving force (7.23) for the special case $\mu_0^{\beta} = \mu_0^{\xi}$ yields the governing PDE for the reaction kinetics as

$$\dot{\xi} = -R_0 \mathcal{F}, \quad \text{with}$$

$$\mathcal{F} = \left(\frac{c_{\text{max}}^{\text{D}}}{c_{\text{max}}^{\text{R}}} \bar{c} + (1 - \bar{\xi})\right) (\mu_0^{\xi} - \mu_0^{\alpha}) + \frac{E^{\alpha}}{c_{\text{max}}^{\text{R}}} (2\bar{\xi} - 6\bar{\xi}^2 + 4\bar{\xi}^3) - R\vartheta \ln \left(\frac{\bar{c}}{1 - \bar{c}}\right)$$

$$+ J^{c} \mathbf{M}^{\mathbf{m}} : \left((1 - \bar{\xi})\mathbf{N}^{\alpha, D} + \bar{\xi}\mathbf{N}^{\beta, D} - \bar{\xi}\mathbf{N}^{\beta, R}\right) - \text{Div}(\lambda \nabla \xi),$$
(8.3)

which in this particular framework is a PDE due to the presence of the $\text{Div}(\nabla \xi)$ term in the driving force \mathcal{F} . Following (7.24), these kinetics also obey the condition $\dot{\xi} = 0$ when $\bar{\xi} = 1$, which marks the end of the reaction.

Finally, we need initial and boundary conditions to complete the model. We define S_1 and S_2 to be complementary subsurfaces of the boundary ∂B of the body B, i.e. $\partial B = S_1 \cup S_2$ and $S_1 \cap S_2 = \emptyset$. In a similar fashion, S_μ and $S_{\bf j}$ are defined as complementary subsurfaces of the boundary: $\partial B = S_\mu \cup S_{\bf j}$ and $S_\mu \cap S_{\bf j} = \emptyset$, and finally let S_ξ and S_η are also complementary subsurfaces of the boundary: $\partial B = S_\xi \cup S_\eta$ and $S_\xi \cap S_\eta = \emptyset$. In a time interval $t \in (0,T)$ then the deformation is specified on S_1 and the surface traction on S_2 as:

$$\chi = \check{\chi} \quad \text{on} \quad S_1 \times (0, T),
\mathbf{T}_R \mathbf{n}_R = \check{\mathbf{t}}_R \quad \text{on} \quad S_2 \times (0, T);$$
(8.4)

while the chemical potential is specified on boundary \mathcal{S}_{μ} and the species flux on boundary $\mathcal{S}_{\mathbf{j}}$

$$\mu = \check{\mu} \quad \text{on} \quad S_{\mu} \times (0, T),$$

$$\mathbf{j}_{R} \cdot \mathbf{n}_{R} = \check{\mathbf{j}}_{R} \quad \text{on} \quad S_{\mathbf{j}} \times (0, T);$$

$$(8.5)$$

and similarly the reaction is specified on boundaries S_{ξ} and the wetting boundary condition on S_{η} .

$$\xi = \xi \quad \text{on} \quad S_{\xi} \times (0, T),$$

$$\lambda \nabla \xi \cdot \mathbf{n}_{R} = \check{\eta} \quad \text{on} \quad S_{\eta} \times (0, T).$$

$$(8.6)$$

The initial conditions is also written as

$$\chi(X, 0) = \chi_0(X)$$
, and $\mu(X, 0) = \mu_0(X)$ and $\xi(X, 0) = \xi_0(X)$ in B. (8.7)

The coupled set of PDEs (8.1)–(8.3), along with boundary conditions (8.4)–(8.6), and initial conditions (8.7) give an initial/boundary-value problem for the unknowns of motion $\chi(\mathbf{X},t)$, the chemical potential $\mu(\mathbf{X},t)$, and the extent of the reaction $\xi(\mathbf{X},t)$.

9. Numerical simulations

In this Section we detail a set of numerical simulations aimed at both highlighting the important features of our theoretical framework and addressing an engineering problem of relevance. The theoretical framework is implemented in Abaqus Standard (Simulia, 2010) with a custom user-element (UEL) subroutine. In order to make the theoretical framework more amenable to numerical implementation, we have utilized the so called "micromorphic" formulation (cf. Forest, 2009; Di Leo et al., 2014; Di Leo, 2015) where an auxiliary variable is introduced to ease numerical convergence. Complete details of the numerical implementation are presented in Appendix B. We emphasize that the use of this particular numerical technique does not affect the numerical results and produces equivalent outputs as would be generated with a direct implementation of the coupled PDEs in question.

We present three sets of numerical simulations in the subsequent sections. In Section 9.1 we present simulations which are purely chemical (i.e. no mechanical deformation or stress generation) to demonstrate the manner in which the theory captures the formation and evolution of sharp reaction interfaces which are either kinetically or thermodynamically driven. In Section 9.2 we address an engineering problem of relevance, namely we perform three-dimensional simulations of the reaction of FeS_2 crystals with either Li or Na ions. In particular, we demonstrate the manner in which the theoretical framework may be calibrated in straightforward fashion. Subsequently, we demonstrate the role of mechanical deformation and stress on determining the morphology of reaction front with good qualitative agreement with experiments. Finally, in Section 9.3 we present a set of numerical results to elucidate the role and importance of surface wetting (surface energy) boundary conditions in modeling the aforementioned FeS_2 crystals undergoing chemical reactions.

9.1. Modeling sharp interface reactions in the absence of mechanical coupling

In this section we focus on purely chemical (i.e. diffusion–reaction) simulations and neglect all mechanical deformation and stress terms in the theoretical framework. Here we demonstrate the mechanisms which control the formation of a sharp interface during the diffusion–reaction process. In particular, we explore the manner in which reaction vs. diffusion kinetics affect sharp interface formation and the role of the energy barrier introduced in the free energy. We model a quarter of a two-dimensional square simulation domain and mesh it with 10 000 elements. Consistent with modeling a quarter simulation domain, elements on the external boundaries are prescribed a constant flux while elements on the mirrored (internal) boundaries are prescribed zero flux. So as to focus on the terms controlling sharp interface reaction kinetics, in this section we apply zero wetting (surface energy) boundary conditions (i.e. $\eta = 0$ in (8.6)₂). The energetic driving force and ratio of maximum species hosted through diffusion and consumed during the reaction in (7.23) are taken as

$$\frac{\mu_0^{\xi} - \mu_0^{\alpha}}{R\theta} = 5 \quad \text{and} \quad \frac{c_{\text{max}}^D}{c_{\text{max}}^R} = 1, \tag{9.1}$$

with $R\theta$ the thermal energy. To characterize the diffusion kinetics, reaction kinetics, and the activation energy barrier we introduce the non-dimensional quantities

$$\frac{R_0 L^2}{D_0}$$
 and $\frac{E^a}{R \theta c_{\text{max}}^R}$, (9.2)

where R_0 is the reaction rate in (7.24), D_0 is the diffusivity in (7.19) and assumed here to be the same for reacted and unreacted materials, L is the length of the simulation domain, E^a is the activation energy in (7.23), $R\theta$ is the thermal energy with R the gas constant and θ the absolute temperature, and c_{\max}^R is the maximum molar concentration of species consumed during chemical reaction. The quantity $(R_0L^2)/D_0$ controls the ratio of reaction to diffusion kinetics, while the quantity $E^a/(R\theta c_{\max}^R)$ controls the magnitude of the activation energy barrier.

We consider here two regimes for the formation of a sharp interface during a diffusion–reaction process. The first regime, termed "kinetically controlled", occurs when the diffusion–reaction problem is diffusion limited, that is when the *reaction kinetics are much faster than the diffusion kinetics*. This regime will naturally result in a sharp interface as there is no time for the diffusing species to transport beyond the reaction front and form a wide interface. This regime is most often used in the literature as the mechanism for producing a sharp interface (cf. Konica and Sain, 2020; Loeffel et al., 2013; Zhao et al., 2019a). Such a regime is shown in Fig. 5(a) where we set $E^a/(R\theta c_{max}^R) = 0$ and consider simulations with increasing values of $(R_0L^2)/D_0$. The first simulation with $(R_0L^2)/D_0 = 0.01$ does not form a sharp interface. As we increase this ratio and the kinetics of reaction becomes faster, we form a sharp interface. Past the value of $(R_0L^2)/D_0 = 1$ considered here, the width of the sharp interface remains constant and is determined by the λ parameter in (7.23) which is introduced for numerical regularization so as to maintain an interface of finite width. While this regime is physical in nature – that is some systems will have reaction kinetics which are faster than diffusion kinetics – not all problems of relevance which exhibit sharp interface reactions (including the one considered in Section 9.2) have reaction kinetics which are faster than diffusion.

We now consider the second regime, termed "thermodynamically controlled", which occurs when the activation energy introduced through ψ_R^ξ in (7.8) becomes significant. In such a regime, a sharp interface may form even when the reaction kinetics are sluggish and are the limiting process in the diffusion–reaction physics. In this regime a sharp interface is formed when the height of the potential barrier is significantly larger than the thermal energy. This regime is shown in Fig. 5(b) where we set $(R_0L^2)/D_0=0.01$ and consider simulations with increasing values of $E^a/(R\theta c_{\rm max}^R)$. The first simulation with $E^a/(R\theta c_{\rm max}^R)=0$ is identically equal to its counterpart in Fig. 5(a) above and as such does not produce a sharp interface. However now, as we increase $E^a/(R\theta c_{\rm max}^R)$ — while maintaining the kinetics fixed at a ratio which would not produce a sharp interface — we can see the formation of a sharp interface at $E^a/(R\theta c_{\rm max}^R)=20$. Again, above values of $E^a/(R\theta c_{\rm max}^R)=20$, the width of the interface is governed by the λ parameter in (7.23).

As discussed in Section 9.2, a large family of relevant solids undergoing sharp-interface reactions for applications in energy storage and conversion electrodes belong to the family in which the reaction kinetics are sluggish (cf. Boebinger et al., 2018; Zhang et al., 2015). In this class of reactions the sharp interface is governed by the height of the thermodynamic energy barrier as we have introduced in our theoretical framework. The developed theoretical framework fills this gap in the available continuum chemo-mechanics treatment of reaction-diffusion-deformation problems.

Finally, one additional crucial consideration is with regards to anisotropy. Some sharp interface reactions occur with an anisotropic reaction front (cf. Liu et al., 2011; Lee et al., 2012). The physics controlling that front may arise for example from anisotropies in the manner in which the reaction occurs, rather than anisotropies in the diffusivity of the species. If a sharp interface arises in the kinetically controlled regime anisotropies in the reaction rate will not impact the actual morphology of the interface since

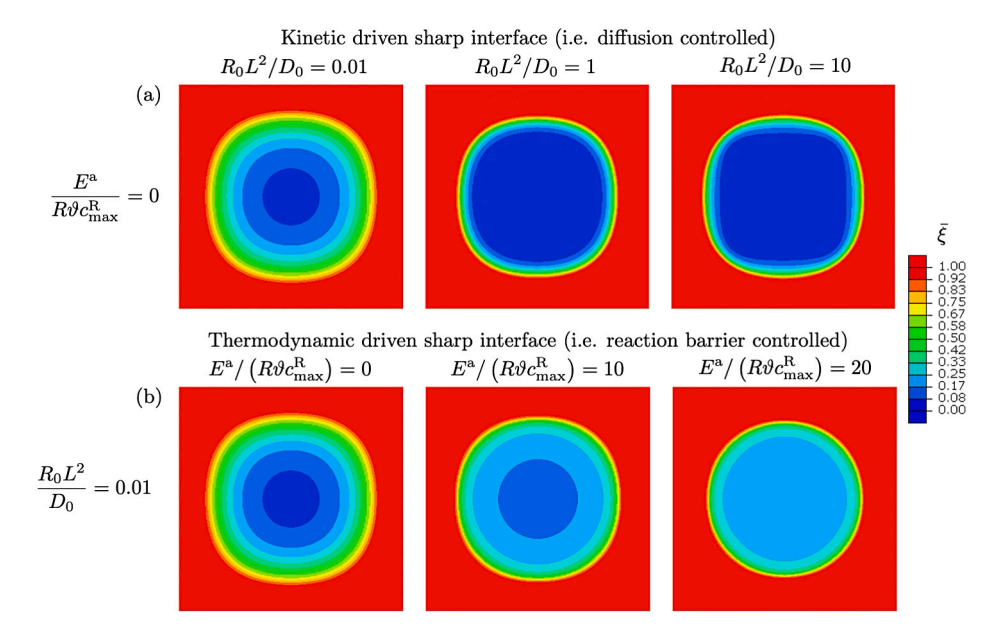


Fig. 5. Diffusion–reaction (no mechanics) sharp interface simulations in a two-dimensional domain. (a) Shows the formation of a sharp interface in the kinetically driven regime where the reaction rate is significantly faster than the diffusion kinetics. (b) Shows the formation of a sharp interface in the thermodynamically driven regime where the activation energy is much larger than the thermal energy.

diffusion is the limiting factor. On the other hand, if one wants to model an anisotropic reaction front that is thermodynamically driven, one cannot rely on anisotropy in diffusion kinetics as it is not the limiting factor in this regime. An anisotropic reaction front morphology arising from anisotropic reaction kinetics will be demonstrated in Section 9.2.

9.2. Modeling chemo-mechanics of sharp interface reactions in FeS2 conversion electrodes

In this Section we apply our theoretical framework to an engineering problem of relevance, namely the modeling of conversion electrode materials for next generation energy storage. In particular, we focus on the reaction of FeS₂ crystals with different ions as recently experimentally studied by Boebinger et al. (2018). Through this modeling we also highlight the role of mechanics in the chemo-mechanical modeling of these materials with a particular emphasis on how mechanics changes the morphology of the reaction interface. In turn, the morphology of the interface is critical for it largely dictates the manner in which stresses are generated and can subsequently lead to failure of the host material during the reaction process.

As shown in Fig. 6, Boebinger et al. (2018) observed that in the case of reaction of FeS_2 with the "small" Li ions (left figure) the morphology of the interface was particularly sharp (concave) and significant fracture occurred. In contrast, they observed that when reacting FeS_2 with the "large" Na ions (right figure), the morphology of the interface was smoother (convex) and significantly less fracture was observed in the electrode. This observation is significant since reaction of FeS_2 with Li leads to volume changes of approximately 180% whereas reaction with Na leads to changes of approximately 330%. One would thus expect mechanical failure to be more prevalent in the reaction with Na ions; however, the opposite was experimentally observed. Importantly, both reactions proceed through the formation and propagation of a sharp interface.

In order to model the diffusion–reaction–deformation behavior of these crystals we consider a three-dimensional (3D) cubic crystal measuring 40 nm in each side. We discretize one-eight of the crystal with a finite element mesh and appropriate symmetry boundary conditions. Fig. 7 shows the $20 \times 20 \times 20$ nm cube simulation domain which is discretized with 10 585 brick elements (approximately $20 \times 20 \times 20$ elements per side). The exterior edges of the crystal are slightly filleted to avoid numerical convergence issues at the early stages of the simulation when the reaction front first forms. We apply a constant flux and zero traction boundary conditions on the faces $\{A, B, C\}$ shown in Fig. 7, the remaining faces have symmetry boundary conditions. The magnitude of the applied flux was chosen to fill the simulation domain with $c = c_{\text{max}}^D + c_{\text{max}}^R$ moles of species in approximately one hour. The numerical value is given by $\mathbf{j}_R = 0.75 \cdot 10^{-6} \, \text{mol/m}^2/\text{s}^2$.

As discussed in the introduction, and detailed in Section 9.3, wetting (surface energy) boundary conditions are critical in obtaining experimentally relevant reaction morphologies. Here on faces $\{A, B, C\}$ we apply a constant surface energy by prescribing

$$\eta = \lambda \nabla \xi \cdot \mathbf{n}_{R} = 10 \text{ J} \mu \text{m/mol}$$
 (9.3)

as a boundary condition for the PDE governing the reaction kinetics (8.3). In the absence of experimental or ab-initio data yielding the precise value, here this value was chosen by trial and error to provide sufficient surface wetting to capture the experimentally observed reaction morphologies. The prescribed value corresponds to a surface energy of $\eta c_{\text{max}}^{R} = 0.8 \text{ J/m}^2$, which is in the order of magnitude expected for solid surface interfaces (cf. Cogswell and Bazant, 2013).

The reaction being modeled proceeds as follows

$$FeS_2 + 4M \rightarrow Fe + 2M_2S \tag{9.4}$$

where M is a placeholder for either Li or Na ions. It is worth noting here that we treat the whole network of iron and ion-sulfide on the right hand side as one product phase. In other words, subsequent phase separation of iron in the product phase is not modeled and is outside the scope of this work.

We make the following assumptions in further specializing the theory described in Section 7 to this particular problem. On the chemical expansions, we take all chemically induced deformations to be due to reaction, and neglect volume changes due to the

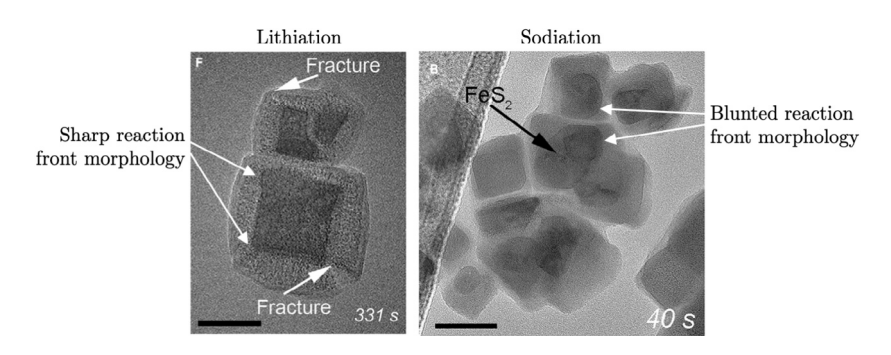


Fig. 6. Lithiation vs. sodiation of FeS₂ crystals. Although lithiation produces smaller overall reaction induced deformations, the morphology of the reaction front is significantly sharper and results in significant fracture. sodiation proceeds with a reaction front morphology which is blunter and significantly less fracture is observed.

Source: Reproduced and adapted with permission from Boebinger et al. (2018).

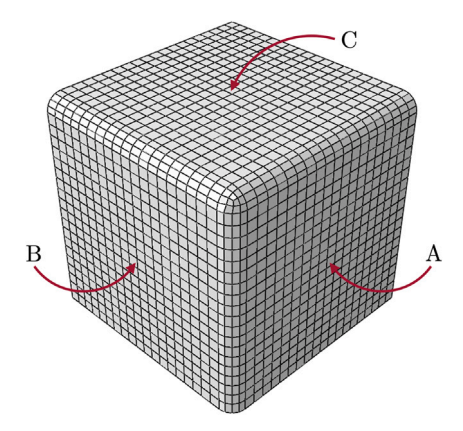


Fig. 7. Three-dimensional simulation domain for one-eighth of an FeS_2 nano particle. Constant flux, zero traction, and constant wetting boundary conditions are applied on the $\{A, B, C\}$ face shown. On the remaining three faces we apply symmetry boundary condition (i.e. no displacement in the perpendicular direction to the face, zero flux, and zero wetting).

diffusion, that is $\mathbf{D}^{\alpha,D} = \mathbf{D}^{\beta,D} = \mathbf{0}$. For the plastic behavior we employ a standard rate-independent elastic–plastic Mises flow rule as described in Section 7.6. The yield function is given as

$$Y = Y_0 + H\bar{\gamma}^p \tag{9.5}$$

with yield strength Y_0 and linear hardening coefficient H (for similar works using Mises theory in the context of energy storage chemo-mechanics, cf. Brassart and Suo, 2013; Hofmann et al., 2020, and Zhao et al., 2011a). The specific material properties are listed in Table 1, and we note the small amount of linear hardening introduced is used to ease numerical convergence.

The reaction–diffusion portion is identically equal to that presented in Section 7 with one modification to account for the anisotropic nature of the reaction. We introduce an anisotropy of the reaction rate motivated by the experimental observations of Boebinger et al. (2018). We implement this anisotropy by multiplying the reaction rate R_0 by the following factor

$$(1-3\delta)\left(1+\frac{4\delta}{1-3\delta}\left(n_x^4+n_y^4+n_z^4\right)\right) \tag{9.6}$$

where (n_x, n_y, n_z) are cosine directions normal to the reaction front, obtained from $\nabla \xi/|\nabla \xi|$. The parameter δ controls the strength of the anisotropy and we have calibrated this to 0.25 to reproduce the experimentally observed reaction fronts. The form of the anisotropy function in (9.6) is taken from Wang and Inatomi (2010) where it was employed for phase field modeling of anisotropic growth of crystals.

Material parameters are listed in Table 1. The chemical properties were determined as follows:

- The diffusivity of lithium ions in FeS₂ was reported in the experiment by Tao et al. (2016) and is presumed here to be the same for both reacted and unreacted phases. The same diffusivity is also used for sodium as its diffusivity was not readily available in the literature.
- The reaction rate R_0 is estimated from the experimental observations in Boebinger et al. (2018), by measuring the size of the internal FeS₂ crystal (unreacted phase) at different times.
- The energetic driving forces μ_0^{ξ} and μ_0^{α} are computed based on the energies of formation of the individual compounds with the assumption of zero energy of formation for the solid Fe and the diffusing species. This value is on the order -500 to -600 kJ/mol, orders of magnitude higher than the thermal energy which is 2.5 kJ/mol at room temperature.
- The maximum concentration of diffusing species is given by $c_{\max}^D = \phi \rho_{\text{FeS}_22} / \mathcal{M}_{\text{FeS}_22}$ with ρ_{FeS_22} the mass density of the host, $\mathcal{M}_{\text{FeS}_22}$ the molar mass of the host, and ϕ the number of sites available. We use here $\phi = 8$ due the cubic structure of the FeS₂ crystal.
- The maximum concentration of reacted species is given by $c_{\text{max}}^{\text{R}} = 2\rho_{\text{FeS}_22}/\mathcal{M}_{\text{FeS}_22}$, where the coefficient 2 is the stoichiometric amount of M in the reacted product in reaction (9.4).
- The experimental observations of Boebinger et al. (2018) on the observed volume changes yield that $\Omega_{\xi}^{\text{Li}} c_{\text{max}}^{\text{R}} = 1.8$ and $\Omega_{\xi}^{\text{Na}} c_{\text{max}}^{\text{R}} = 3.3$ which using the calibrated value for $c_{\text{max}}^{\text{R}}$ yield the partial molar volumes as $\Omega_{\xi}^{\text{Li}} = 22 \, \mu \text{m}^{33}/\text{mol}$ and $\Omega_{\xi}^{\text{Na}} = 40 \, \mu \text{m}^{33}/\text{mol}$.
- The energetic barrier $E^a = 4 \cdot 10^6 \, \text{kJ/m}^3$ is taken from the works of Wan et al. (2010) and Zhao et al. (2011b), where it was calculated for lithium insertion in Silicon using first principles. We use the same energetic barrier here for lithium and sodium in FeS₂ since the specific values were not readily available in the literature.
- The anisotropic factor δ in (9.6) is calibrated based on the experimental observations of Boebinger et al. (2018).

The above highlights an important feature of our theoretical framework which is that due to the thermodynamically consistent formulation, almost all parameters for the chemical portion of the theoretical framework discussed above *can be found experimentally*

 Table 1

 Material properties for the fully coupled reaction-diffusion-deformation theory.

	Parameter	Value	Source
Chemical	D_0	$2 \times 10^{-16} \text{ m}^2/\text{s}$	Tao et al. (2016)
	R_0	$10^{-3} \ 1/s$	Boebinger et al. (2018)
	μ_0^{lpha}	-167 KJ/mol	Chase Jr (1998)
	$\mu_0^{\xi}(\text{Li}_2S)$	-447 KJ/mol	Greenwood and Earnshaw (1997)
	$\mu_0^\xi(\mathrm{Na_2S})$	-370 KJ/mol	Raberg (2007)
	$c_{\mathrm{max}}^{\mathrm{D}} = 8 \rho_{\mathrm{FeS}_2} / \mathcal{M}_{\mathrm{FeS}_2}$	$0.32\cdot 10^6\ mol/m^3$	Set by crystal structure
	$c_{\mathrm{max}}^{\mathrm{R}} = 2 \rho_{\mathrm{FeS}2} / \mathcal{M}_{\mathrm{FeS}2}$	$0.08\cdot 10^6\ mol/m^3$	Set by stoichiometry
	$ ho_{\mathrm{FeS}_2}$	5.0 g/cm ³	PubChem Database (2005)
	\mathcal{M}_{FeS_2}	120 g/mol	PubChem Database (2005)
	$arOmega_{ar{arepsilon}}^{ m Li} c_{ m max}^{ m R}$	1.8	Boebinger et al. (2018)
	$arOmega_{arxi}^{ m Na} c_{ m max}^{ m R}$	3.3	Boebinger et al. (2018)
	$E^{\mathbf{a}}$	$4\cdot 10^6~\text{KJ/m}^3$	Wan et al. (2010)
	δ	3	Calibrated
Mechanical	E _{FeS} ,	30 GPa	Boebinger et al. (2018)
	$\mathrm{E_{FeS_2}^{reacted}}$	20 GPa	Boebinger et al. (2018)
	v_{FeS_2}	0.3	Boebinger et al. (2018)
	Y_0	1.5 GPa	Boebinger et al. (2018)
	H	1.0 GPa	
Numerical	λ	$10.0 \text{ nJ}\mu\text{m}^5/\text{mol}^2$	

or from ab-initio simulations (the only exception being the anisotropic reaction rates). That is, the theoretical framework may be calibrated in straightforward fashion and as such should prove useful in application to a number of engineering problems of relevance. Finally, we note that based on the material properties above, the non-dimensional parameter $(R_0L^2)/D_0$ is equal to 0.008 for a 40 nm length scale. As such, for this system the *sharp interface is predominantly thermodynamically driven*, and would not occur in the absence of the activation energy.

The **mechanical properties** were extracted predominantly from the work of Boebinger et al. (2018). The Elastic modulus reported there was measured using nano-indentation for both pristine and reacted phases of FeS₂ crystal. We chose here to use the average of the two reacted Young's modulus in simulation and assume a constant Poisson's ratio. Further, following their work, the yield stress is simply assumed to be 5% of Elastic modulus. The interfacial energy parameter λ in (7.23), which is introduced for numerical regularization, was chosen as $\lambda = 8.0 \text{ nJ}\mu\text{m}^5/\text{mol}^2$. This was determined through simulations to provide a minimum interface width of approximately 2 nm, which could then be discretized with sufficient finite elements so as to provide accurate numerical results with the computational resources available.

Fig. 8 shows isocontours of the reaction coordinate $\bar{\xi}$ over time in (a) the one-eight simulation domain, (b) mirrored about two planes (representing a view cutting through the center of the crystal), and (c) of the fully-mirrored domain. In Fig. 8(a), the undeformed exterior of the simulation domain is shown with a dashed line while the deformed exterior is shown with a solid line. We can observe the manner in which a sharp anisotropic reaction forms and evolves over time with the accompanying large reaction induced deformations. We note throughout the simulation the sharp, concave-like, lithiation morphology which is also observed in the corresponding lithiation experiments of Boebinger et al. (2018) shown in the left of Fig. 6.

More importantly we now wish to compare the difference between lithiation and sodiation using our theoretical framework and numerical implementation. We note that the only parameter of relevance that changes between these two simulations is the partial molar volume Ω_{ξ} which is almost twice as large for the case of sodiation over lithiation. The energy of formation μ_0^{ξ} is also slightly different for these two materials but this does not have major impact on the simulation results.

Fig. 9 compares the evolution of the reaction front between (a) lithiation and (b) sodiation. We can clearly observe that the morphology of the reaction front changes drastically. This change is due to the complex coupling between mechanical deformations/stress and reaction kinetics as captured through the reaction driving force \mathcal{F} in (7.23). Increasing the molar volume Ω_{ξ} not only increases the amount of reaction induced deformations, it also generates a different stress field and a different magnitude of stress-coupling with the reaction kinetics which acts to "blunt" the sharp corners of the reaction front.

The phenomena is further illustrated in Fig. 10(a–b) where we show a side view of the inside of the crystal and visualize isocontours of the reaction coordinate ξ for (a) lithiation and (b) sodiation. Note here we have chosen to compare simulation results with the reaction front at similar locations, rather than at a fixed time. Comparing (a) and (b) in Fig. 10, we can clearly observe that the theoretical framework – by varying only the partial molar volume Ω_{ξ} – reproduces the experimental observation of Boebinger et al. (2018) whereby FeS₂ reactions with Li lead to a sharp (concave-like) reaction front while reactions with Na lead to a blunt (convex-like) reaction front. The arrows in Fig. 10 show the good qualitative agreement between the simulation results and the TEM images of Boebinger et al. (2018), where we highlight that in addition to capturing the correct morphology of the reaction front, the simulations also capture the manner in which the external reacted surfaces change between lithiation and sodiation. We note

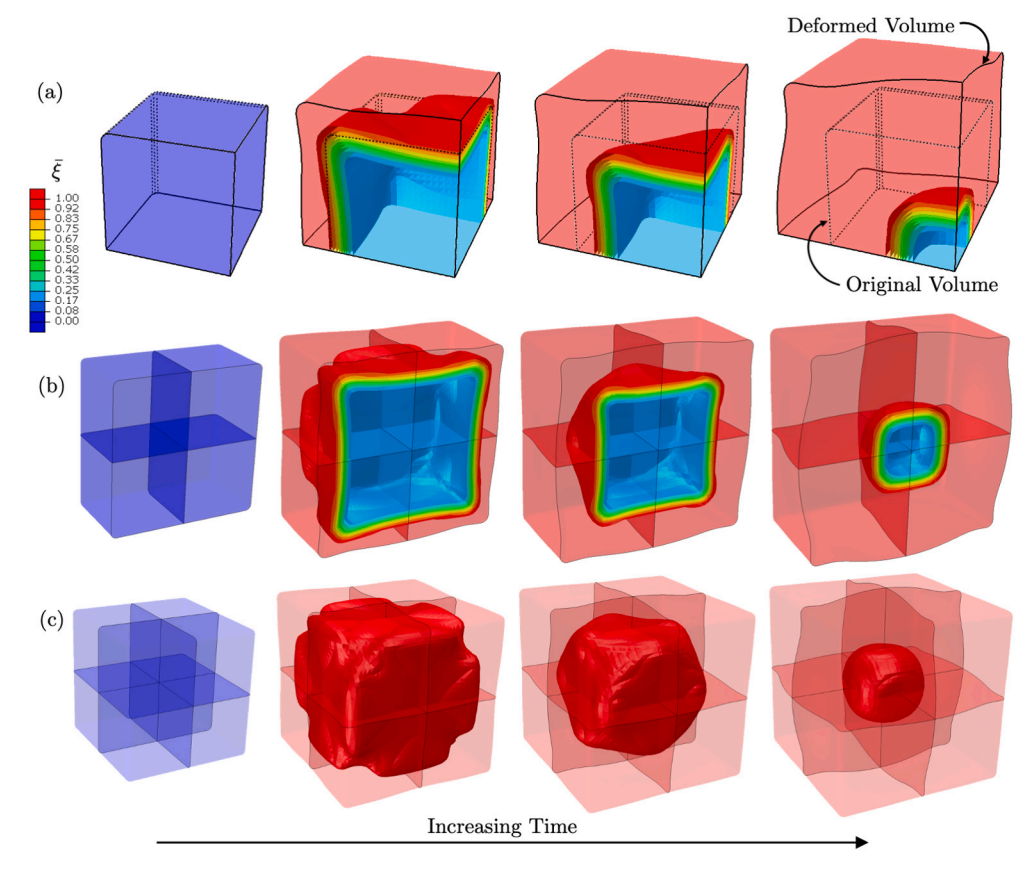


Fig. 8. Isocontours of reaction coordinate $\bar{\xi}$ with (a) showing the one-eight simulation domain, (b) mirrored about two planes, and (c) the fully-mirrored domain.

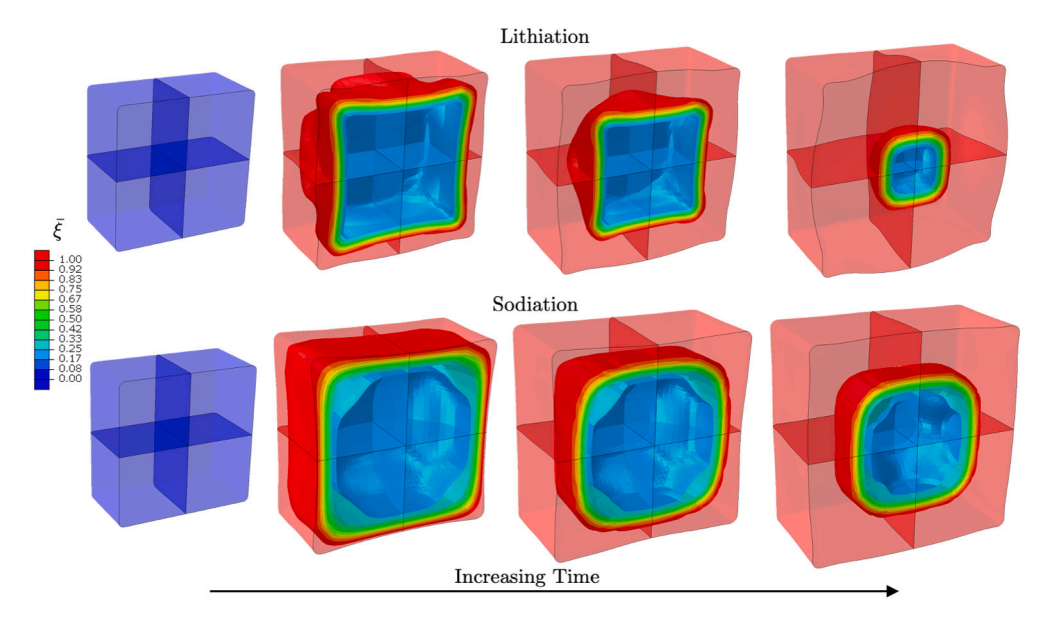


Fig. 9. Isocontours of reaction coordinate ξ with (a) showing the lithiation simulation and (b) showing the sodiation simulation.

once again that the only simulation parameter of relevance varied between these simulations is the partial molar volume Ω_{ξ} . The strength of the reaction anisotropy, as prescribed through (9.6), is the same for both simulations.

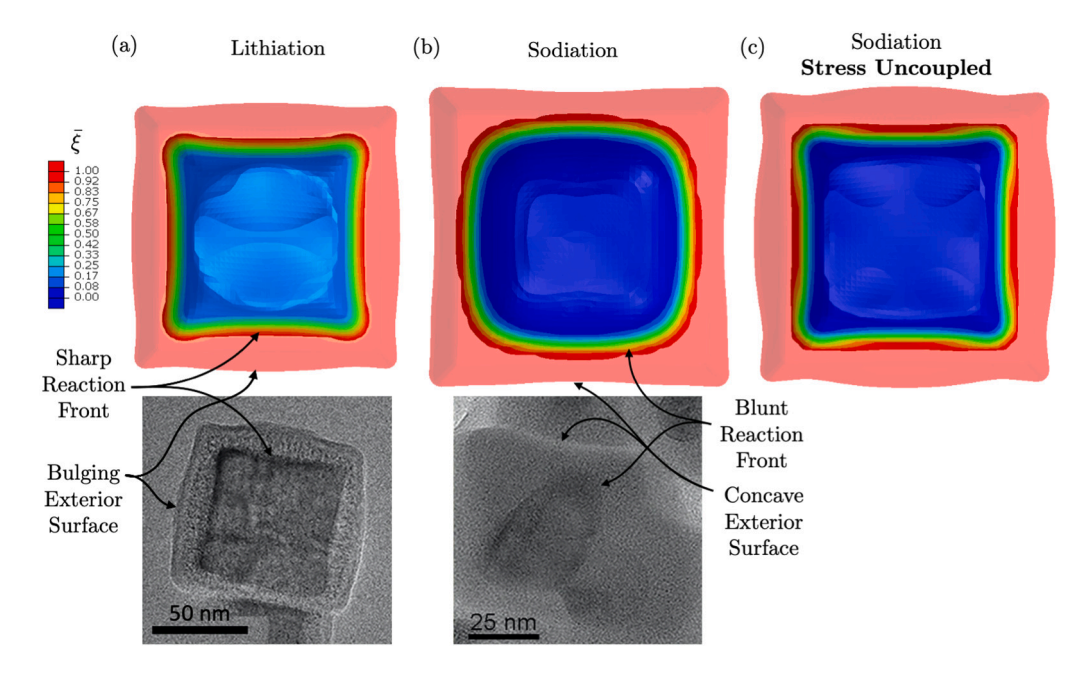


Fig. 10. Isocontours of reaction coordinate $\bar{\xi}$ in the inside of the crystal for (a) lithiation, (b) sodiation, and (c) sodiation without the effect of stress on the reaction driving force. Comparing (a–b) shows that although sodiation experiences larger volumetric expansions, the stress-coupling leads to a blunter reaction front. Comparing (b–c) shows that the effect of stress coupling drives the blunting of the reaction front in the sodiation simulations.

The blunting effect arises from the fact that the sodiation simulation with larger reaction induced deformations has significantly stronger coupling between mean tensile stresses and reaction rate at the corners of the simulation domain which in turn accelerates the reaction at those corners and leads to a blunter reaction front. The coupling arises from the stress effect in the reaction driving force \mathcal{F} given in (7.23). To illustrate the importance of this coupling, Fig. 10(b–c) compares two sodiation simulations with (b) the fully-coupled chemo-mechanical simulation, and (c) an uncoupled simulation. In Fig. 10(c) we have removed the stress effect term

$$J^{\rm c}\mathbf{M}^{\rm m}:\left((1-\bar{\xi})\mathbf{N}^{\alpha,D}+\bar{\xi}\mathbf{N}^{\beta,D}-\bar{\xi}\mathbf{N}^{\beta,R}\right)=\frac{1}{3}(\varOmega_{\xi}\bar{\xi}){\rm tr}\mathbf{M}^{\rm m}$$

from the reaction driving force \mathcal{F} in (7.23). As can be observed in Fig. 10(c), removing the stress effect on the reaction driving force leads to a return to sharp concave-like reaction front even for the case of sodiation. Further, note that the stress coupling arises not just from the stress field through the trM^m term above, but also through the magnitude of Ω_{ξ} which multiplies the stress. As such, the sodiation simulations need not produce significantly larger stresses, when compared to lithiation, to lead to blunting since they have larger Ω_{ξ} values. This confirms our observation that stress-coupling plays a critical role in determining the shape of the sharp interface reaction front.

Finally, it is important to note that our simulation framework demonstrates the possibility that mechanics plays a critical role in the development and evolution of the reaction front morphology in FeS₂ crystals. However, this does not exclude the possibility that the blunting of the reaction front observed experimentally during sodiation may arise from a number of combined mechanisms, including possible variations in material properties such as reactivity, activation energy, and yield stress between Li and Na in FeS₂. Further careful experimentation is necessary to definitively sort out the contributions from mechanics to those of chemistry in this class of problems. Nonetheless, the results shown here serve to demonstrate the capabilities of the general theoretical framework developed in this work and in particular the manner in which it may be calibrated and applied to an engineering problem of relevance in a straightforward fashion.

We finish this set of simulation results by briefly discussing the development of stresses and the potential for fracture. The theoretical formulation is fully-coupled in the sense that the stresses affect the reaction front morphology which in turn affects the distribution of stresses by altering the manner in which the reaction proceeds. To illustrate this, Fig. 11 shows contours of the *positive* principal stress $\{\sigma_1, \sigma_2, \sigma_3\}$ of the Cauchy stress for (a) lithiation and (b) sodiation along the (110) plane. The figures are taken at an instance where the reaction front has just formed, as stresses are largest during this time. This instance is highlighted by the insets in Fig. 11 which show isocontours of the reaction front along with a wireframe outline of the deformed body. Comparing Fig. 11(a) and (b) we can observe that the magnitude of the maximum principal stress σ_1 is larger in the lithiation simulations, here by approximately 10%, even though the overall reaction induced deformations are smaller in lithiation than sodiation. This is in good qualitative agreement with the experimental observations of Boebinger et al. (2018) who observed that fracture occurs more frequently in lithiation than in sodiation, even though this is intuitively not what one would expect as FeS₂ incurs much larger deformations during sodiation. Although stresses are larger in lithiation simulations, it must be noted that they are not drastically different and this suggest that further experimental investigations need to be performed to understand if there are also changes in the fracture toughness properties of the reacted materials which can help explain the experimental observations.

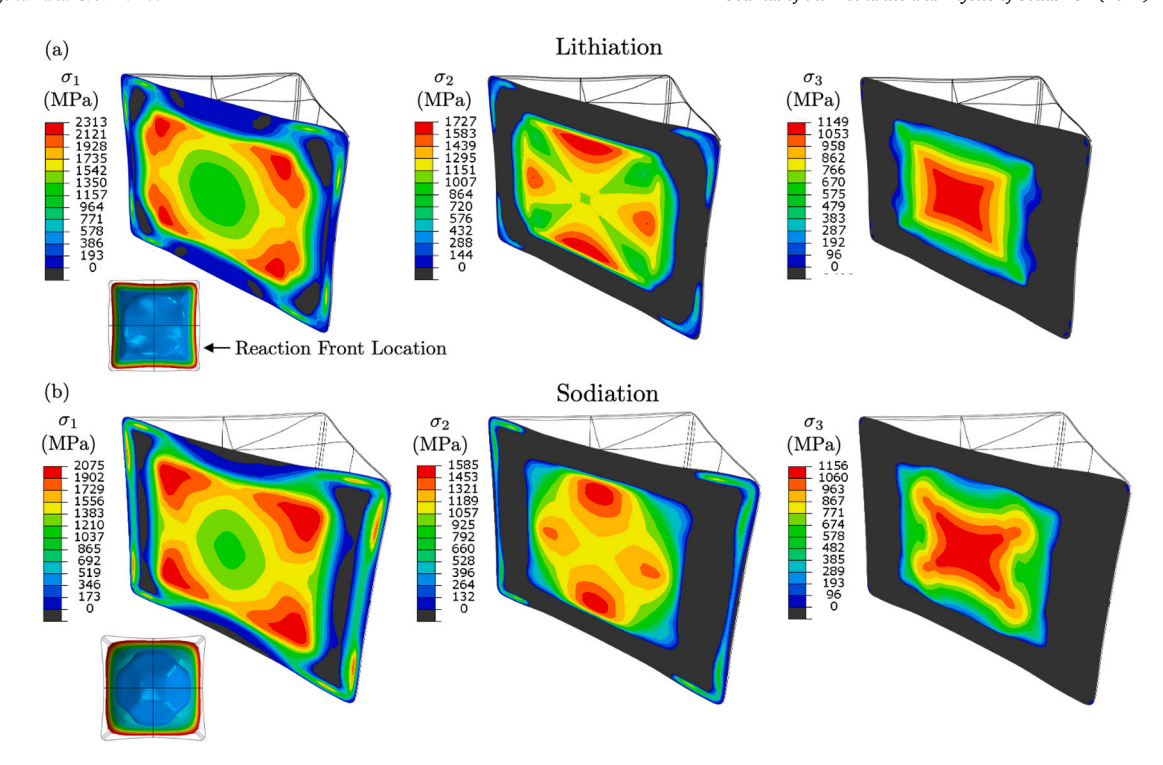


Fig. 11. Contours of positive principal stresses $\{\sigma_1, \sigma_2, \sigma_3\}$ during (a) lithiation and (b) sodiation. The inset shows isocontours of the reaction coordinate $\bar{\xi}$ along with a wireframe of the deformed body to highlight the location of the front within the solid at the times shown.

9.3. Sharp interface morphologies and the role of surface wetting boundary conditions

We present here a series of numerical examples to demonstrate the importance of the surface wetting (surface energy) boundary condition $(8.6)_2$ in reproducing experimentally relevant reaction front morphologies. All material parameters are identical to those listed in Section 9.2 with the only modification being to the $\eta = \lambda \nabla \xi \cdot \mathbf{n}_R$ boundary condition.

Fig. 12 shows isocontours of the reaction front for lithiation simulations with surface wetting ($\eta=10~\text{J}\mu\text{m}/\text{mol}$) in (a) against simulations with zero surface wetting ($\eta=0$) in (b) and (c). In Fig. 12(b) we show the wetting free simulations mirrored about two planes (representing a view cut through the center of the crystal), while (c) shows the fully-mirrored domain also for the wetting free case.

Comparing Fig. 12(a) and (b) we can clearly observe the importance of the wetting boundary condition. In Fig. 12(b-c), without any surface wetting, the morphology of the reaction front *does not form a core-shell structure*, as is expected and experimentally observed. The surfaces of the crystal do not become fully reacted early in the simulation, rather they remain partially reacted. From a numerical perspective, this can be expected from the nature of the boundary condition $(8.6)_2$ which dictates the value of $\nabla \xi \cdot \mathbf{n}_R$, which can also be thought of as the angle between the isocontours of ξ and the free surfaces. When $\eta = 0$, isocontours penetrating the free surfaces must be perpendicular to the free surface, that is $\nabla \xi$ and the unit normal to the free surface \mathbf{n}_R must be perpendicular. This in turn prevents these surfaces from becoming fully wetted. In contrast, as shown in Fig. 12(a), a non-zero value of the surface wetting boundary condition makes it favorable for the free surface to become fully reacted early in the simulation process, yielding the experimentally relevant core–shell structure. We emphasize that the only difference between the simulations shown in Fig. 12(a) and (b-c) is the wetting boundary condition, all other material properties and boundary conditions are identical.

The need for appropriate surface wetting boundary conditions is particularly important for chemo-mechanically coupled problems. This is demonstrated in Fig. 13, where we compare simulations with no mechanical deformation or coupling (left two columns, a–b and e–f) to fully-coupled chemo-mechanical simulations (right two columns, c–d and g–h). Simulations are shown at $t = 850 \,\mathrm{s}$ (top row, a–d) and $t = 950 \,\mathrm{s}$ (bottom row, e–h).

Focusing first on the mechanics free simulations, we can observe that for simulations without wetting, (a) and (e), the free surfaces will still become fully reacted at a relatively early stage such that by $t = 950 \, \mathrm{s}$ as shown in Fig. 13(e) the simulation has led to a core–shell morphology albeit with a somewhat distorted core structure. The addition of wetting does of course help improve the simulation even in the mechanics-free case as shown in (b) and (f). With wetting, we observe the formation of a core–shell structure early on in the simulation and the morphology of the reaction front in the core–shell structure remains a cube, retaining the original shape of the external surface. In contrast, when considering fully-coupled chemo-mechanical simulations as shown in the right two columns, (c–d, and g–h), the wetting boundary condition is critical in achieving a core–shell morphology. In chemo-mechanical simulations without wetting, Fig. 13(c) and (g) we do not observe the formation of a core–shell structure.

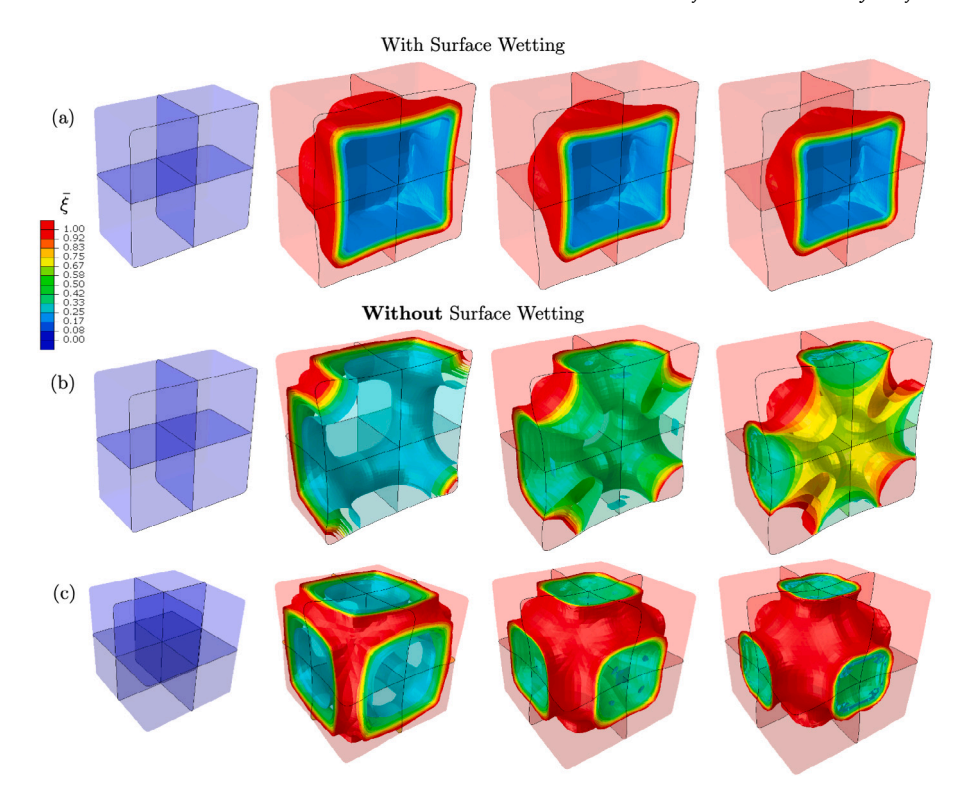


Fig. 12. Isocontours of reaction coordinate $\bar{\xi}$ for lithiation simulations with (a) surface wetting ($\eta = 10 \text{ J}\mu\text{m}/\text{mol}$), and (b-c) no surface wetting ($\eta = 0$). (a-b) show the simulation domains mirrored about two planes, while (c) shows the simulation domain fully mirrored.

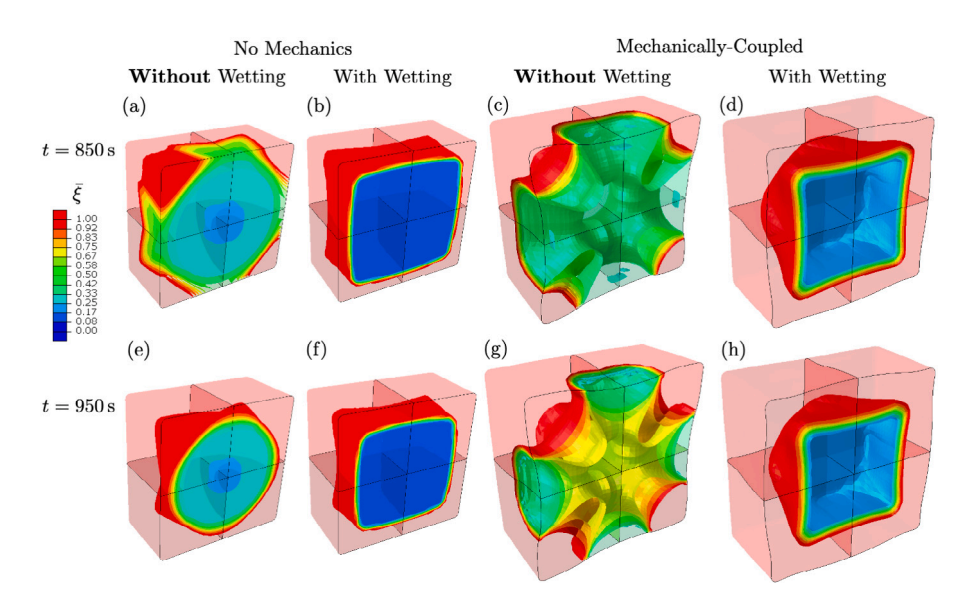


Fig. 13. Isocontours of reaction coordinate $\bar{\xi}$ for lithiation simulations. (a–b) and (e–f) show simulations with no mechanical deformation or stress coupling, while (c–d) and (g–h) show the fully-coupled chemo-mechanical simulations. We demonstrate the manner in which wetting boundary conditions are critical in fully-coupled simulations where a core–shell morphology is never achieved during simulation in the absence of these boundary conditions.

The role of the magnitude of η is briefly illustrated in Fig. 14 using fully-coupled two-dimensional simulations with (a) $\eta=0$, (b) $\eta=5$ Jµm/mol, and (c) $\eta=10$ Jµm/mol. For each particular simulation, we show isocontours of $\bar{\xi}$ when the free surfaces *first become* fully reacted. We can see two important effects of the magnitude of η . First, for the case of $\eta=0$ in Fig. 14(a), as also discussed above, we do not achieve a core–shell morphology, rather the reaction interface evolves significantly into the body until the reaction fronts meet at the free surfaces. In contrast, as η is increased to a non-zero value in Fig. 14(b–c), the free surfaces become fully reacted

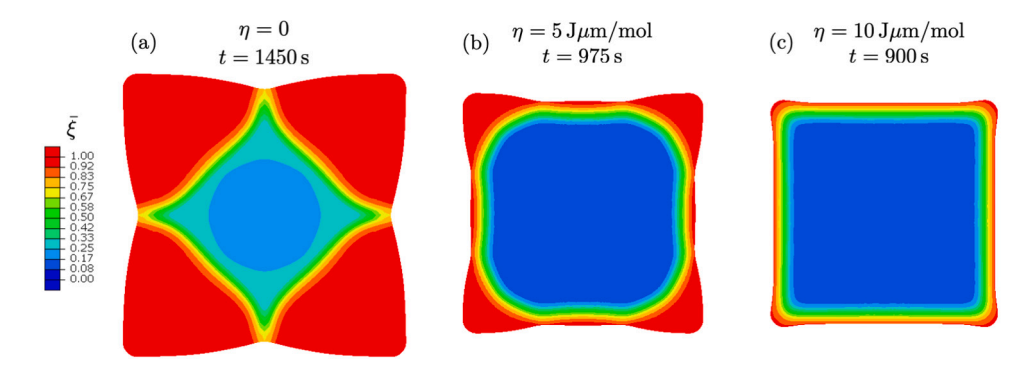


Fig. 14. Isocontours of reaction coordinate $\bar{\xi}$ for fully-coupled two-dimensional simulations with (a) $\eta = 0$, (b) $\eta = 5 \text{ J}\mu\text{m/mol}$, and (c) $\eta = 10 \text{ J}\mu\text{m/mol}$. For each case, results are shown at the instance when the free surfaces first become fully reacted. We can clearly observe the manner in which increasing surface wetting η leads to earlier wetting of the external surfaces and a well-defined and undistorted core–shell morphology.

early on in the simulation and the reaction front achieves a core–shell morphology. For an intermediate value of $\eta = 5 \,\mathrm{J}\mu\mathrm{m/mol}$ as shown in Fig. 14(b), full surface wetting still occurs only after the corners of the simulation domain are significantly reacted, leading to the distorted morphology shown. As η is increased to $10 \,\mathrm{J}\mu\mathrm{m/mol}$ and beyond, this distortion disappears and the free surfaces become fully wetted before reactions take place anywhere else on the body. The second important point is that increasing values of η also speed up the time at which the surfaces first become fully wetted. As shown in Fig. 14, as η increases full-wetting occurs earlier in time. These two-dimensional simulations were used to inform the choice of surface wetting boundary condition employed in the simulations shown in Section 9.2.

10. Concluding remarks

We have formulated a thermodynamically consistent field theory that couples diffusion of species, bulk sharp interface chemical reactions, and mechanical deformations. The framework was specialized to the engineering problem of relevance of modeling conversion electrodes for energy storage. In particular we demonstrated the manner in which material parameters may be calibrated in a straightforward fashion. The simulated results captured the experimental observations including the change in reaction front morphologies when reacting FeS₂ crystals with different ions.

Specific major contributions of this work include:

- The framework distinguishes between kinetically and thermodynamically driven sharp interface. Here kinetics encompasses the diffusion and reaction rates which may drive a sharp interface, while thermodynamics includes an activation energy capturing the reaction potential landscape which may also lead to the formation of a sharp interface.
- The thermodynamically consistent treatment enabled us to derive a physically motivated reaction driving force expression in which different contributions of energy, configurational entropy, mechanical stress, and activation energy can be readily identified. The formulation presented is general, and may be specialized to recover similar forms as in the existing literature but can also encompass other physical considerations. The continuum field treatment of the driving force also resulted in the existence of a critical concentration, below which the reaction would not initiate. Particularly useful then is the fact that material properties driving the reaction kinetics can be calibrated from the literature or experiments.
- The gradient based phase-field formulation is able to capture wetting (surface energy) boundary conditions which we demonstrated are critical to reproducing experimentally meaningful reaction morphologies, especially in the context of conversion materials for energy storage. Consequences of applying this surface energy as a boundary condition and its role in determining the reaction front morphology were elucidated using numerical simulations.

The theory was implemented in a three-dimensional finite element model and applied to modeling chemical reactions in a potential conversion electrode for energy storage. The role of mechanics in controlling the reaction morphology and subsequent stress distribution was demonstrated, and showcased the critical role mechanics can play in the behavior of these materials. The simulations captured the morphology of the chemical reaction front with good qualitative agreement as observed experimentally through TEM imaging.

CRediT authorship contribution statement

Arman Afshar: Design and implementation of the research, Analysis of results, Writing of the manuscript. **Claudio V. Di Leo:** Design and implementation of the research, Analysis of results, Writing of the manuscript.

Declaration of competing interest

The authors declare that they have no known competing financial interests or personal relationships that could have appeared to influence the work reported in this paper.

Acknowledgment

This work was supported by the National Science Foundation, USA under Award No. CMMI-1825132.

Appendix A. Formulation based on a decomposition of the diffusing species in the absence of mechanics

In this Appendix we present a brief formulation of a general reaction—diffusion theoretical framework with decomposition of the diffusing species into multiple species. The framework is then specialized *specifically* with the intent to find the special forms of the constitutive equations and the *limiting conditions* under which the theoretical framework developed in Sections 2 through 6 may be motivated as a particular case of the two-species diffusion theory. Specifically, we will demonstrate how the theoretical framework presented in the main body can be considered as a *limiting case* of this more general framework under conditions of equilibrium diffusion and uniform distribution of concentration within the material point in which the chemical reaction is occurring. We note that the specialized constitutive forms are chosen solely for the purpose of comparing to the main body formulation and not as a derivation of a stand-alone two-species diffusion formulation. For brevity, we present only the chemical reaction—diffusion phenomena, in the absence of mechanical coupling and in the absence of gradients in the reaction coordinate.

A.1. Mass conservation

Consider the schematic Fig. 15 of a part P over which we have ongoing diffusion and the generic reaction $A+C\to B$. Regions labeled as α represent unreacted phases of the part, while regions labeled β represent reacted phases. We now consider two diffusing species, distinguishing between the presence of the species in either α or β phases. Let $c_{\alpha}(\mathbf{X},t)$ denote the number of moles of diffusing species in the α phase per unit volume, and $c_{\beta}(\mathbf{X},t)$ the number of moles of diffusing species in the β phase per unit volume.⁵ As in Section 2, we let ξ denote the number of moles of reacted species, with $\dot{\xi}$ the reaction rate. We define $\bar{\xi}=\xi/c_{\max}^{\xi}$ as the extent of reaction. We introduce here a new quantity, $R_{\alpha\beta}$, which denotes the transfer rate of diffusing species between the α and β phases. Physically, this is the diffusion of species across the interface between reacted and unreacted portions of the material.

Mass conservation may now be written as two diffusion-reaction equations of the form

$$\dot{c}_{\alpha} = -\text{Div}\,\mathbf{j}_{\alpha} - R_{\alpha\beta} - \dot{\xi},\tag{A.1}$$

$$\dot{c}_{\beta} = -\text{Div}\,\mathbf{j}_{\beta} + R_{\alpha\beta},\tag{A.2}$$

with \mathbf{j}_{α} the flux of species into α phases, and \mathbf{j}_{β} the flux of species into β phases. Consistent with the schematic in Fig. 15, chemical reactions leading to the formation of new β phase occur between the diffusing species in the unreacted α and the host phase itself, hence inclusion of the reaction rate $\dot{\xi}$ only in (A.1).

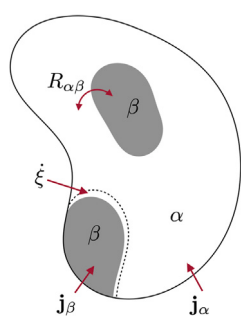


Fig. 15. Schematic of a part P with unreacted portions denoted by α and reacted portions denoted by β . $R_{\alpha\beta}$ denotes diffusion across the α - β interfaces, $\dot{\xi}$ characterizes the growth of a β phase due to chemical reaction, and \mathbf{j}_{α} are the fluxes of species into the α and β phases respectively.

⁵ Note that in this development, consistent with our neglect of mechanical coupling and mechanical deformations, we no longer distinguish between undeformed and deformed quantities and everything may be viewed as defined over a stationary undeforming reference configuration.

Summing (A.1) and (A.2) yields the same conservation Eq. (2.2) from Section 2 of the form

$$\dot{c} = -\text{Div}\,\mathbf{j} - \dot{\xi} \tag{A.3}$$

where in writing (A.3) we have defined

$$c \stackrel{\text{def}}{=} c_{\alpha} + c_{\beta}$$
, and $\mathbf{j} \stackrel{\text{def}}{=} \mathbf{j}_{\alpha} + \mathbf{j}_{\beta}$, (A.4)

as the total concentration of diffusing species c, and the total flux \mathbf{j} . With this decomposition of the diffusing species into unique identifiers, we now develop the remainder of the formulation based on continuum thermodynamics.

A.2. Free-energy imbalance

Under isothermal conditions, and considering here a formulation without mechanical work, the free energy imbalance may be written as

$$\int_{\mathbf{P}} \psi dv \le -\int_{\partial \mathbf{P}} \mu_{\alpha} \mathbf{j}_{\alpha} \cdot \mathbf{n} da - \int_{\partial \mathbf{P}} \mu_{\beta} \mathbf{j}_{\beta} \cdot \mathbf{n} da, \tag{A.5}$$

which using the divergence theorem over the boundary integral terms, and using the fact that this must hold for all parts P, yields the local free energy imbalance as

$$\dot{\psi} + \mu_{\alpha} \text{Div} \mathbf{j}_{\alpha} + \mathbf{j}_{\alpha} \cdot \nabla \mu_{\alpha} + \mu_{\beta} \text{Div} \mathbf{j}_{\beta} + \mathbf{j}_{\beta} \cdot \nabla \mu_{\beta} \le 0. \tag{A.6}$$

Using the mass balance Eqs. (A.1) and (A.2) this may be written as

$$\dot{\psi} - \mu_{\alpha}(\dot{c}_{\alpha} + \dot{\xi}) - \mu_{\beta}\dot{c}_{\beta} + R_{\alpha\beta}(\mu_{\beta} - \mu_{\alpha}) + \mathbf{j}_{\alpha} \cdot \nabla \mu_{\alpha} + \mathbf{j}_{\beta} \cdot \nabla \mu_{\beta} \le 0. \tag{A.7}$$

A.3. Constitutive equations

A.3.1. Energetic constitutive equations

We consider a constitutive equation for the free energy ψ of the form

$$\psi = \hat{\psi}(c_{\alpha}, c_{\beta}, \xi). \tag{A.8}$$

Substituting (A.8) into (A.7) the free energy imbalance may be written as

$$\left(\frac{\partial \psi}{\partial c_{\alpha}} - \mu_{\alpha}\right) \dot{c}_{\alpha} + \left(\frac{\partial \psi}{\partial c_{\beta}} - \mu_{\beta}\right) \dot{c}_{\beta} + \left(\frac{\partial \psi}{\partial \xi} - \mu_{\alpha}\right) \dot{\xi} + R_{\alpha\beta}(\mu_{\beta} - \mu_{\alpha}) + \mathbf{j}_{\alpha} \cdot \nabla \mu_{\alpha} + \mathbf{j}_{\beta} \cdot \nabla \mu_{\beta} \le 0. \tag{A.9}$$

As in Section 5.1 following (5.3), here too we assume that processes associated with diffusion (governed by \dot{c}_{α} and \dot{c}_{β}) are energetic, while processes associated with the chemical reaction (governed by $\dot{\xi}$) are dissipative. We further assume here that the process of diffusing across an $\alpha - \beta$ interface governed by $R_{\alpha\beta}$ is dissipative, which will be further clarified subsequently.

As the inequality in (A.9) is to hold for all values of \dot{c}_{α} and \dot{c}_{β} , the "coefficients" must vanish and we are led to the thermodynamic restriction that the free energy determine the chemical potentials through the "state relations":

$$\mu_{\alpha} = \frac{\partial \psi}{\partial c_{\alpha}},$$

$$\mu_{\beta} = \frac{\partial \psi}{\partial c_{\beta}}.$$
(A.10)

We are now left with a reduced dissipation inequality of the form

$$\mathcal{D} = -\left(\frac{\partial \psi}{\partial \xi} - \mu_{\alpha}\right)\dot{\xi} - R_{\alpha\beta}(\mu_{\beta} - \mu_{\alpha}) - \mathbf{j}_{\alpha} \cdot \nabla \mu_{\alpha} - \mathbf{j}_{\beta} \cdot \nabla \mu_{\beta} \le 0. \tag{A.11}$$

A.3.2. Dissipative constitutive equations

As in Section 5.2, we define the chemical potential of the species of interest in the reacted compound as

$$\mu^{\xi} \stackrel{\text{def}}{=} \frac{\partial \psi}{\partial \xi} \tag{A.12}$$

and define the thermodynamic force driving the chemical reaction as

$$\mathcal{F} \stackrel{\text{def}}{=} u^{\xi} - u_{\alpha} \tag{A.13}$$

and the dissipation inequality (A.11) may now be written as

$$\mathcal{D} = -\mathcal{F}\dot{\xi} - R_{\alpha\beta}(\mu_{\beta} - \mu_{\alpha}) - \mathbf{j}_{\alpha} \cdot \nabla \mu_{\alpha} - \mathbf{j}_{\beta} \cdot \nabla \mu_{\beta} \le 0. \tag{A.14}$$

Remark 7. The dissipation inequality (A.14) has important similarities and differences with the inequality (5.8) in Section 5.2.

First, in this development, the driving force \mathcal{F} depends on the difference of μ^{ξ} and μ_{α} , rather than on a single chemical potential μ as in the main body of this work. This difference arises naturally from the fact that here we distinguish between the chemical potentials of the diffusing species in either the unreacted or reacted phases.

Second, the dissipation inequality (A.14) has an additional driving force $(\mu_{\beta} - \mu_{\alpha})$ which drives the diffusion of species across the $\alpha - \beta$ interface. As expected, this process also depends on a jump in chemical potential. It is similar to the manner in which bulk diffusion will depend on gradients in chemical potential, but now at an interface, where the transformation $R_{\alpha\beta}$ will depend on the jump in chemical potential. \square

A.4. Equilibrium diffusion between α and β phases

We now make the specific assumption that the process of diffusion of species across the $\alpha - \beta$ interface is an equilibrium process. Thus, whenever such phases exists in the body (i.e. whenever $0 < \bar{\xi} < 1$) we constrain ourselves to

$$\mu_{\alpha} = \mu_{\beta} \tag{A.15}$$

which effectively states that these species are in chemical equilibrium within the material point. Another way of viewing this constraint is by stating that the diffusion process across the $\alpha-\beta$ phase is much faster than other processes. In essence, following the dissipation inequality (A.14), we expect the diffusion rate $R_{\alpha\beta}$ to be a function of the driving force ($\mu_{\beta}-\mu_{\alpha}$) and to drive this driving force to zero as the process reaches equilibrium. If $R_{\alpha\beta}$ is sufficiently fast, the two potentials μ_{α} and μ_{β} will always be in equilibrium such that this driving force is essentially always zero.

In view of the restriction (A.15), the chemical potentials (A.26) are no longer independent. Further, we define a chemical potential μ of the form

$$\mu \stackrel{\text{def}}{=} \frac{\mu_{\alpha} + \mu_{\beta}}{2}.\tag{A.16}$$

which we note also implies that $\mu = \mu_{\alpha} = \mu_{\beta}$ through the constraint (A.15). Focusing first on the dissipation inequality, use of (A.15) in (A.14) along with the fact that $\mathbf{j} = \mathbf{j}_{\alpha} + \mathbf{j}_{\beta}$ from (A.4)₂ yields the following dissipation inequality

$$D = -F\dot{\xi} - \mathbf{j} \cdot \nabla \mu \le 0, \tag{A.17}$$

which in the absence of mechanical contributions, **is identical in form** to (5.8) in Section 5.2 of the main body. Here we may now prescribe a constitutive equation for the total flux **j** as a function of $\nabla \mu$ in identical nature to (6.9).

The theoretical framework as presented in Sections A.1 through A.4 is a complete framework and may be solved through finite element analysis if desired once the free energy (A.8) is specified. For completeness the governing partial differential equation would take the form

$$\dot{c} = \text{Div}(m\nabla u) - \dot{\xi} \tag{A.18}$$

with $\dot{c} = \dot{c}_{\alpha} + \dot{c}_{\beta}$ and where we have introduced $\mathbf{j} = -m\nabla\mu$ with m a mobility. The concentration c_{β} (or alternatively c_{α} as this is arbitrary) is now a dependent variable solved in any increment through the constraint $\mu_{\alpha} = \mu_{\beta}$ from (A.15). Finally, considering linear reaction kinetics, the reaction rate $\dot{\xi}$ would be solved using

$$\dot{\xi} = \begin{cases} -R_0 \mathcal{F}, & \text{if } \bar{\xi} < 0, \\ 0, & \text{if } \bar{\xi} = 1, \end{cases}$$
(A.19)

with $R_0 > 0$ a reaction rate constant, and \mathcal{F} given in (A.13).

The two-species diffusion–reaction formulation presented thus far is quite general. In the following Section we specialize this treatment solely with the intent to compare to the main body theory and finding the limiting conditions under which the main body theoretical framework may be derived as a limiting case.

A.5. Specialization of the constitutive equations. Comparison to the main body theory

We now specialize the form of the free energy function ψ with an objective of developing the chemical potentials μ_{α} and μ_{β} and the driving force \mathcal{F} and comparing to our formulation in the main body of this work.

Similar to (7.6) in Section 7.2, we take the free energy to be separable and of the form

$$\hat{\psi}(c_a, c_\beta, \xi) = \psi^c(c_a, c_\beta, \xi) + \psi^{\xi}(\xi). \tag{A.20}$$

Here

(i) ψ^c is the change in the chemical free energy due to the mixing of the diffusing species. As in the main body, it is taken to be a weighted average over the reacted and unreacted phases, with the contribution of each phase assumed to be given by a

regular solution model. Specifically

$$\begin{split} \psi^{c}(c_{\alpha},c_{\beta},\xi) &= (1-\bar{\xi})\psi^{c,\alpha}(c_{\alpha}) + \bar{\xi}\psi^{c,\beta}(c_{\beta}) \\ &= (1-\bar{\xi})c_{\max}^{\alpha} \left(\mu_{0}^{\alpha}\bar{c}_{\alpha} + R\vartheta\left(\bar{c}_{\alpha}\ln\bar{c}_{\alpha} + (1-\bar{c}_{\alpha})\ln(1-\bar{c}_{\alpha})\right)\right) \\ &+ \bar{\xi}c_{\max}^{\beta} \left(\mu_{0}^{\beta}\bar{c}_{\beta} + R\vartheta\left(\bar{c}_{\beta}\ln\bar{c}_{\beta} + (1-\bar{c}_{\beta})\ln(1-\bar{c}_{\beta})\right)\right). \end{split} \tag{A.21}$$

where \bar{c}_{α} and \bar{c}_{β} are the normalized species concentrations (which will be defined shortly), c_{\max}^{α} and c_{\max}^{β} are the maximum molar concentration, and μ_0^{α} and μ_0^{β} are the reference potentials, all respectively in the unreacted α and reacted β phases.

(ii) ψ^{ξ} is the free energy of the diffusing species in the reacted compound and serves to introduce the reference potential for this species, it is identical to (7.8) in the absence of the energy barrier term. Here we could also include the activation energy as included in (7.8) but we neglect this term since it is not relevant to our discussion.

The energy is given as

$$\psi^{\xi}(\xi) = \xi \mu_0^{\xi}. \tag{A.22}$$

Using (A.21) and (A.22) the total free energy is given by

$$\begin{split} \psi_{\mathrm{R}}^{c}(c,\xi) &= (1-\bar{\xi})\psi^{c,\alpha}(c_{\alpha}) + \bar{\xi}\psi^{c,\beta}(c_{\beta}) \\ &= (1-\bar{\xi})\,c_{\mathrm{max}}^{\alpha} \left(\mu_{0}^{\alpha}\bar{c}_{\alpha} + R\vartheta\Big(\bar{c}_{\alpha}\ln\bar{c}_{\alpha} + (1-\bar{c}_{\alpha})\ln(1-\bar{c}_{\alpha})\Big)\right) \\ &+ \bar{\xi}\,c_{\mathrm{max}}^{\beta} \left(\mu_{0}^{\beta}\bar{c}_{\beta} + R\vartheta\Big(\bar{c}_{\beta}\ln\bar{c}_{\beta} + (1-\bar{c}_{\beta})\ln(1-\bar{c}_{\beta})\Big)\right) + \xi\mu_{0}^{\xi}. \end{split} \tag{A.23}$$

We now consider the *specific conditions* under which the chemical free energy $\psi^c(c_\alpha, c_\beta \xi)$ in (A.21) will be identical to $\psi^c_R(c, \xi)$ in the main body (7.7) in Section 7.2. The two energies are identical if the following conditions are met

$$\bar{c} = \bar{c}_{\alpha} = \bar{c}_{\beta}$$
, and $c_{\text{max}}^{\text{D}} = c_{\text{max}}^{\alpha} = c_{\text{max}}^{\beta}$. (A.24)

This motivates our statement in the main body — Remark 3 following (7.7) — that rationalizes our model as assuming a uniform distribution of diffusing species within the material point.

Under the specific condition (A.24) the two energies are identical, and we will demonstrate the chemical potential and reaction driving forces are also identical. The constraints (A.24) have a number of consequences which we elaborate on next. First, using $c = c_{\alpha} + c_{\beta}$ from (A.4)₁, the constraints (A.24) dictate that the normalized concentrations \bar{c}_{α} and \bar{c}_{β} must be defined as

$$\bar{c}_{\alpha} \stackrel{\text{def}}{=} 2 \frac{c_{\alpha}}{c_{\text{max}}^{\alpha}}, \quad \text{and} \quad \bar{c}_{\beta} \stackrel{\text{def}}{=} 2 \frac{c_{\beta}}{c_{\text{max}}^{\beta}}.$$
 (A.25)

We next derive the chemical potentials and reaction driving forces and compare with the main body of the theory.

A.5.1. Chemical potential

Using (A.23) in (A.10) the chemical potentials are given by

$$\mu_{\alpha} = 2(1 - \bar{\xi}) \left(\mu_{0}^{\alpha} + R\vartheta \ln \left(\frac{\bar{c}_{\alpha}}{1 - \bar{c}_{\alpha}} \right) \right),$$

$$\mu_{\beta} = 2\bar{\xi} \left(\mu_{0}^{\beta} + R\vartheta \ln \left(\frac{\bar{c}_{\beta}}{1 - \bar{c}_{\beta}} \right) \right).$$
(A.26)

In view of the definition for μ from (A.16) and under the constraints (A.24) we may write

$$\mu = \left(1 - \bar{\xi}\right)\mu_0^{\alpha} + \bar{\xi}\mu_0^{\beta} + R\vartheta\ln\left(\frac{\bar{c}}{1 - \bar{c}}\right),\tag{A.27}$$

which is **identical** in **form** to the chemical potential (7.16) in Section 7.4 of the main body of this paper, of course here in the absence of mechanical coupling.

A.5.2. Reaction driving force

Using (A.23) in (A.12), the chemical potential for the species of interest in the reacted compound is given by

$$\mu^{\xi} = \mu_0^{\xi} + \frac{2}{c_{\max}^{\xi}} \left(\mu_0^{\theta} c_{\theta} - \mu_0^{\alpha} c_{\alpha} \right) + \frac{2}{c_{\max}^{\xi}} \left(c_{\max}^{\theta} \hat{g}(\bar{c}_{\theta}) - c_{\max}^{\alpha} \hat{g}(\bar{c}_{\alpha}) \right), \tag{A.28}$$

where for brevity we have defined the function

$$\hat{g}(\bar{c}) = \bar{c} \ln \bar{c} + (1 - \bar{c}) \ln(1 - \bar{c}). \tag{A.29}$$

Considering the equilibrium of chemical potentials (A.15) and the definition of μ in (A.16), we may write that $\mu_{\alpha} = \mu$ and hence the thermodynamic driving force (A.13) for reaction may be expressed as $\mathcal{F} = \mu^{\xi} - \mu$. Then, under the constraints (A.24), and using μ^{ξ} from (A.28) and μ from (A.27) we may write \mathcal{F} as

$$\mathcal{F} = \mu^{\xi} - \mu = \mu_0^{\xi} + \frac{2}{c_{\max}^{\xi}} \left(\mu_0^{\theta} \frac{c}{2} - \mu_0^{\alpha} \frac{c}{2} \right) - \left(1 - \bar{\xi} \right) \mu_0^{\alpha} - \bar{\xi} \mu_0^{\theta} - R \vartheta \ln \left(\frac{\bar{c}}{1 - \bar{c}} \right),$$
(A.30)

which after rearranging may be written in the following useful form

$$F = \mu^{\xi} - \mu$$

$$= \underbrace{\frac{1}{c_{\text{max}}^{\xi}} \left(c - \xi \right) \left(\mu_0^{\beta} - \mu_0^{\alpha} \right) + \left(\mu_0^{\xi} - \mu_0^{\alpha} \right)}_{\text{entropic}} - \underbrace{R\vartheta \ln \left(\frac{\bar{c}}{1 - \bar{c}} \right)}_{\text{entropic}}$$
(A.31)

which is **identical in form** to the thermodynamic driving force (7.23) in Section 7.5 of the main body of this work with $c_{\max}^R = c_{\max}^{\xi}$. Of course here $\mathcal F$ is not mechanically coupled and does not contain either the activation barrier or numerical regularization terms which were also omitted.

As such, we can concisely describe the main body of this work as a limiting case of the more general two-species diffusion–reaction under two particular conditions, namely:

- The diffusing species in the unreacted α and reacted β phases are in equilibrium, such that their chemical potentials are equal at all times, that is $\mu_{\alpha} = \mu_{\beta}$. Note that this does not imply that their reference potentials, μ_{0}^{α} and μ_{0}^{β} are equal, for they may still differ
- The concentration within the material point is considered uniformly distributed such that $\bar{c}_{\alpha} = \bar{c}_{\beta} = \bar{c}$, and the maximum molar concentration of diffusing species allowed in each phase are identical such that $c_{\max}^{\alpha} = c_{\max}^{\beta} = c_{\max}^{D}$.

This analysis helps make clear what the underlying limiting conditions of the theory derived in the main body are. If a particular system is modeled in which it is desirable to relax these constraints, the two-species formulation provided in this appendix provides an avenue for the development of a more complex two-species theoretical framework as necessary.

Appendix B. Numerical implementation. Micromorphic approach

The theory has been implement in the finite element software Abaqus/Standard (Simulia, 2010) by writing a user-element subroutine (UEL), which couples mechanical deformation, ion diffusion and chemical reactions. The system of PDEs summarized in Section 8, however, can cause significant convergence issues. To alleviate the difficulty associated with the numerics, we utilized a split micromorphic implementation (cf. Forest, 2009; Di Leo et al., 2014) in which the gradient term $\nabla \xi$ in (8.3) is substituted with a micromorphic counterpart $\nabla \xi$ ^m. We note that this method, for appropriate numerical values as discussed below, will yield **identical** results to those that would be achieved if we had directly implemented the original PDEs shown in Section 8.

The micromorphic derivation is achieved by modifying the free energy (7.6) by introducing an additional penalty term, as following:

$$\check{\psi}_{R}(\mathcal{I}_{\mathbf{E}^{e}}, c, \xi, |\nabla \xi|) = \psi_{R}^{c}(c, \xi) + \psi_{R}^{\xi}(\xi) + \psi_{R}^{m}(\mathcal{I}_{\mathbf{E}^{e}}, c, \xi) + \psi_{R}^{g}(|\nabla \xi^{m}|) + \psi_{R}^{\text{micromorph}}(\xi, \xi^{m}), \tag{B.1}$$

where we note that the gradient energy ψ_R^g is now in terms of $\nabla \xi^m$ and we have introduced a penalty energy $\psi_R^{\text{micromorph}}(\xi,\xi^m)$ of the form

$$\psi_{\mathbf{R}}^{\text{micromorph}}(\xi, \xi^{\mathbf{m}}) = \frac{1}{2} \gamma(\xi - \xi^{\mathbf{m}})^2, \tag{B.2}$$

with a γ a simulation parameter which penalizes the difference between the real ξ and its micromorphic counterpart $\xi^{\rm m}$. For sufficiently large values of γ the real ξ and micromorphic $\xi^{\rm m}$ parameters become virtually identical.⁶

With the modified free energy (B.1), the time-dependent PDE for the reaction kinetics (8.3) is replaced with a time-independent PDE for the micromorphic ξ^{m} of the form

$$0 = \Delta(\lambda \xi^{m}) + \gamma(\xi - \xi^{m}), \tag{B.3}$$

where λ is the same gradient energy parameter as discussed in the main body of this work. The reaction ξ is now an internal state variable with an evolution equation of the form

$$\dot{\xi} = -R_0 \mathcal{F}, \quad \text{with}$$

$$\mathcal{F} = \left(\frac{c_{\text{max}}^{\text{D}}}{c_{\text{max}}^{\text{R}}} \bar{c} + (1 - \bar{\xi})\right) (\mu_0^{\xi} - \mu_0^{\alpha}) + \frac{E^{\text{a}}}{c_{\text{max}}^{\text{R}}} (2\bar{\xi} - 6\bar{\xi}^2 + 4\bar{\xi}^3) - R\vartheta \ln \left(\frac{\bar{c}}{1 - \bar{c}}\right)$$

$$+ J^{\text{c}} \mathbf{M}^{\text{m}} : \left((1 - \bar{\xi}) \mathbf{N}^{\alpha, D} + \bar{\xi} \mathbf{N}^{\beta, D} - \bar{\xi} \mathbf{N}^{\beta, R}\right) + \gamma(\xi - \xi^{\text{m}}).$$
(B.4)

⁶ See for example Appendix B in Di Leo (2015) which compares micromorphic and direct numerical simulations for a Cahn–Hilliard phase-field simulation and demonstrates in detail the equivalence of the two methods for suitable choice of simulation parameters.

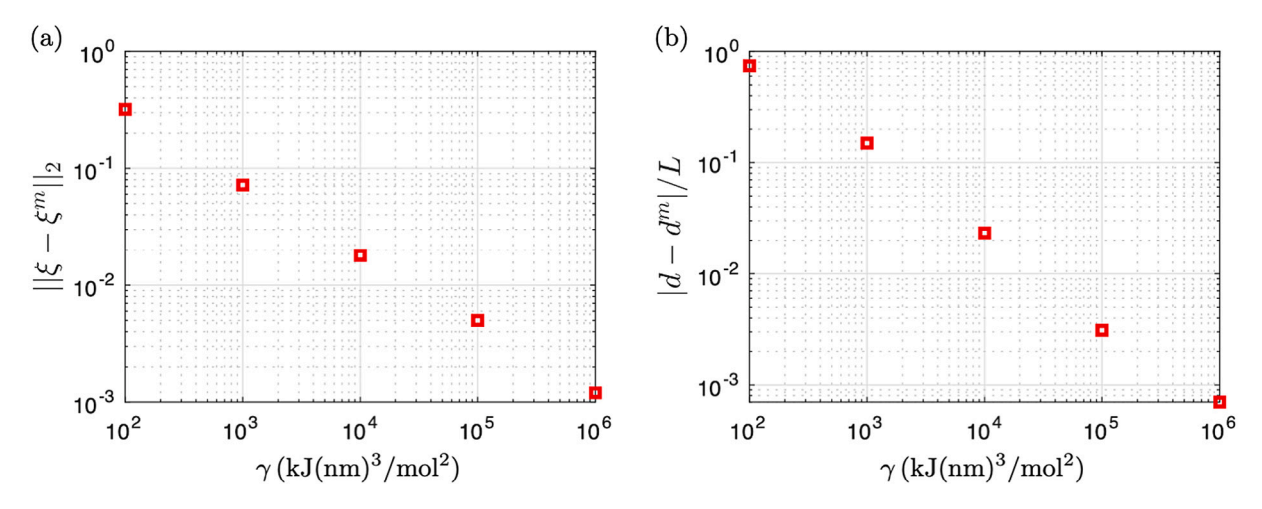


Fig. 16. (a) L_2 norm of the difference between ξ and ξ^m in diffusion–reaction simulations when the reaction front is half-way through the simulation domain as a function of the simulation parameter γ. (b) Normalized difference between the width of the reaction front in simulations with a direct implementation of the theory, d, and a micromorphic implementation d^m as a function of the simulation parameter γ. The simulation domain is $L = 10 \, \mu m$ in size.

We note that using (B.3) the term $\gamma(\xi - \xi^m) = -\text{Div}(\lambda \nabla \xi^m)$, and thus the result of this process is that we have replaced the original term $\text{Div}(\lambda \nabla \xi)$ with one in terms of $\nabla \xi^m$.

Finally, the boundary conditions (8.6) are replaced with

$$\xi^{\mathbf{m}} = \xi \quad \text{on } S_{\mu^{\xi}} \times (0, T),$$

$$\lambda \nabla \xi^{\mathbf{m}} \cdot \mathbf{n}_{\mathbf{R}} = \eta \quad \text{on } S_{\rho^{\xi}} \times (0, T).$$
(B.5)

which will act in identical fashion to the original boundary conditions.

To calibrate the simulation parameter γ so as to provide results which accurately describe the original problem we ran multiple diffusion–deformation simulations equivalent to those shown in Section 9.1. Fig. 16(a) shows the L₂ norm of the difference $\xi - \xi^{\rm m}$ over the simulation domain when the reaction front is half way through the simulation domain as a function of γ . As shown, as the parameter γ increase, penalizing the difference between ξ and $\xi^{\rm m}$, the difference becomes negligibly small.

To further emphasize the convergence towards the exact implementation we implemented the theory (without mechanics) through a direct implementation of the PDEs summarized in Section 8 **without** the use of the micromorphic variable. Fig. 16(b) compares the width of the reaction zone from the direct implementation d, and the micromorphic implementation d^{micromorph}. Here too we observe that as the value of γ increases the difference between the reaction front width becomes negligible and we recover the exact solution. Based on these results, we ensure that the micromorphic approach yields valid results by choosing $\gamma = 5 \times 10^5$ kJ(nm)³/mol² for all simulations shown in Section 9 of the main body of this work.

References

Anand, Lallit, 2012. A cahn-hilliard-type theory for species diffusion coupled with large elastic-plastic deformations. J. Mech. Phys. Solids 60 (12), 1983–2002. Bazant, Martin Z., 2013. Theory of chemical kinetics and charge transfer based on nonequilibrium thermodynamics. Acc. Chem. Res. 46 (5), 1144–1160. Bistri, Donald, Afshar, Arman, Di Leo, Claudio V., 2020. Modeling the chemo-mechanical behavior of all-solid-state batteries: a review. Meccanica 1–32.

Boebinger, Matthew G., Yeh, David, Xu, Michael, Miles, B. Casey, Wang, Baolin, Papakyriakou, Marc, Lewis, John A, Kondekar, Neha P, Cortes, Francisco Javier Quintero, Hwang, Sooyeon, et al., 2018. Avoiding fracture in a conversion battery material through reaction with larger ions. Joule 2 (9), 1783–1799. Bosnjak, Nikola, Nadimpalli, Siva, Okumura, Dai, Chester, Shawn A., 2020. Experiments and modeling of the viscoelastic behavior of polymeric gels. J. Mech. Phys. Solids 137, 103829.

Bower, Allan F., Guduru, Pradeep R., Sethuraman, Vijay A., 2011. A finite strain model of stress, diffusion, plastic flow, and electrochemical reactions in a lithium-ion half-cell. J. Mech. Phys. Solids 59 (4), 804–828.

Brassart, Laurence, Suo, Zhigang, 2013. Reactive flow in solids. J. Mech. Phys. Solids 61 (1), 61-77.

Bucci, Giovanna, Nadimpalli, Siva P.V., Sethuraman, Vijay A., Bower, Allan F., Guduru, Pradeep R., 2014. Measurement and modeling of the mechanical and electrochemical response of amorphous si thin film electrodes during cyclic lithiation. J. Mech. Phys. Solids 62, 276–294.

Chase Jr, M.W., 1998. NIST-JANAF thermochemical tables fourth edition. J. Phys. Chem. Ref. Data Monogr. 9.

Cheng, Yang-Tse, Verbrugge, Mark W., 2008. The influence of surface mechanics on diffusion induced stresses within spherical nanoparticles. J. Appl. Phys. 104 (8), 083521.

Christensen, John, Newman, John, 2006. A mathematical model of stress generation and fracture in lithium manganese oxide. J. Electrochem. Soc. 153 (6), A1019-A1030.

Cogswell, Daniel A., Bazant, Martin Z., 2013. Theory of coherent nucleation in phase-separating nanoparticles. Nano Lett. 13 (7), 3036–3041.

Cui, Zhiwei, Gao, Feng, Qu, Jianmin, 2012. A finite deformation stress-dependent chemical potential and its applications to lithium ion batteries. J. Mech. Phys. Solids 60 (7), 1280–1295.

Cui, Chuanjie, Ma, Rujin, Martínez-Pañeda, Emilio, 2020. A phase field formulation for dissolution-driven stress corrosion cracking. J. Mech. Phys. Solids 104254.

DeHoff, Robert, 2006. Thermodynamics in Materials Science. CRC Press.

- Di Leo, Claudio V., 2015. Chemo-Mechanics of Lithium-Ion Battery Electrodes (PhD thesis). Massachusetts Institute of Technology, URL: https://dspace.mit.edu/handle/1721.1/100119.
- Di Leo, Claudio V., Rejovitzky, Elisha, Anand, Lallit, 2014. A Cahn-Hilliard-type phase-field theory for species diffusion coupled with large elastic deformations: application to phase-separating Li-ion electrode materials. J. Mech. Phys. Solids 70, 1–29.
- Di Leo, Claudio V., Rejovitzky, Elisha, Anand, Lallit, 2015. Diffusion-deformation theory for amorphous silicon anodes: the role of plastic deformation on electrochemical performance. Int. J. Solids Struct. 67, 283–296.
- El Kadiri, H., Horstemeyer, M.F., Bammann, D.J., 2008. A theory for stress-driven interfacial damage upon cationic-selective oxidation of alloys. J. Mech. Phys. Solids 56 (12), 3392–3415.

Forest, Samuel, 2009. Micromorphic approach for gradient elasticity, viscoplasticity, and damage. J. Eng. Mech. 135 (3), 117-131.

Ganser, Markus, Hildebrand, Felix E., Kamlah, Marc, McMeeking, Robert M., 2019. A finite strain electro-chemo-mechanical theory for ion transport with application to binary solid electrolytes. J. Mech. Phys. Solids 125, 681–713.

Germain, Paul, 1973. The method of virtual power in continuum mechanics. Part 2: Microstructure. SIAM J. Appl. Math. 25 (3), 556-575.

Ghasemi, Arman, Gao, Wei, 2020. A method to predict energy barriers in stress modulated solid-solid phase transitions. J. Mech. Phys. Solids 137, 103857.

Gigliotti, Marco, Olivier, Loic, Vu, Dinh Quy, Grandidier, Jean-Claude, Lafarie-Frenot, Marie Christine, 2011. Local shrinkage and stress induced by thermo-oxidation in composite materials at high temperatures. J. Mech. Phys. Solids 59 (3), 696–712.

Greenwood, N.N., Earnshaw, A., 1997. Chemistry of the Elements, second ed. Butterworth-Heinemann, Oxford, pp. 328-366.

Gurtin, Morton E., 2002. A gradient theory of single-crystal viscoplasticity that accounts for geometrically necessary dislocations. J. Mech. Phys. Solids 50 (1), 5–32.

Gurtin, Morton E., Fried, Eliot, Anand, Lallit, 2010. The Mechanics and Thermodynamics of Continua. Cambridge University Press.

Guyer, Jonathan E., Boettinger, William J., Warren, James A., McFadden, Geoffrey B., 2004. Phase field modeling of electrochemistry. I. Equilibrium. Phys. Rev. E 69 (2), 021603.

Hofmann, Tobias, Westhoff, Daniel, Feinauer, Julian, Andrä, Heiko, Zausch, Jochen, Schmidt, Volker, Müller, Ralf, 2020. Electro-chemo-mechanical simulation for lithium ion batteries across the scales. Int. J. Solids Struct. 184, 24–39.

Hu, Jin, Li, Hong, Huang, Xuejie, Chen, Liquan, 2006. Improve the electrochemical performances of Cr2O3 anode for lithium ion batteries. Solid State Ion. 177 (26–32), 2791–2799.

Konica, Shabnam, Sain, Trisha, 2020. A thermodynamically consistent chemo-mechanically coupled large deformation model for polymer oxidation. J. Mech. Phys. Solids 137, 103858.

Larcher, D., Sudant, G., Leriche, J.B., Chabre, Y., Tarascon, J.M., 2002. The electrochemical reduction of Co3 O 4 in a lithium cell. J. Electrochem. Soc. 149 (3), A234–A241.

Lee, Seok Woo, McDowell, Matthew T., Berla, Lucas A., Nix, William D., Cui, Yi, 2012. Fracture of crystalline silicon nanopillars during electrochemical lithium

insertion. Proc. Natl. Acad. Sci. 109 (11), 4080–4085. Levitas, Valery I., Attariani, Hamed, 2014. Anisotropic compositional expansion in elastoplastic materials and corresponding chemical potential: Large-strain

formulation and application to amorphous lithiated silicon. J. Mech. Phys. Solids 69, 84–111.

Li, Linsen, Meng, Fei, Jin, Song, 2012. High-capacity lithium-ion battery conversion cathodes based on iron fluoride nanowires and insights into the conversion

mechanism. Nano Lett. 12 (11), 6030–6037. Lin, Feng, Nordlund, Dennis, Weng, Tsu-Chien, Zhu, Ye, Ban, Chunmei, Richards, Ryan M., Xin, Huolin L., 2014. Phase evolution for conversion reaction electrodes

in lithium-ion batteries. Nat. Commun. 5, 3358. Liu, Xiao Hua, Zheng, He, Zhong, Li, Huang, Shan, Karki, Khim, Zhang, Li Qiang, Liu, Yang, Kushima, Akihiro, Liang, Wen Tao, Wang, Jiang Wei, et al., 2011.

Anisotropic swelling and fracture of silicon nanowires during lithiation. Nano Lett. 11 (8), 3312–3318.

Loeffel, Kaspar, Anand, Lallit, 2011. A chemo-thermo-mechanically coupled theory for elastic-viscoplastic deformation, diffusion, and volumetric swelling due to a chemical reaction. Int. J. Plast. 27 (9), 1409–1431.

Loeffel, Kaspar, Anand, Lallit, Gasem, Zuhair M., 2013. On modeling the oxidation of high-temperature alloys. Acta Mater. 61 (2), 399-424.

Mao, Yunwei, Anand, Lallit, 2018. A theory for fracture of polymeric gels. J. Mech. Phys. Solids 115, 30-53.

Minervino, M., Gigliotti, M., Lafarie-Frenot, M.C., Grandidier, J.C., 2014. A coupled experimental/numerical approach for the modelling of the local mechanical behaviour of epoxy polymer materials. J. Mech. Phys. Solids 67, 129–151.

Nadkarni, Neel, Rejovitsky, Elisha, Fraggedakis, Dimitrios, Di Leo, Claudio V., Smith, Raymond B., Bai, Peng, Bazant, Martin Z., 2018. Interplay of phase boundary anisotropy and electro-auto-catalytic surface reactions on the lithium intercalation dynamics in Li X FePO 4 plateletlike nanoparticles. Phys. Rev. Mater. 2 (8), 085406.

Okumura, Dai, Kawabata, Hironori, Chester, Shawn A., 2020. A general expression for linearized properties of swollen elastomers undergoing large deformations. J. Mech. Phys. Solids 135, 103805.

Poizot, P.L.S.G., Laruelle, S., Grugeon, S., Dupont, L., Tarascon, J.M., 2000. Nano-sized transition-metal oxides as negative-electrode materials for lithium-ion batteries. Nature 407 (6803), 496.

PubChem Database, 2005. National Center for Biotechnology Information. PubChem Database. Hydropyrite, CID=123110. https://pubchem.ncbi.nlm.nih.gov/compound/Hydropyrite.

Raberg, Mathias, 2007. Black Liquor Gasification: Experimental Stability Studies of Smelt Components and Refractory Lining (PhD thesis). Energiteknik och termisk processkemi.

Ren, Zhimin, Wang, Zhiyu, Chen, Chao, Wang, Jia, Fu, Xinxin, Fan, Chenyao, Qian, Guodong, 2014. Preparation of carbon-encapsulated ZnO tetrahedron as an anode material for ultralong cycle life performance lithium-ion batteries. Electrochim. Acta 146, 52–59.

Salvadori, A., McMeeking, R., Grazioli, D., Magri, M., 2018. A coupled model of transport-reaction-mechanics with trapping. Part I-small strain analysis. J. Mech. Phys. Solids 114. 1–30.

Simulia, Dassault Systèmes, 2010. Abaqus Analysis User's Manual 6.10. Providence, RI, USA.

Svendsen, Bob, Shanthraj, Pratheek, Raabe, Dierk, 2018. Finite-deformation phase-field chemomechanics for multiphase, multicomponent solids. J. Mech. Phys. Solids 112, 619–636.

Tao, Yiming, Rui, Kun, Wen, Zhaoyin, Wang, Qingsong, Jin, Jun, Zhang, Tao, Wu, Tian, 2016. Fes2 microsphere as cathode material for rechargeable lithium batteries. Solid State Ion. 290, 47–52.

Tolpygo, V.K., Dryden, J.R., Clarke, D.R., 1998. Determination of the growth stress and strain in α -Al2O3 scales during the oxidation of Fe–22Cr–4.8 Al–0.3 Y alloy. Acta Mater. 46 (3), 927–937.

Ulm, Franz-Josef, Coussy, Olivier, Kefei, Li, Larive, Catherine, 2000. Thermo-chemo-mechanics of ASR expansion in concrete structures. J. Eng. Mech. 126 (3), 233–242.

Wan, Wenhui, Zhang, Qianfan, Cui, Yi, Wang, Enge, 2010. First principles study of lithium insertion in bulk silicon. J. Phys.: Condens. Matter 22 (41), 415501. Wang, Jincheng, Inatomi, Yuko, 2010. Three-dimensional phase field modeling of the faceted cellular growth. ISIJ Int. 50 (12), 1901–1907.

Wang, Feng, Yu, Hui-Chia, Chen, Min-Hua, Wu, Lijun, Pereira, Nathalie, Thornton, Katsuyo, Van der Ven, Anton, Zhu, Yimei, Amatucci, Glenn G., Graetz, Jason, 2012. Tracking lithium transport and electrochemical reactions in nanoparticles. Nat. Commun. 3, 1201.

- Xu, G.N., Yang, L., Zhou, Y.C., Pi, Z.P., Zhu, W., 2019. A chemo-thermo-mechanically constitutive theory for thermal barrier coatings under CMAS infiltration and corrosion. J. Mech. Phys. Solids 133, 103710.
- Yu, Seung-Ho, Lee, Soo Hong, Lee, Dong Jun, Sung, Yung-Eun, Hyeon, Taeghwan, 2016. Conversion reaction-based oxide nanomaterials for lithium ion battery anodes. Small 12 (16), 2146–2172.
- Zhang, Xiaoxuan, Lee, Seok Woo, Lee, Hyun-Wook, Cui, Yi, Linder, Christian, 2015. A reaction-controlled diffusion model for the lithiation of silicon in lithium-ion batteries. Extreme Mech. Lett. 4, 61–75.
- Zhang, Xiangchun, Shyy, Wei, Sastry, Ann Marie, 2007. Numerical simulation of intercalation-induced stress in li-ion battery electrode particles. J. Electrochem. Soc. 154 (10), A910–A916.
- Zhang, Wei-Ming, Wu, Xing-Long, Hu, Jin-Song, Guo, Yu-Guo, Wan, Li-Jun, 2008. Carbon coated fe3o4 nanospindles as a superior anode material for lithium-ion batteries. Adv. Funct. Mater. 18 (24), 3941–3946.
- Zhao, Yunong, Chen, Yanfei, Ai, Shigang, Fang, Daining, 2019a. A diffusion, oxidation reaction and large viscoelastic deformation coupled model with applications to SiC fiber oxidation. Int. J. Plast. 118, 173–189.
- Zhao, Kejie, Pharr, Matt, Cai, Shengqiang, Vlassak, Joost J., Suo, Zhigang, 2011a. Large plastic deformation in high-capacity lithium-ion batteries caused by charge and discharge. J. Am. Ceram. Soc. 94, \$226–\$235.
- Zhao, Ying, Stein, Peter, Bai, Yang, Al-Siraj, Mamun, Yang, Yangyiwei, Xu, Bai-Xiang, 2019b. A review on modeling of electro-chemo-mechanics in lithium-ion batteries. J. Power Sources 413, 259–283.
- Zhao, Kejie, Wang, Wei L., Gregoire, John, Pharr, Matt, Suo, Zhigang, Vlassak, Joost J., Kaxiras, Efthimios, 2011b. Lithium-assisted plastic deformation of silicon electrodes in lithium-ion batteries: a first-principles theoretical study. Nano Lett. 11 (7), 2962–2967.